

Cover Page



Universiteit Leiden



The handle <http://hdl.handle.net/1887/22066> holds various files of this Leiden University dissertation.

**Author:** Rieder, Steven

**Title:** The clustered universe : het geclusterde heelal

**Issue Date:** 2013-10-30



# **The Clustered Universe**

Het geclusterde heelal

Proefschrift

ter verkrijging van  
de graad van Doctor aan de Universiteit Leiden,  
op gezag van Rector Magnificus prof. mr. C.J.J.M. Stolker,  
volgens besluit van het College voor Promoties  
te verdedigen op woensdag 30 oktober 2013  
klokke 15:00 uur

door

**Steven Rieder**  
geboren te Zwolle  
in 1983

Promotiecommissie

Promotores:	Prof. dr. Simon Portegies Zwart Prof. dr. Cees de Laat	(Universiteit van Amsterdam)
Overige leden:	Prof. dr. Henri Bal Dr. Paola Grosso Prof. dr. Steve McMillan Prof. dr. Huub Röttgering Prof. dr. Joop Schaye Prof. dr. Tom Theuns Prof. dr. Rien van de Weygaert	(Vrije Universiteit Amsterdam) (Universiteit van Amsterdam) (Drexel University)  (Durham University) (Rijksuniversiteit Groningen)

ISBN: 978-94-6191-915-1

© 2013 Steven Rieder, 

Dit werk is gelicenseerd onder een Creative Commons Naamsvermelding-GelijkDelen 3.0 Unported licentie. Ga naar <http://creativecommons.org/licenses/by-sa/3.0/> om een kopie van de licentie te kunnen lezen.

Dit proefschrift werd ondersteund door NWO IsFast grant #643.000.803 en het Leids Kerkhoven Bosscha fonds.

*Nou moe!?!  
-- Guust<sup>1</sup>*

---

<sup>1</sup>Franquin (1972)



# Contents

<b>Acronyms</b>	<b>ix</b>
<b>1 Introduction</b>	<b>1</b>
1.1 Why simulate the Universe? . . . . .	2
1.2 Simulating gravity on a large scale . . . . .	2
1.2.1 Finding the initial conditions . . . . .	2
1.2.2 The Millennium run . . . . .	3
1.3 Work in this thesis . . . . .	5
1.3.1 The CosmoGrid project . . . . .	5
1.3.2 Obtaining computational power (Chapter 2) . . . . .	5
1.3.3 Results of CosmoGrid (Chapter 3) . . . . .	7
1.3.4 Galaxies in the void (Chapter 4) . . . . .	7
1.3.5 Star clusters in a dark matter halo (Chapter 5) . . . . .	7
1.3.6 Open clusters in a galaxy (Chapter 6) . . . . .	7
<b>2 Cosmological simulations on a grid of supercomputers</b>	<b>9</b>
2.1 Introduction . . . . .	10
2.1.1 Related work . . . . .	10
2.2 Improvements to SUSHI . . . . .	11
2.3 Tests on a single site . . . . .	11
2.3.1 Setup . . . . .	11
2.3.2 Results . . . . .	12
2.4 Tests across three sites . . . . .	13
2.4.1 Setup . . . . .	13
2.4.2 Results . . . . .	14
2.5 User Experiences . . . . .	15
2.6 Conclusion . . . . .	16

<b>3</b>	<b>The CosmoGrid simulation</b>	<b>19</b>
3.1	Introduction . . . . .	20
3.2	Initial Conditions and Numerical Method . . . . .	22
3.3	Results . . . . .	25
3.3.1	Mass Function . . . . .	25
3.3.2	Density Structures of Most Massive Halos . . . . .	30
3.3.3	Concentration Distributions . . . . .	32
3.3.4	Spin Distributions . . . . .	36
3.3.5	Subhalo . . . . .	39
3.4	Discussions and Summary . . . . .	42
3.A	The Effect of Dynamical State of Halos . . . . .	43
<b>4</b>	<b>Assembly of filamentary void galaxy configurations</b>	<b>47</b>
4.1	Introduction . . . . .	48
4.1.1	The Void Galaxy Survey . . . . .	49
4.1.2	Outline . . . . .	50
4.2	Simulations . . . . .	52
4.2.1	Setup . . . . .	52
4.2.2	Selection of the simulated haloes . . . . .	53
4.2.3	Analysis of the environment . . . . .	55
4.3	Evolution of void haloes . . . . .	58
4.3.1	Halo Structure . . . . .	59
4.3.2	Halo Assembly and Evolution . . . . .	60
4.3.3	Dynamical Evolution . . . . .	61
4.4	Large scale environment . . . . .	64
4.4.1	The web-like environment of CGV-G . . . . .	64
4.4.2	The wall-like environment of CosmoGrid Void systems (CGVs) . . . . .	68
4.4.3	Intravoid Filaments . . . . .	69
4.4.4	Evolution of the intravoid cosmic web . . . . .	70
4.5	CGV halo configurations and VGS_31: a comparison . . . . .	76
4.5.1	Size evolution of the CGVs . . . . .	79
4.5.2	Energy considerations . . . . .	79
4.5.3	The origin of VGS_31 . . . . .	81
4.6	Discussion & Conclusions . . . . .	81
<b>5</b>	<b>Evolution of star clusters in a cosmological tidal field</b>	<b>85</b>
5.1	Introduction . . . . .	85
5.2	The experimental setup . . . . .	87
5.2.1	The CosmoGrid $N$ -body simulation . . . . .	87



5.2.2	Halo catalogue . . . . .	87
5.2.3	The clusters . . . . .	88
5.2.4	The tidal field . . . . .	93
5.2.5	Combining the clusters and the tidal field . . . . .	93
5.2.6	Escaping and bound stars . . . . .	95
5.2.7	Validation . . . . .	95
5.3	Results . . . . .	96
5.3.1	The evolution of the selected haloes . . . . .	96
5.3.2	The evolution of the star clusters . . . . .	98
5.4	Discussion and conclusions . . . . .	104
<b>6</b>	<b>Evolution of star clusters in an evolving galaxy</b>	<b>109</b>
6.1	Introduction . . . . .	110
6.2	The experimental setup . . . . .	111
6.2.1	The galaxy simulation . . . . .	111
6.2.2	Star cluster models . . . . .	112
6.2.3	Embedding star clusters in the galaxy . . . . .	113
6.3	Results . . . . .	114
6.3.1	Tidal fields . . . . .	114
6.3.2	Cluster evolution . . . . .	117
6.3.3	Comparison to observed open clusters . . . . .	119
6.3.4	Influence of eccentricity on cluster properties . . . . .	120
6.3.5	White dwarfs as a signature for tidal field strength . . . . .	120
6.4	Discussion and conclusions . . . . .	122
<b>7</b>	<b>Samenvatting</b>	<b>123</b>
7.1	Afstanden in het heelal . . . . .	123
7.2	Samenstelling van het heelal . . . . .	124
7.3	Simulaties . . . . .	126
7.4	De hoofdstukken in dit proefschrift . . . . .	127
7.4.1	Simulaties op gecombineerde supercomputers . . . . .	127
7.4.2	De CosmoGrid simulatie . . . . .	127
7.4.3	Ontstaan van sliertige melkwegen in leegtes . . . . .	128
7.4.4	Evolutie van bolhopen in halo's van donkere materie . . . . .	129
7.4.5	Evolutie van sterrenhopen in een melkweg . . . . .	129
	<b>Bibliography</b>	<b>130</b>
	<b>Curriculum Vitae</b>	<b>147</b>

**Nawoord**

**149**

# Acronyms and used codes

## Acronyms

<b>2dFGRS</b>	Two-degree-Field Galaxy Redshift Survey
<b>CDM</b>	Cold Dark Matter
<b>CGV</b>	CosmoGrid Void system
<b>CMB</b>	Cosmic Microwave Background
<b>DEISA</b>	Distributed European Infrastructure for Supercomputing Applications
<b>GBBP</b>	Gravitational Billion Body Problem
<b>GLIF</b>	Global Lambda Integrated Facility ( <a href="http://glif.is">http://glif.is</a> )
$\Lambda$ <b>CDM</b>	Lambda Cold Dark Matter
<b>SDSS</b>	Sloan Digital Sky Survey
<b>SPH</b>	Smoothed-particle hydrodynamics
<b>TCP</b>	Transmission Control Protocol
<b>TreePM</b>	Tree-Particle-Mesh
<b>VGS</b>	Void Galaxy Survey
<b>WMAP</b>	Wilkinson Microwave Anisotropy Probe

## Used codes

<b>AMUSE</b>	Astrophysical Multipurpose Software Environment
<b>Bonsai</b>	GPU-enabled Tree code (Bédorf et al. 2012)
<b>Consistent Trees</b>	Gravitationally Consistent Halo Catalogs and Merger Trees for Precision Cosmology (Behroozi et al. 2013b)
<b>DTFE</b>	Delaunay Tessellation Field Estimator
<b>FFTW</b>	Fastest Fourier Transform in the West (Frigo and Johnson 2005)
<b>Fi</b>	N-body/SPH code
<b>GRAFIC</b>	Code to generate initial conditions for cosmological simulations
<b>GreeM</b>	GRAPE TreePM (Yoshikawa and Fukushige 2005; Ishiyama et al. 2009b)
<b>MPGRAFIC</b>	Parallellised version of GRAFIC
<b>MPWide</b>	Light-weight communication library for distributed computing (Groen et al. 2010)
<b>NEXUS+</b>	Algorithm for the identification of Cosmic Web Environments (Cautun et al. 2013)
<b>ph4</b>	GPU-enabled direct N-body code
<b>Rockstar</b>	Robust Overdensity Calculation using K-Space Topologically Adaptive Refinement (Behroozi et al. 2013a)
<b>SUSHI</b>	Simulating the Universe Structure formation on Heterogeneous Infrastructures (Groen et al. 2011)

# 1 | Introduction

*“Space (...) is big. Really big. You just won't believe how vastly, hugely, mindbogglingly big it is. I mean, you may think it's a long way down the road to the chemist's, but that's just peanuts to space” (Adams 1986).* Although written in a work of fiction, this is correct: it's hard to imagine how vast the Universe really is. It takes light (which seems to move instantaneous to our eyes) more than two seconds to travel to the moon and back, a distance that would take over four months to travel at 120km/h. Yet, this distance is minute compared to other scales in the Universe. For instance, light from the nearest star (apart from the Sun) takes more than four years to reach us, and light from the galaxy nearest to us, Andromeda, takes 2.5 Myr to reach us. The current record holder for the furthest galaxy is about 12.5 Gyr away, nearly the age of the Universe itself.

Despite its huge size, the Universe is not static. It formed about 13.8 Gyr ago, and has been expanding ever since. Soon after the big bang, matter, which was initially distributed almost homogeneously, started clumping, forming the first stars. The first protogalaxies formed, which in time merged to form the galaxies we see nowadays in our region of space.

In our own galaxy, generations of stars formed and exploded before our own Sun and solar system formed from a giant molecular cloud. This cloud had been enriched with heavier elements such as carbon and oxygen, the building blocks for life, by these previous generations of stars. The Earth formed from remnants of this cloud around the Sun, and about 4.5 Gyr later, this thesis describing simulations of some of the mechanics in the Universe was complete.

## 1.1 Why simulate the Universe?

Since the distances are so large, timescales in astrophysics are often very long - on the order of millions to billions of years. While local stars can be measured to move, and while we can see variable stars and various stellar transients change on much shorter timescales, most of the far-away sky will remain completely unchanged during a human's lifetime. The process of forming galaxies and other large-scale structures in particular takes place over a very large amount of time.

In order to investigate how such structures form and evolve, we cannot resort to observing change in singular objects - this would simply take too long. To observe changes in objects of galactic scale, astronomers make the assumption that the Universe is homogenous and isotropic: on average, it looks the same in every direction. Galaxies that are far, far away - and therefore observed as they were a long time ago - can then be interpreted as the predecessors of modern close-by galaxies.

This still leaves a problem though: we cannot see the exact formation history of individual galaxies, only the evolution of galaxies in general. Even then, we observe local galaxies with much higher resolution than the faraway ones, so many details about these remain unknown.

In order to fill in these limitations, astronomers also try to investigate the Universe by modelling and simulating it. With simulations, we can investigate the formation of individual galaxies from very early on until now, and follow exactly what happens to it: how many other, smaller galaxies merge with it, when star formation occurs, etc.

## 1.2 Simulating gravity on a large scale

Such simulations to study galaxies can be done on various scales, from the size of the known Universe to the size of an individual galaxy. In order to model the formation of an individual galaxy though, we first have to know what the right initial conditions are - where was all the matter that ended up in this galaxy?

### 1.2.1 Finding the initial conditions

Finding the initial conditions of matter in the Universe is difficult, since we cannot just trace back the origin of all matter from current day observations. We can therefore roughly choose between two routes: either simulate a large environment with enough resolution to follow individual galaxies, or make assumptions about the composition of these galaxies.

As a starting point for the former (cosmological) type of simulations, we are fortunate enough to have a snapshot of the Universe when it was very young (only a few 100.000 years): the cosmic microwave background (CMB, see Figure 1.1 for a recent observation by the Planck satellite (Planck Collaboration et al. 2013)). From the CMB, we can obtain information about the distribution and type of matter in the Universe at that time, and we can use it to create large-scale initial conditions for cosmological simulations.

These initial conditions are only for a large scale though. Simulations of individual galaxies are not immediately possible, since we do not know which particles end up in one galaxy and which in another. So, we start with simulations of the large-scale Universe: the cosmic web. The cosmic web is a vast sponge-like structure that connects all galaxies with long filaments and walls. At the intersections of these filaments, galaxies are grouped in large clusters (see Figure 1.2).

### 1.2.2 The Millennium run

One of the most famous simulations performed of this large-scale structure is the Millennium simulation (Springel et al. 2005). This simulation (see Figure 1.3) consists of a volume of  $500 h^{-1}\text{Mpc}$ , about 2 billion lightyears, with 10 billion particles. In this huge volume, we can see the evolution of a very large number of individual galaxies.

However, there are some limitations to this simulation. Because of its large volume, the Millennium simulation is limited in its accuracy on smaller scales. A galaxy like the Milky Way for instance, would only consist of about 100-1000 particles, which is not enough to investigate its structure and formation in detail.

Another limitation is that the simulation consists only of dark matter - a type of matter that has mass and therefore exerts gravity, but which doesn't interact with light and doesn't collide with other particles. This is the dominant form of matter in the Universe - there is about five times more of it than there is baryonic matter. Yet, all matter that we can see, including all stars and ourselves, consists of the 'other' type of matter: baryonic, which does interact with light and which does collide and interact with light. Therefore, the structures that form in dark matter simulations do not exactly correspond to visible structures. While a galaxy will form inside a dark matter halo, its shape and structure will be completely different.

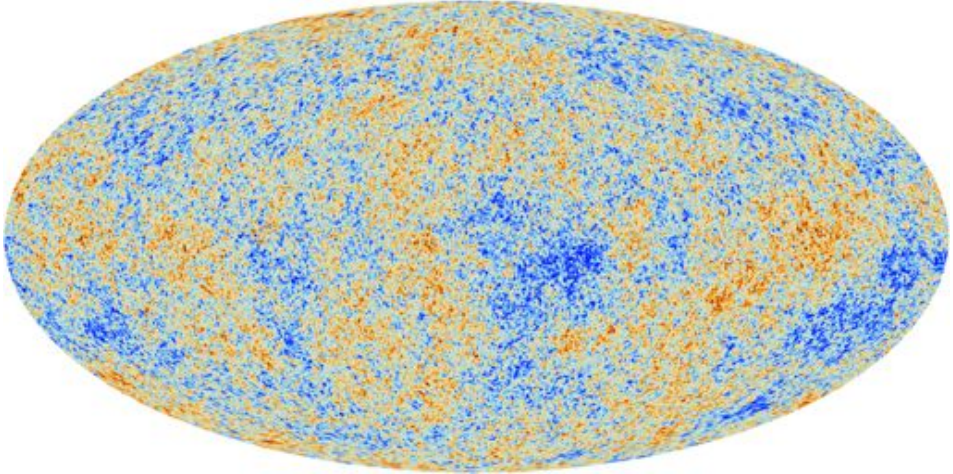


**Figure 1.1:** Projected image of the cosmic microwave background, the “initial conditions” of the Universe, as measured by the Planck mission (Planck Collaboration et al. 2013).

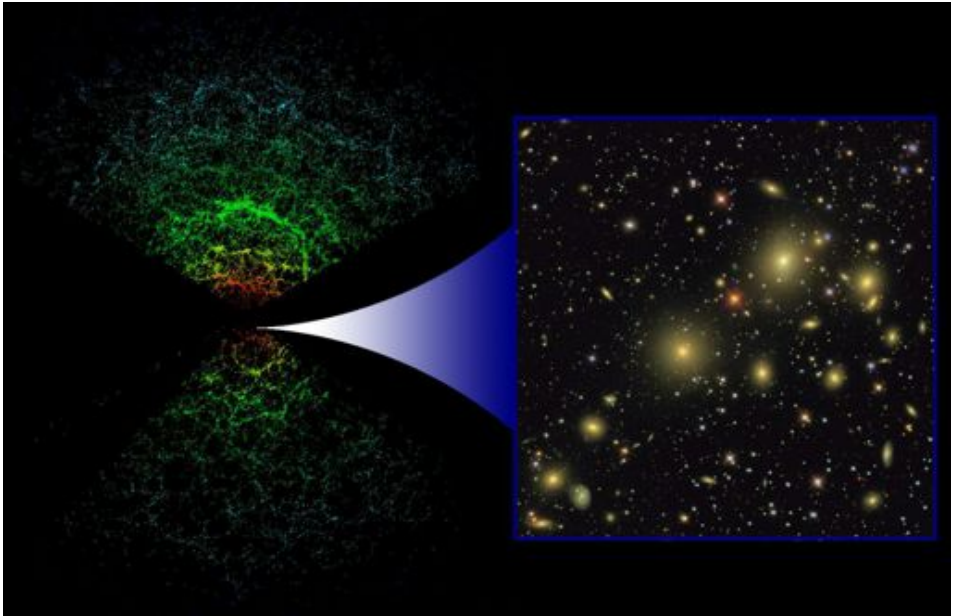


**Figure 1.2:** Image of galaxies at small and large distances, showing the web-like pattern in which they are distributed (left) and how they appear to us (right). Image from the SDSS.



## 1.3 Work in this thesis

### 1.3.1 The CosmoGrid project

In this thesis we mostly address the first of these limitations. In chapters 2-5, we discuss the CosmoGrid simulation and results obtained with it. CosmoGrid, like Millennium, is a dark matter-only simulation. However, it contains a much smaller volume, with an almost equal (8.5 billion) total number of particles. A Milky Way-size halo in CosmoGrid contains about 10 million particles, and will give us the much higher resolution needed to investigate internal properties of the halo and track mergers with small satellites.

A calculation like CosmoGrid is computationally very expensive. The computation time for direct gravity calculations scales with the square of the number of particles, and quickly becomes too large to be feasible. To do cosmological calculations, we therefore use approximations to direct calculation, like the TreePM method. This method calculates large-scale gravity using a particle mesh method, while a Barnes and Hut (1986) Tree code (which scales with  $N \log N$ ) calculates gravity on smaller scales. This way, it becomes possible to do gravity calculations even with large numbers of particles.

### 1.3.2 Obtaining computational power (Chapter 2)

To compute such simulations, we use supercomputers, which consist of a large number of nodes with several CPU cores each. But, as the number of particles is increased, so are the computational requirements. At a certain point, it becomes rather difficult to perform a calculation, due to the limited amount of resources available.

A solution to this is either to find and obtain time on a larger supercomputer, or to combine multiple smaller supercomputers into one large computational machine. For CosmoGrid, we took the latter approach. We developed the `GreenM` (Ishiyama et al. 2009b) code into the multi-site enabled `Sushi` (Groen et al. 2011) code, which uses the `MPWide` (Groen et al. 2010) message passing interface to connect supercomputers at large physical distances, regardless of the locally installed software. We used the `Sushi` code in combination with a fast, dedicated network to combine supercomputers from all over the world, from Amsterdam to Japan, Finland and Scotland (see Figures 1.4 and 1.5). When limitations due to scheduling were met, this allowed us to combine all these machines efficiently into one large machine. In chapter 2, we discuss the performance of such a set-up.

**Figure 1.3:** Final snapshot of the Millennium simulation (at  $z = 0$ ), showing the large scale structure as it forms in dark matter simulations. The image shows a slice of  $15 h^{-1} \text{Mpc}$  thick.

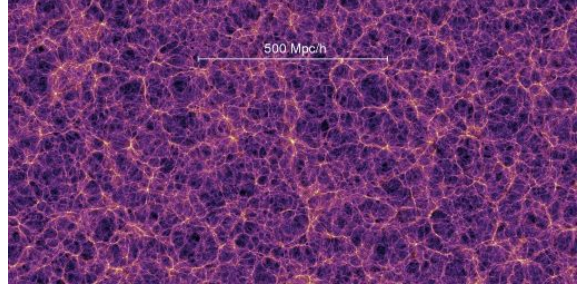


**Figure 1.4:** Locations of the supercomputers used in the CosmoGrid and GBBP projects.

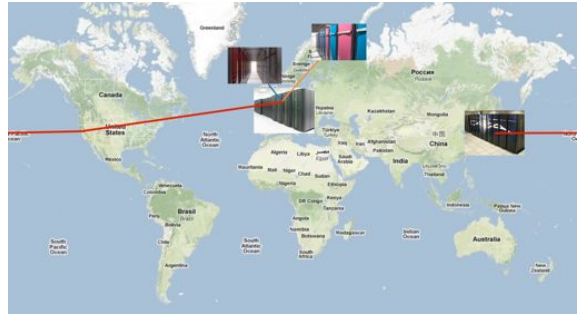
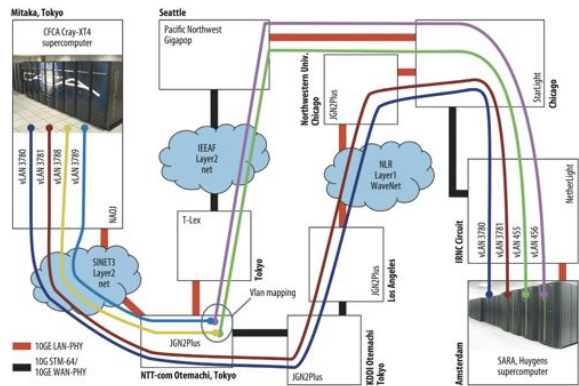


**Figure 1.5:** Schematic description of the network used in the CosmoGrid project to make the Tokyo-Amsterdam connection. Figure from Portegies Zwart et al. (2010a).



### 1.3.3 Results of CosmoGrid (Chapter 3)

The CosmoGrid simulation, as said, has very high spatial and mass resolution, uniquely suitable to investigate Milky Way- and dwarf-sized galaxies and groups of galaxies. In chapter 3, we discuss the properties of dark matter haloes found in this simulation, in particular we discuss how these properties change when we increase the resolution of the simulation.

### 1.3.4 Galaxies in the void (Chapter 4)

While dark matter is not directly observed, visible matter will follow its gravitational potential, and galaxies will form where dark matter haloes are. In chapter 4, we use this to describe the formation history of so-called void galaxies: galaxies that form in a seemingly empty region of space, where the amount of matter is much lower than in the surrounding environment. In a survey of galaxies in such voids, one particular system was found, consisting of three interconnected low-mass galaxies. Using the CosmoGrid simulation, we investigated how such a system can form, and what properties one may expect to observe.

### 1.3.5 Star clusters in a dark matter halo (Chapter 5)

Galaxies do not just have disks with loose stars, rather they contain a large number of star clusters. These are roughly divided into two types, although there is no physical difference: globular clusters, which are mostly old, massive systems that orbit the galaxy in the halo, and open clusters, which are generally much younger, extended objects in the stellar disk.

In chapter 5, we investigate the influence of the dark matter halo on star clusters resembling the globular clusters in the Milky Way. We use the CosmoGrid simulation to do this, by first finding two dark matter haloes, and then selecting particles at various distances from the galactic centre. We trace the orbits of these particles, and calculate the tidal forces exerted on them by the rest of the dark matter halo. We then combine these tidal forces to new simulations of star clusters in order to find how these disrupt.

### 1.3.6 Open clusters in a galaxy (Chapter 6)

One of the limitations of the project in chapter 5 was that star clusters formed at later age generally form in the disk of a galaxy, since all the gas is contained there, but that the CosmoGrid simulation does not contain any gas particles. We address this in chapter 6, where we use a re-simulation of a dark matter halo with

baryonic particles (gas and stars) as a large-scale environment. The result of this re-simulation is a galaxy that resembles our Milky Way.

In this chapter, we simulate a large number of open clusters from initial conditions chosen to match observed young clusters. We compare the surviving population of simulated clusters to open clusters observed in the solar neighbourhood, and investigate possible observable signatures in these clusters.

## 2 | Cosmological simulations on a grid of supercomputers

*Based on:*

*Derek Groen, Steven Rieder and Simon Portegies Zwart*

*High performance cosmological simulations on a grid of supercomputers*

*The First International Conference on Advanced Communications and Computation 2011*

We present results from our cosmological  $N$ -body simulation which consisted of  $2048^3$  particles and ran distributed across three supercomputers throughout Europe. The run, which was performed as the concluding phase of the GBBP DEISA project, integrated a 30Mpc box of dark matter using an optimized TreePM  $N$ -body integrator. We ran the simulation up to the present day ( $z=0$ ), and obtained an efficiency of about 0.93 over 2048 cores compared to a single supercomputer run. In addition, we share our experiences on using multiple supercomputers for high performance computing and provide several recommendations for future projects.

## 2.1 Introduction

Cosmological simulations are an efficient method to gain understanding of the formation of large-scale structures in the Universe. Large simulations were previously applied to model the evolution of dark matter in the Universe (Springel et al. 2005), and to investigate the properties of Milky-Way sized dark matter halos (Springel et al. 2008; Ishiyama et al. 2009a). However, these simulations are computationally demanding, and are best run on large production infrastructures. We have previously run a cosmological simulation using two supercomputers across the globe (Portegies Zwart et al. 2010a) with the GreeM integrator, and presented the SUSHI  $N$ -body integrator, which we used to run simulations across up to four supercomputers. The simulations we ran in the GBBP produced over 110 TB of data, which we have used to characterize the properties of ultra-faint dwarf galaxies (Ishiyama et al. 2013), and to compare the halo mass function in our runs to analytical formulae for the mass function. Among other things, we found that the halo mass function in our runs shows good agreement with the Sheth and Tormen (1999) mass function down to  $\sim 10^7 M_{\odot}$ .

Here we present the performance results of a production simulation across three supercomputers, as well as several other runs which all use an enhanced version of SUSHI. The production simulation ran continuously for  $\sim 8$  hours, using 2048 cores in total for calculations as well as 4 additional cores for communications. We achieved a peak performance of  $3.31 \times 10^{11}$  tree force interactions per second, a sustained performance of  $2.19 \times 10^{11}$  tree force interactions per second and a wide area communication overhead of less than 10% overall.

We briefly reflect on the improvements made to SUSHI for this work in section 2.2, while we report on tests performed on a single supercomputer in section 2.3. In section 2.4 we describe our experiments across three supercomputers and present our performance results. We reflect on our experiences on using multiple supercomputers for distributed supercomputing simulations, and provide several recommendations for users and resource providers in section 2.5 and present our conclusions in section 2.6.

### 2.1.1 Related work

There are several other projects which have run high performance computing applications across multiple supercomputers. These include simulations of a galaxy collision (Norman et al. 1996), a materials science problem (Pratt et al. 1997) as well as an analysis application for arthropod evolution (Stewart et al. 2004). A larger number of groups performed distributed computing across sites of PCs rather than supercomputers (e.g. Gualandris et al. 2007; Bal and Verstoep 2008;

Bar et al. 2009). Several software tools have been developed to facilitate high performance computing across sites of PCs (e.g. Karonis et al. 2003; Gabriel et al. 1998, 2004; Manos et al. 2008; Sundari M. et al. 2010)) and within volatile computing environments (Rood et al. 2010). The recently launched MAPPER EU-FP7 project (map 2012) seeks to run multi-scale applications across a distributed supercomputing environment, where individual subcodes periodically exchange information and (in some cases) run concurrently on different supercomputing architectures.

## 2.2 Improvements to SUSHI

Based on results of our earlier simulations and in preparation for the production run across three supercomputers we made several modifications to the SUSHI distributed  $N$ -body integrator. In our previous experiments a relatively large amount of computation and communication time was spent on (non-parallelised) particle-mesh integration. To reduce this bottleneck we now parallelised the particle-mesh integration routines using the parallel FFTW2 library and a one dimensional slab decomposition. We also optimized the communications of the particle-mesh integration by introducing a scheme where sites only broadcast those mesh cells which have actual particle content. This optimization reduced the size of the mesh communications by a factor roughly equal to the number of sites used, in the case of an equal domain distribution.

In some of the larger previous runs we also observed load imbalances if the code was run across two machines with different architectures, despite the presence of a load balancing scheme. This result has led us to further optimize the load balancing in SUSHI, taking into account not only the force integration time, but also the number of particles stored on each node. In addition to these changes, we also seized the opportunity to plug in a more recent MPWide version into SUSHI. This newer version contains several optimizations to improve the wide area communication over networks with a high latency.

## 2.3 Tests on a single site

### 2.3.1 Setup

We performed a number of runs on the Huygens supercomputer to validate the scalability of our new implementation, and to provide performance measurements against which we can compare our results using multiple sites. More information on the Huygens machine can be found in the second column of Table 2.3. The ini-

**Table 2.1:** Initial condition and accuracy parameters used for our simulations with  $2048^3$  particles.

Parameter	Value
Matter density parameter ( $\omega_0$ )	0.3
Cosmological constant ( $\Omega_\Lambda$ )	0.7
Hubble constant ( $H_0$ )	70.0 km/s/Mpc
Mass fluctuation parameter ( $\sigma_8$ )	0.8
Box size	$(30\text{Mpc})^3$
Softening for $2048^3$ particle run.	175 pc
Sampling rate for $2048^3$ particle run.	20000

tial conditions for this simulation is the snapshot at redshift  $z = 0.0026$  from the CosmoGrid simulation (described in Portegies Zwart et al. 2010a). We also use the simulation parameters chosen for the CosmoGrid simulation, which are summarized in Table 2.1. Here the first four parameters are constants, which are derived from WMAP observations (with a slight round-off), and the physical size of our simulated system is given by the fifth parameter (Box size). The softening in our simulation (i.e. a length value added to reduce the intensity of close interactions) and the sampling rate are given by the last two parameters. The sampling rate is the ratio of particles in the simulation divided by the number of particles sampled by the load balancing scheme. Our simulation used a mesh size of  $512^3$  cells. We ran the simulation using respectively 512 cores and 1024 cores until  $z = 0.0024$ , and using 2048 cores until the simulation completed (at  $z = 0$ ). The number of force calculations per step in the simulation varies for different  $z$  values, though these variations are negligible for  $z < 0.01$ .

### 2.3.2 Results

The performance results of our runs are shown in Table 2.2. In addition, the total runtime of the run using 2048 cores is given by the light blue line in Figure 2.1 (top). The overall performance of the code is dominated by calculations, with the communication overhead ranging from  $\sim 5\%$  for 512 cores to  $\sim 10\text{-}15\%$  for 2048 cores. During the run using 2048 cores, several snapshots were written. This resulted in a greatly increased execution time during two steps of the run.



**Table 2.2:** Overview of experiments performed with the enhanced SUSHI code on the Huygens supercomputer. The time spent on communication is given in the fourth column, while the total runtime is given in the fifth column. All times are measured per step, averaged over steps 1-11. In addition we included the timing results of the last 10 steps of the simulation running on 2048 cores (bottom row).

$N$	$p$	$\theta$	comm. t [s]	runtime [s]	$z$ range $\times 10^{-3}$	speed-up
2048 <sup>3</sup>	512	0.5	19.18	501.3	2.5-2.4	1
2048 <sup>3</sup>	1024	0.5	13.96	258.2	2.5-2.4	1.94
2048 <sup>3</sup>	2048	0.5	22.34	151.0	2.5-2.4	3.32
2048 <sup>3</sup>	2048	0.5	16.22	143.7	0.1-0.0	-

## 2.4 Tests across three sites

### 2.4.1 Setup

We performed our main run using a total of 2048 cores across three supercomputers, which are listed in Table 2.3. These machines include Huygens in the Netherlands (1024 cores), Louhi in Finland (512 cores), and HECToR in Scotland (512 cores). The sites are connected to the DEISA shared network with either a 1Gbps interface (HECToR) or a 10Gbps interface (Huygens, Louhi). The initial conditions and simulation parameters chosen are identical to those of the runs using 1 supercomputer, although we use a mesh of  $256^3$  cells. The use of a smaller mesh size results in a slightly higher calculation time as tree interactions are calculated over a longer range, but a somewhat lower time spent on intra-site communications. We configured MPWide to use 64 parallel TCP streams per path for the wide area communication channels, each with a TCP buffer size set at 768 kB and packet-pacing set at 10 MB/s maximum. We enabled some load balancing during the run, though we had to limit the boundary moving length per step to 0.00001 of the box length due to memory constraints on our communication nodes and the presence of dense halos in our initial condition.

In addition to the main run, we also performed three smaller runs using the same code across the same three supercomputers. These include one run with  $1024^3$  particles using 80 cores per supercomputer, and two runs with  $512^3$  particles using 40 cores per supercomputer. These runs also used a mesh size of  $256^3$ , though we did reduce the sampling rate to respectively 10000 and 5000 for the runs with  $1024^3$  and  $512^3$  particles. The force softening used for these runs were respectively 1.25kpc and 2.5kpc, and we set the boundary moving length limit to 0.01 of the box length. Some of the measurements were made using an opening angle  $\theta$  of 0.3, rather than 0.5. Using a smaller opening angle results a higher accuracy of the

**Table 2.3:** Properties of the three supercomputers used for our run. The measured peak number of tree force interactions (in millions) per second per core is given for each site in the bottom row.

Name	Huygens	Louhi	HECToR
Location	Amsterdam	Espoo	Edinburgh
Vendor	IBM	Cray	Cray
Architecture	Power6	XT4	XT4
# of cores	3328	4048	12288
CPU [GHz]	4.7	2.3	2.3
RAM / core [GB]	4/8	1/2	2
force calcs. / core [Mints/s]	185	256	250

force integration on close range, but also results in a higher force calculation and tree structure communication time per step.

## 2.4.2 Results

The timing results of our production run are shown in Figure 2.1. Here, we also added the wall-clock time results of the simulation run using 2048 cores on Huygens as reference. The simulation run across three sites is only  $\sim 9\%$  slower per step than the single-site run, despite the slightly higher force calculation time due to the lower number of mesh cells. The peaks in wall-clock time of the single site run are caused by the writing of snapshots during those steps (we only wrote one snapshot at the end of the three site run). The total wide area communication overhead of our run is  $\lesssim 10\%$  at about 15s per step. Most of this time is required to exchange the tree structures between sites, though the communications for the parallelised particle-mesh require an additional  $\sim 2.5s$  per step. Despite the use of a shared wide area network, the communication performance of our run shows very little jitter and no large slowdowns. We provide a snapshot of the final state of the simulation (at  $z = 0$ ), distributed across the three supercomputers, in Figure 2.2.

We also provide a numerical overview of the production run performance, as well as that of several other runs which use the new code, in Table 2.4. The communication overhead for the runs with  $512^3$  particles is less than 20%, while the overhead for the run with  $1024^3$  particles is just 6.5%. The parallelisation of the particle-mesh integration and the enhanced load balancing greatly improved the performance of these runs, especially in the case with  $1024^3$  particles. Here, the communication overhead was reduced by  $\sim 60\%$  and the overall runtime by more than 25% compared to the previous version (Groen et al. 2011).

**Table 2.4:** Overview of experiments performed with the enhanced SUSHI code across all three supercomputers. All times are measured per step, averaged over 10 steps.

$N$	$p$	$\theta$	comm. time		runtime	$z$ range
			WAN	total		
$512^3$	120	0.3	6.925	7.312	39.70	11.8-10.1
$512^3$	120	0.5	5.982	6.335	24.60	9.9-8.8
$1024^3$	240	0.3	12.09	14.04	214.5	17.0-14.9
$2048^3$	2048	0.5	15.40	24.77	167.7	0.0026-0.0025
$2048^3$	2048	0.5	14.62	23.13	155.2	0.0001-0

## 2.5 User Experiences

We have presented results from several cosmological simulations which run across three supercomputers, including a production run lasting for 8 hours. In the process of seeking a solution for wide area message passing between supercomputers, requesting allocations, arranging network paths and preparing for the execution of these simulations, we have learned a number of valuable lessons.

Primarily, we found that it is structurally possible to do high performance computing across multiple supercomputers. During the GBBP project we have run a considerable number of large-scale simulations using two or more supercomputers, with results improving as we were able to further enhance the  $N$ -body integrator and optimize the MPWide communication library for the wide area networks that we used.

The cooperation of the resource providers was particularly crucial in this project, as they enabled previously unavailable network paths and provided us with means to initiate simulations concurrently at the different sites. However, reserving networks and orchestrating concurrent supercomputer runs currently does require a disproportionate amount of time and effort, which makes performance optimization and debugging a challenging task. The effort required to run applications across supercomputers can be greatly reduced if resource providers were to adopt automated resource reservation systems for their supercomputers, and maintain shared high-bandwidth networking between sites. The persistent DEISA shared network connections helped greatly in our case, as we could use it at will without prior network reservations.

The software environment across different supercomputers, even within the same distributed infrastructure, is very heterogeneous. This made it unattractive to use existing middleware or message passing implementations to make different sites interoperable. We chose to use a modular approach where we connected platform-specific optimized versions of the SUSHI code with the MPWide com-

munication library. With MPWide being a user-space tool that requires no external libraries or administrative privileges, we are able to install and run the simulation code in the locally preferred software environments on each site without needing any additional (grid) middleware. We recommend adopting a similar modular software approach in future distributed supercomputing efforts for its ease of installation and optimization, at least until resource providers present a homogeneous and interoperable software environment for distributed supercomputing.

This paper focuses on the calculation and communication performance aspects of a single application run across supercomputers. However, the methods presented here can be applied for several other purposes. During this project we were confronted with additional overhead introduced by disk I/O, as can be observed in Figure 2.1. With supercomputer disk performance and capacity improving at a much slower rate than the compute power, the deployment of an application across sites may help to eliminate a disk I/O performance bottleneck, though a detailed investigation will be needed to quantify such potential benefit. Additionally, the communication technique could be used to facilitate periodic exchanges between different simulation codes, each of which runs on a different site and tackles a different aspect of a complex multi-scale or multi-physics problem.

## 2.6 Conclusion

Our results show that cosmological production simulations run efficiently across supercomputers for a prolonged time. The political effort required to arrange cross-supercomputer runs is considerable, and is an important reason why few people have attempted to run production simulations across supercomputers. We have shown that the added overhead of using a network of supercomputers is rather marginal for at least one optimized production application and that given the right (political) environment, supercomputers can be conveniently connected to form even larger high performance computing resources.

## Acknowledgements

*We are grateful to Jeroen Bédorf, Juha Fagerholm, Tomoaki Ishiyama, Esko Keränen, Walter Lioen, Jun Makino, Petri Nikunen, Gavin Pringle and Joni Virtanen for their contributions to this work. This research is supported by the Netherlands organization for Scientific research (NWO) grant #639.073.803, #643.200.503 and #643.000.803, the Stichting Nationale Computerfaciliteiten (project #SH-095-08) and the MAPPER EU-FP7 project (grant no. RI-261507). We thank the DEISA Consortium (EU FP6 project RI-031513 and FP7 project RI-222919) for support within the DEISA Extreme Computing Initiative (GBBP project).*

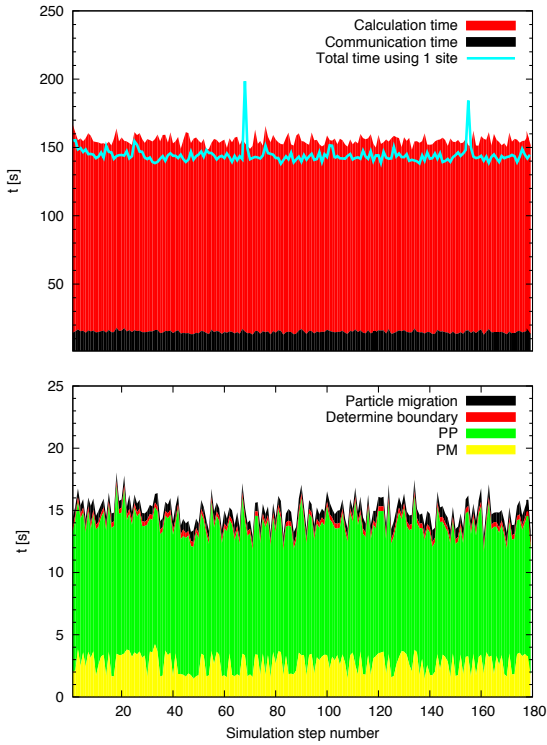


**Figure 2.1:** Performance results of the production simulation across three sites. In the top figure we provide the total time spent on calculation per step in red, and on communication per step in blue. Here, the total wall-clock time of an identical simulation using 2048 processes only on Huygens is given by the light blue line. Time spent on the four communication phases is given in the bottom figure. These phases are (from top to bottom) the migration of particles between sites, the exchanges of sample particles for determining the site boundaries, the local essential tree exchanges (PP) and the mesh cell exchanges (PM). See Groen et al. (2011) for full details on the communication routines of the code.

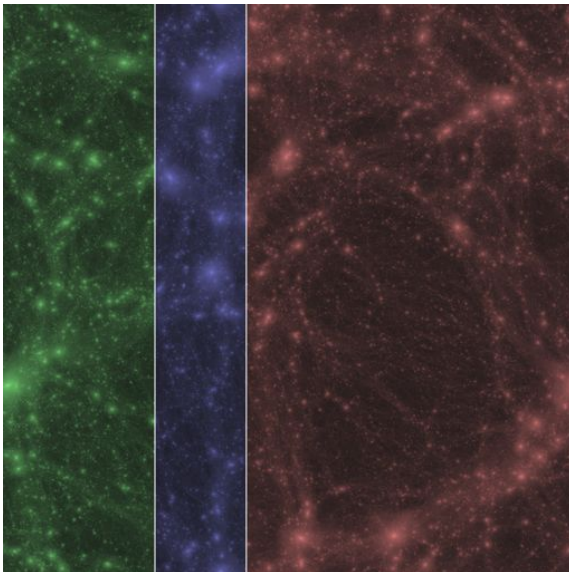


**Figure 2.2:** The final snapshot of the production simulation across three supercomputers, taken at  $z = 0$ . The size of the box is  $30 \times 30 \times 30$  Mpc and the contents are coloured to match the particles residing in Espoo (green, left), Edinburgh (blue, centre) and Amsterdam (red, right) respectively.



---

# 3 | The CosmoGrid Simulation: Statistical Properties of Small Dark Matter Halos

*Based on:*

*Tomoaki Ishiyama, Steven Rieder, Junichiro Makino, Simon Portegies Zwart, Derek Groen, Keigo Nitadori, Cees de Laet, Stephen McMillan, Kei Hiraki and Stefan Harfst*  
*The Cosmogrid Simulation: Statistical Properties of Small Dark Matter Halos*  
*Published in ApJ*

We present the results of the "CosmoGrid" cosmological  $N$ -body simulation suites based on the concordance Lambda Cold Dark Matter ( $\Lambda$ CDM) model. The CosmoGrid simulation was performed in a 30Mpc box with  $2048^3$  particles. The mass of each particle is  $1.28 \times 10^5 M_\odot$ , which is sufficient to resolve ultra-faint dwarfs. We found that the halo mass function shows good agreement with the Sheth and Tormen (1999) fitting function down to  $\sim 10^7 M_\odot$ . We have analysed the spherically averaged density profiles of the three most massive haloes which are of galaxy group size and contain at least 170 million particles.

The slopes of these density profiles become shallower than  $-1$  at the inner most radius. We also find a clear correlation of halo concentration with mass. The mass dependence of the concentration parameter cannot be expressed by a single power law, however a simple model based on the Press-Schechter theory proposed by Navarro, Frenk, and White (1997) gives reasonable agreement with this dependence. The spin parameter does not show a correlation with the halo mass. The probability distribution functions for both concentration and spin are well fitted by the log-normal distribution for haloes with the masses larger than  $\sim 10^8 M_\odot$ . The subhalo abundance depends on the halo mass. Galaxy-sized haloes have 50% more subhaloes than  $\sim 10^{11} M_\odot$  haloes have.

### 3.1 Introduction

According to the present standard  $\Lambda$ CDM model, the universe is thought to be composed primarily of Cold Dark Matter (CDM) and dark energy (White and Rees 1978; Peacock 1999). Structure formation of the universe proceeds hierarchically in this model. Smaller-scale structures collapse first, and then merge into larger-scale structures.

There is serious discrepancy between the distribution of subhaloes in galaxy-sized haloes obtained by numerical simulations and the observed number of dwarf galaxies in the Local Group (Klypin et al. 1999; Moore et al. 1999a). This "missing dwarf problem" is still considered to be one of the most serious problems in the CDM paradigm (e.g., Kroupa et al. 2010). In order to understand the origin of this discrepancy, it is necessary to perform high-resolution cosmological  $N$ -body simulations and obtain unbiased sample of galaxy-sized haloes with resolution high enough to obtain reliable statistics of subhaloes since the subhalo abundance shows large halo-to-halo variations (Ishiyama et al. 2009a).

Cosmological  $N$ -body simulations have been widely used to study the non-linear structure formation of the universe and have been an important tool for a better understanding of our universe. In order to study the spatial correlation of galaxies, the first cosmological  $N$ -body simulations were performed in the 1970s using approximately 1000 particles (e.g., Miyoshi and Kihara 1975; Fall 1978; Aarseth et al. 1979; Efsthathiou 1979). Since then, the development of better simulation algorithms and improvements in the performance of computers allow us to use much larger numbers of particles and have drastically increased the resolution of cosmological simulations.

Today, it is not uncommon that the number of particles exceeds  $10^9$  in high-resolution simulations. In these works, the size of the simulation volumes is typically  $[O(\text{Gpc})]^3$  and populations of galaxy clusters, gravitational lensing, and the baryon acoustic oscillation are studied (e.g., Evrard et al. 2002; Wambsganss et al. 2004; Teyssier et al. 2009; Kim et al. 2009; Crocce et al. 2010). The simulation results are also used to construct mock halo catalogues for next generation large volume surveys. Others use simulations of  $[O(100\text{Mpc})]^3$  volumes to study the internal properties of galaxy-sized dark matter haloes, their formation, evolution, and statistical properties (e.g., Springel et al. 2005; Klypin et al. 2011; White et al. 2010).

Using the results of high-resolution simulations of small-scale structures, we can study the fine structures of galactic haloes, the distribution of subhaloes, their structures, and their dependence on the nature of dark matter. This information has a strong impact on the indirect search for dark matter since gamma-ray flux



by self-annihilation is proportional to local density if we consider neutralino as the candidate of dark matter. Thus, we can restrict the nature of dark matter using the results of high-resolution simulations of small-scale structures and indirect searches of dark matter. In addition, galaxies are considered to form in dark matter haloes with a mass larger than a critical value (Strigari et al. 2008; Li et al. 2009; Macciò et al. 2009; Okamoto and Frenk 2009). The structure of the smallest haloes which can host galaxies is important for the understanding of the galaxy formation processes.

The simulation of smaller-scale structures of dark matter haloes is not a trivial task since a very wide dynamic range of space, mass, and time must be covered. In particular, the number of time steps of such simulations is significantly larger than that of larger-scale simulations since the dynamical time-scale is proportional to  $1.0/\sqrt{G\bar{\rho}}$ , where  $\bar{\rho}$  is the local density. Structures of smaller scales form earlier, and thus have higher densities, therefore, simulations of smaller scales are computationally more expensive.

Recently, simulations with galactic haloes of very high-resolution have been performed (Diemand et al. 2008; Springel et al. 2008; Stadel et al. 2009). These works used the re-simulation method, where one selects one or a few haloes at  $z = 0$  from a simulation which covers a large volume (typically a cube of size  $O(100\text{Mpc})$ ) with a relatively low-resolution. The corresponding regions of these haloes are then identified in the initial particle distribution, and the particles in these regions are replaced by a larger number of smaller particles. After this is done, the entire volume is simulated to  $z = 0$  again.

With this re-simulation method, we can resolve the structures of selected haloes with extremely high resolution (Diemand et al. 2008; Springel et al. 2008; Stadel et al. 2009). However, this method cannot be used for the study of halo-to-halo variations. Different haloes are born in different environments and grow differently. The difference in the environment and growth history must be the cause of halo-to-halo variations. Therefore, in order to study variations, we need a bias-free set of a large number of haloes. Clearly one cannot obtain a large number of haloes with re-simulation method in practical time.

In principle, one can improve the statistics by increasing the number of haloes selected for re-simulations. In order to avoid the selection bias, we need to apply random, bias-free selection, and the most reliable bias-free selection is to select all haloes, in other words, to simulate the entire simulation box with uniformly high mass resolution. Ishiyama et al. (2009a) performed the first bias-free high resolution simulation of small-scale structures. They analysed the statistics of the subhalo abundance using the complete set of haloes in the simulation box. The number of particles was  $1600^3$  in a  $46.5\text{Mpc}$  cubic box and the mass of a particle was  $10^6 M_{\odot}$ .

The subhalo abundance showed large halo-to-halo variations (see also Ishiyama et al. 2008; Boylan-Kolchin et al. 2010). The concentration parameter and the radius at the moment of the maximum expansion showed fairly a tight correlation with the subhalo abundance. Halos formed earlier have a smaller number of subhaloes at present. This correlation suggests that the difference in the formation history is the origin of the variation of the subhalo abundance (see also Gao et al. 2004; van den Bosch et al. 2005; Zentner et al. 2005).

The Millennium-II simulation (Boylan-Kolchin et al. 2009) used a 137Mpc cubic box and the particle mass of  $\sim 9.45 \times 10^6 M_\odot$ . Its result is suitable for the analysis of the statistics of galaxy-sized dark matter haloes, because the number of haloes is larger than that of Ishiyama et al. (2009a). However, due to the lack of the mass resolution, it cannot be used to study the statistics of dwarf-galaxy-sized haloes and the statistics of subhaloes with the size larger than faint dwarf galaxy.

In this paper, we describe the first result of our CosmoGrid simulation. We simulated the evolution of haloes in a 30Mpc cubic box using  $2048^3$  particles. The mass of one particle is  $1.28 \times 10^5 M_\odot$ . The resolution reaches down to ultra-faint dwarf-galaxy-sized haloes ( $\sim 10^7 M_\odot$ ) and is more than eight times better than that of our previous simulation (Ishiyama et al. 2009a). We focus on the halo mass function with the mass down to  $10^7 M_\odot$ , the structures of most massive haloes, and statistics of the internal properties of dwarf-galaxy-sized haloes. We describe our initial conditions and numerical settings in Section 3.2, and results in Section 3.3. We discuss and summarize our results in Section 3.4.

## 3.2 Initial Conditions and Numerical Method

The cosmological parameters adopted are based on the concordance  $\Lambda$ CDM cosmological model ( $\Omega_0 = 0.3$ ,  $\Omega_\Lambda = 0.7$ ,  $h = 0.7$ ,  $\sigma_8 = 0.8$ ,  $n = 1.0$ ). These values are the same as those used in our previous simulation (Ishiyama et al. 2009a). We used a periodic cube of the co-moving size of 30Mpc. The number of particles for the largest run is  $2048^3$  which corresponds to a mass resolution of  $1.28 \times 10^5 M_\odot$ . To generate the initial particle distributions, we used the MPGRAFIC package (Prunet et al. 2008), which is a parallelised variation of the GRAFIC package (Bertschinger 2001). The initial redshift was 65.

In order to investigate the effect of the mass and spatial resolution, we performed two simulations with lower resolution. We generated the initial conditions for these low-resolution runs (CG1024 and CG512) by replacing 8 or 64 particles in the high-resolution initial condition (CG2048) with a single particle 8 or 64 times more massive. We did not use any smoothing filter for density and velocity spaces. The massive particles were picked up at regular intervals before perform-

**Table 3.1:** Run Parameters. Here,  $N$ ,  $L$ ,  $\varepsilon$ , and  $m$  are the total number of particles, the box length, the softening length, the mass resolution.

Name	$N$	$L(\text{Mpc})$	$\varepsilon(\text{pc})$	$m(M_\odot)$
CG2048	$2048^3$	30.0	175	$1.28 \times 10^5$
CG1024	$1024^3$	30.0	350	$1.03 \times 10^6$
CG512	$512^3$	30.0	700	$8.21 \times 10^6$
IFM2009 (Ishiyama et al. 2009a)	$1600^3$	46.5	700	$1.00 \times 10^6$

**Table 3.2:** Global Parameters of Three Most Massive Group Sized Halos at  $z = 0$ . Here,  $M$ ,  $N$ ,  $R_{\text{vir}}$ ,  $R_{\text{vmax}}$ , and  $V_{\text{max}}$  are the mass, the number of particles, the virial radius in which the spherical overdensity is 101 times the critical value, the radius where the rotation velocity is maximum, and the maximum rotation velocity, respectively.

Name	Run	$M(10^{13}M_\odot)$	$N$	$R_{\text{vir}}(\text{kpc})$	$R_{\text{vmax}}(\text{kpc})$	$V_{\text{max}}(\text{kms}^{-1})$
GP1	CG2048	5.24	408499843	969	200	596
	CG1024	5.19	50632942	966	186	589
	CG512	5.22	6361253	968	184	596
GP2	CG2048	3.58	279382586	854	305	476
	CG1024	3.57	34836692	853	279	472
	CG512	3.57	4347651	852	294	475
GP3	CG2048	2.25	175752770	731	178	434
	CG1024	2.26	22072073	732	187	431
	CG512	2.25	2746874	731	192	434

ing the Zel'dovich approximation. This procedure introduces some aliasing noise in the high frequency limit of CG1024 and CG512 runs. The corresponding halo contains less than a few hundred particles. However, here we use CG1024 and CG512 runs for only convergence studies, and analyse haloes with the particles larger than  $\sim 1000$ . Thus, the effect of the aliasing noise should be negligible. In Table 3.1, we summarize parameters used in our simulations.

We used a leapfrog integrator with shared and adaptive time steps. The step size was determined as  $\min(2.0\sqrt{\varepsilon/|\vec{a}_i|}, 2.0\varepsilon/|\vec{v}_i|)$  (minimum of these two values for all particles). All particles have the same time-steps. The gravitational Plummer softening length  $\varepsilon$  was 175pc at  $z = 0$ . The softening was constant in co-moving coordinates from  $z = 65$  (initial condition) to  $z = 10$ . From  $z = 10$  to  $z = 0$ , it was constant in physical coordinates. This procedure is similar to that used in Kawai et al. (2004).

For the largest simulation, we used four supercomputers. Three of them are Cray XT4 machines at the Center for Computational Astrophysics of National Astronomical Observatory of Japan, the Edinburgh Parallel Computing Centre in Edinburgh (United Kingdom) and IT Center for Science in Espoo (Finland). The

fourth machine is an IBM pSeries 575 at SARA in Amsterdam (the Netherlands). Part of the calculation was done in a "grid" computing environment, in which we used more than one machine simultaneously for one run (Portegies Zwart et al. 2010a).

For the time integration we used the GreeM code (Ishiyama et al. 2009b) for single supercomputer runs and the SUSHI code (Groen et al. 2011) for multi-supercomputer runs. The GreeM code is a massively parallel TreePM code based on the parallel TreePM code of Yoshikawa and Fukushige (2005) for large cosmological  $N$ -body simulations. The long range forces are calculated by the PM method (Hockney and Eastwood 1981), and the short range forces are calculated by the Barnes-Hut-Tree method (Barnes and Hut 1986). Yoshikawa and Fukushige (2005) used a 1-D slab decomposition, but in GreeM we use a 3-D multi-section decomposition (Makino 2004) to improve its scalability. In addition, the decomposition is based on CPU time measurement, so that near ideal load balance is archived. The SUSHI code is an extension of the GreeM code which can run concurrently on multiple supercomputers. It uses the MPWide communication library (Groen et al. 2010) running on Global Lambda Integrated Facility (GLIF) (DeFanti et al. 2003) to facilitate message passing between distributed supercomputers. We used  $512^3$  PM grid points for PM calculations, the opening angle for the tree method was 0.3 from initial to  $z = 10$ , and 0.5 from  $z = 10$  to  $z = 0$ .

The calculation time was  $\sim 180$ s per step with 1024 CPU cores for the largest run on the Cray XT4 in Japan and  $\sim 140$ s per step with 2048 CPU cores on the IBM pSeries 575 in the Netherlands. We spent about 3.5 million CPU hours to perform all the 60,283 steps in our simulation.

We used the spherical overdensity method (Lacey and Cole 1994) to identify haloes and calculated the halo virial radius  $R_{\text{vir}}$ . The virial radius of a halo is defined as the radius in which the spherical overdensity is  $\Delta(z)$  times the critical value. The overdensity  $\Delta(z)$  is given by the analytic formula (Bryan and Norman 1998),

$$\Delta(z) = (18\pi^2 + 82x - 39x^2)/\Omega(z), \quad (3.1)$$

where  $x \equiv \Omega(z) - 1$ . The mass of a halo is defined as interior mass within the virial radius.

The mass of the most massive halo is  $5.24 \times 10^{13} M_{\odot}$ . It contains  $4.08 \times 10^8$  particles. Via Lactea I, II (Diemand et al. 2007, 2008), and Aquarius simulations (Springel et al. 2008) used  $\sim 10^8$ ,  $\sim 5 \times 10^8$ , and  $\sim 10^9$  particles for the largest halo. Table 3.2 shows the properties of the three most massive haloes in our simulation.

The subhalo finder is the same as that described in Ishiyama et al. (2009a). Our method is based on the idea of finding all local potential minima. Initially, all

particles are candidates for the centres of haloes. We then search for the particle with the smallest (most negative) potential and regard it as the centre of a halo. We then exclude  $n_{\min}$  neighbour particles of this particle from the list of remaining particles, and search the particle with the smallest potential from the list. At this time, we again search  $n_{\min}$  neighbour particles from the list of originally selected particles, and if the potential of one neighbour is smaller, we do not add this particle to the list of haloes. However, we remove  $n_{\min}$  neighbours no matter whether the particle is added to the list or not. We repeat this procedure until there is no remaining particle. We set  $n_{\min}$  so that  $n_{\min} \times m = 1.0 \times 10^7 M_{\odot}$ , where  $m$  is the mass of each particle.

Figure 3.1 shows the snapshots at  $z = 0$ . In Figure 3.2, we also present the time evolution of the whole box and that of the most massive halo. The three most massive haloes in simulations with three different resolutions are shown in Figure 3.3. The positions of subhaloes agree very well in three simulations. Of course, there are some discrepancies near the centres of haloes. In particular, whereas there is only one core in the centre of the second massive halo (GP2) of CG2048, there are two cores in GP2 of CG1024 and CG512.

The reason of this difference is that the formation history of this halo is rather violent. It experienced many mergers near  $z = 0$  in the centre of the halo and is far from the relaxed state. The difference of the accuracy of integration changed the time-scale of the mergers of the haloes with three different resolutions. At  $z = 0$ , the halo GP2 has just completed the merger in the CG2048 run, whereas the same merger event is still on-going in CG1024 and CG512 runs. If we consider the spherically averaged density profile of the halo, the difference becomes important (see Section 3.3.2).

## 3.3 Results

### 3.3.1 Mass Function

Press and Schechter (1974) established a recipe to derive the number of dark matter haloes based on the hierarchical clustering model. Since then, a number of analytic formulae for the mass function have been proposed. Many of them are designed to give a good agreement with results of high-resolution  $N$ -body simulations (e.g., Sheth and Tormen 1999; Jenkins et al. 2001; Reed et al. 2003; Yahagi et al. 2004; Warren et al. 2006; Tinker et al. 2008, and references therein).

These formulae can reproduce the mass function between  $10^{10} M_{\odot}$  and cluster scale very well. Here, we examine the mass function of mass below  $10^{10} M_{\odot}$  down to  $10^7 M_{\odot}$ . The mass function of this range has been studied only in high redshift

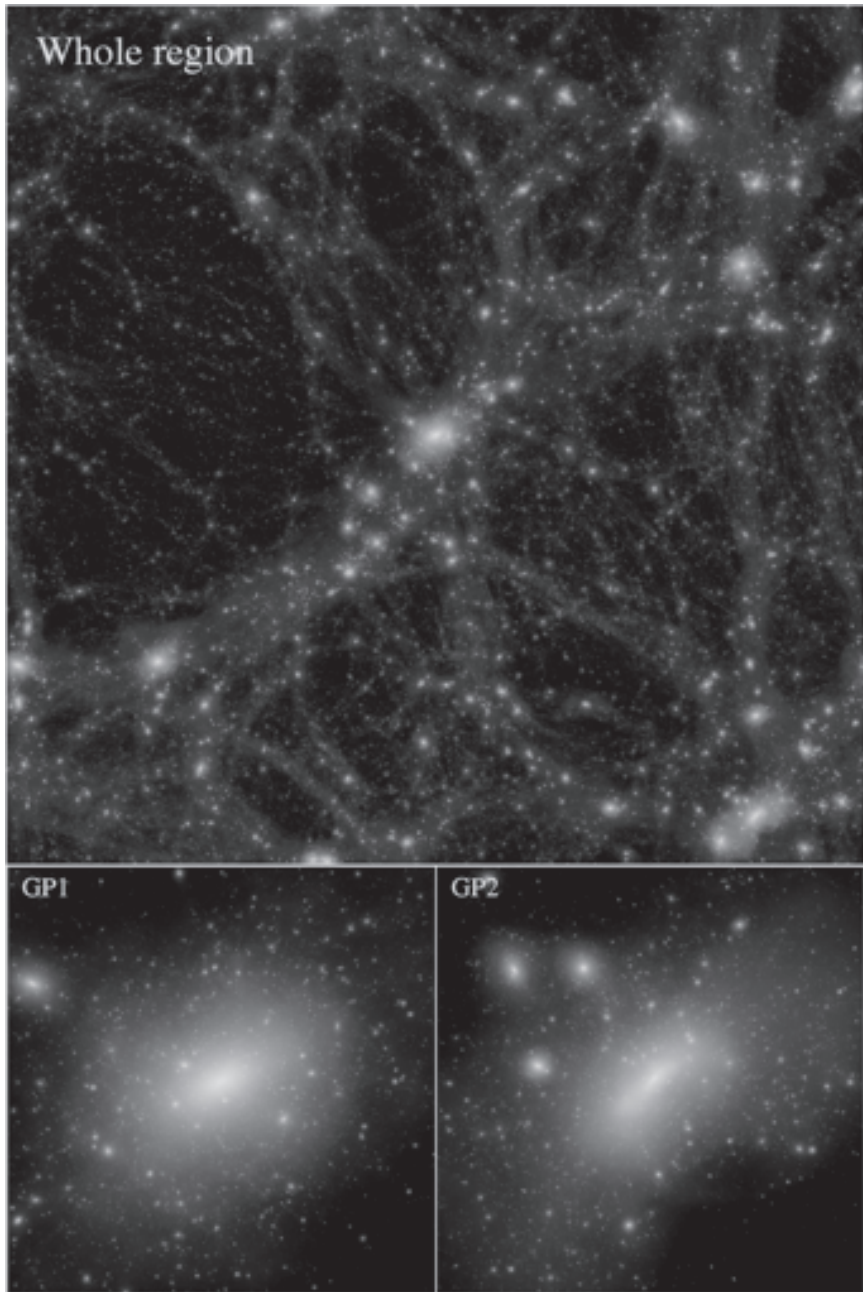


**Figure 3.1:** Projected density of dark matter at  $z = 0$  in our largest simulation ( $2048^3$  particles). Top panel shows the whole region with the volume of  $(30\text{Mpc})^3$ . Bottom panels show the projected density of the two most massive group sized haloes. These volumes are  $(2\text{Mpc})^3$ .

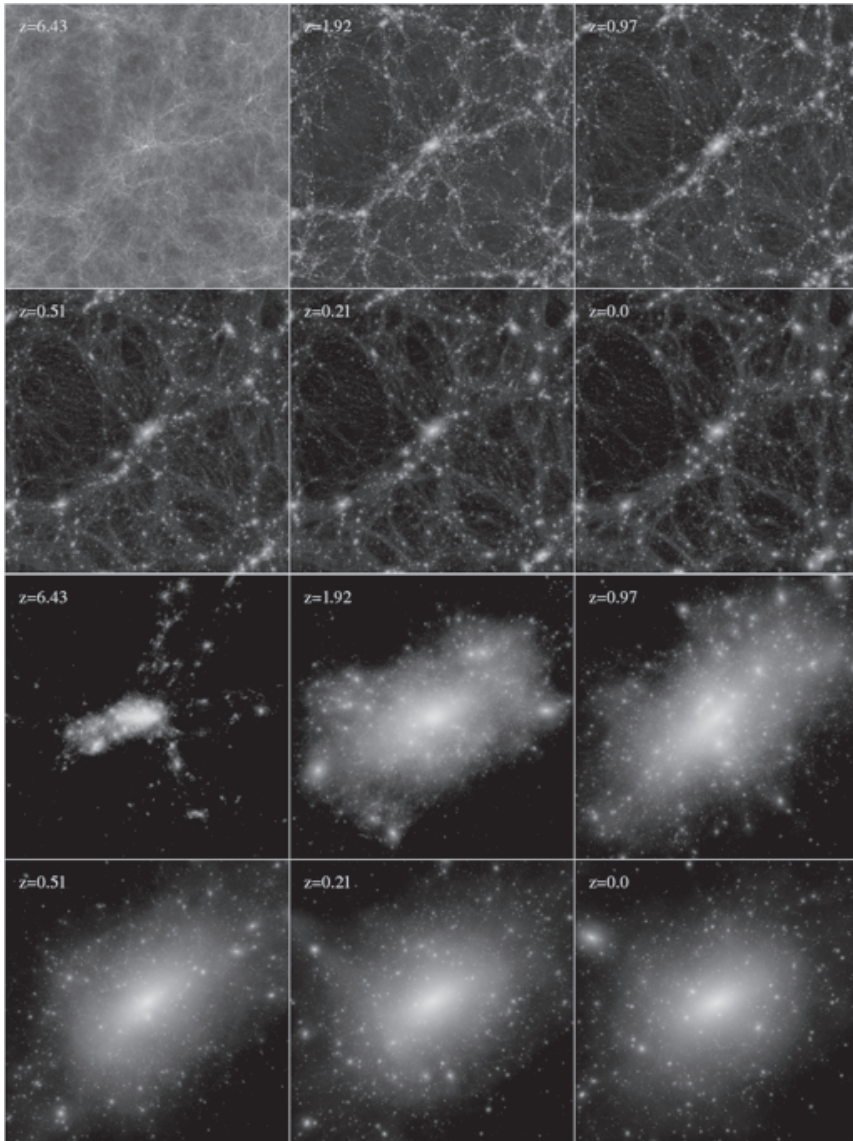


**Figure 3.2:** Evolution pictures of our largest simulation. Top six panels show the evolution of the whole region. Bottom six panels show the evolution of the most massive halo.

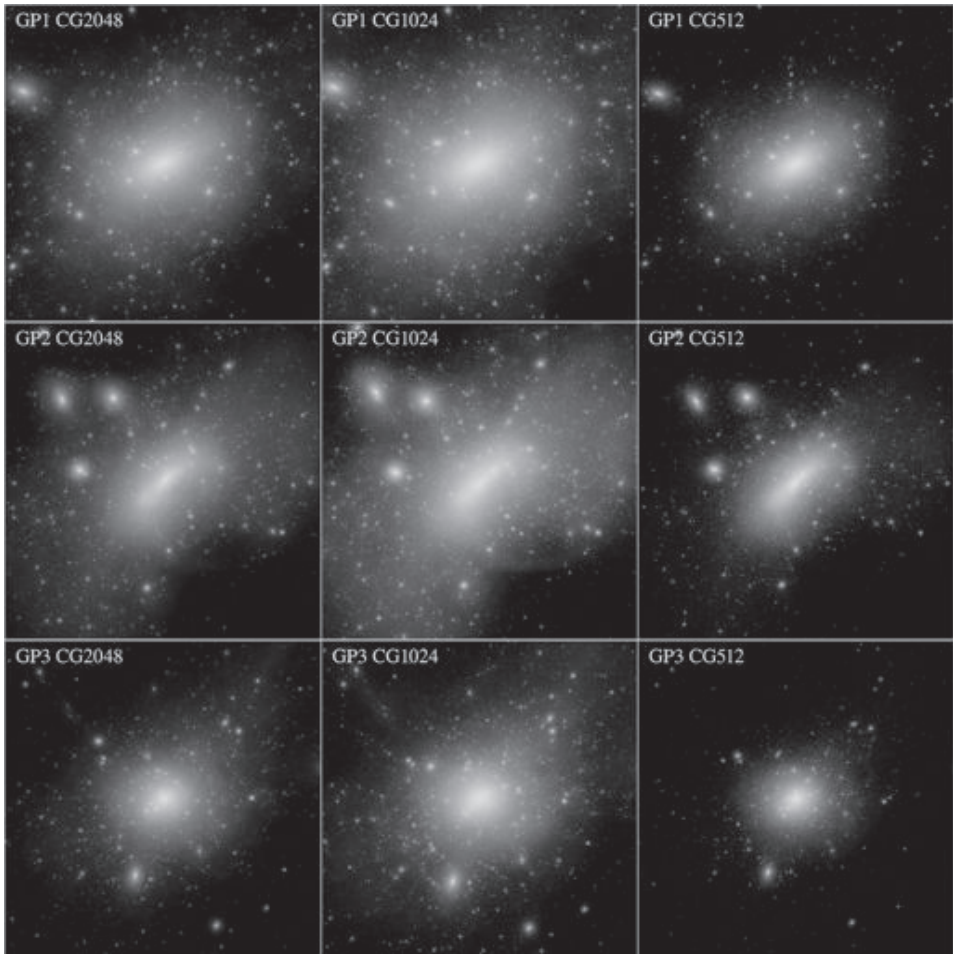


**Figure 3.3:** Projected density of dark matter at  $z = 0$ . Each row shows one of the three most massive haloes with mass decreasing from top to bottom. Columns show different resolution from highest (left) to lowest (right).



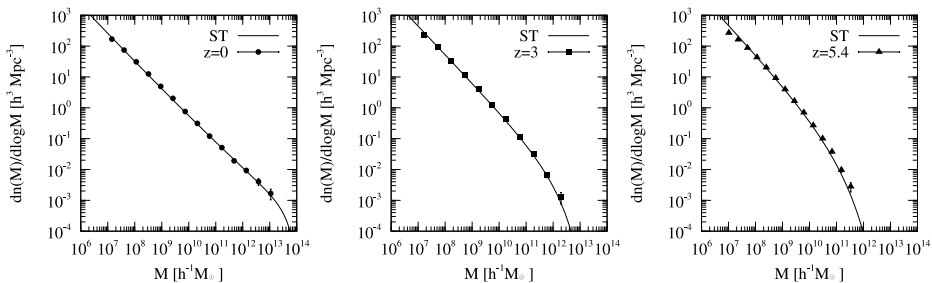


**Figure 3.4:** Mass function of our largest simulation (CG2048). The results of  $z = 0.0$  (left),  $z = 3.0$  (middle), and  $z = 5.4$  (right) are shown. Solid curves are the Sheth and Tormen (1999) function. Error bars are Poisson errors.

(e.g., Reed et al. 2007; Lukić et al. 2007).

Figure 3.4 shows the halo mass functions at three different redshifts for the CG2048 run and the prediction of Sheth & Tormen formula (ST, Sheth and Tormen 1999). The agreement is very good for the mass from  $\sim 10^7 M_\odot$  to  $M = 1.0 \times 10^{13} M_\odot$  at  $z = 0$ . The difference is less than 10% for  $M = 5.0 \times 10^7 M_\odot$  to  $M = 2.0 \times 10^{12} M_\odot$  at  $z = 0$ ,  $M = 5.0 \times 10^7 M_\odot$  to  $M = 5.0 \times 10^{10} M_\odot$  at  $z = 3$ , and  $M = 8.0 \times 10^7 M_\odot$  to  $M = 4.0 \times 10^9 M_\odot$  at  $z = 5.4$ .

Our results imply that the mass function is well represented by the ST function down to  $10^7 M_\odot$ . However, our simulations have a slightly larger number of haloes than the number predicted by the ST formula in particular at the high-mass end of the  $z = 5.4$  mass function. Note that the finite volume of our simulation (the box length is 30Mpc) might affect the mass function in some degrees. The absence of long-wavelength perturbations might increase the number of intermediate mass haloes by about 10% (Bagla and Prasad 2006; Power and Knebe 2006). In order to test the effect of the box size, we performed additional simulations of 30, 45, and 60Mpc boxes with  $512^3$  particles. The left panel of Figure 3.5 shows mass functions of these simulations at  $z = 5.4$  relative to the ST formula. The difference becomes larger as the halo mass and the box size increase. The right panel of Figure 3.5 shows mass functions relative to the 30Mpc simulation. We can see that the number of haloes of the 30Mpc box simulation is systematically larger than those of the 45Mpc and 60Mpc box simulations. The mass functions of the 45Mpc and 60Mpc box simulations are well converged for haloes larger than  $2.0 \times 10^{10} M_\odot$ , which is the limit of resolution for the 60Mpc box simulation. We can conclude that the larger number of haloes seen in CG2048 at the high-mass end is caused by the absence of long-wavelength perturbations.

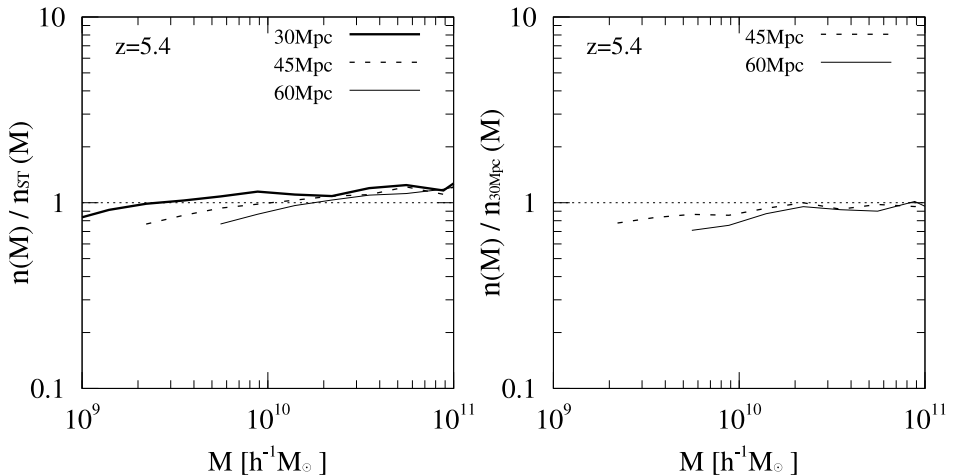


**Figure 3.5:** Left panel shows three mass functions at  $z = 5.4$  derived from  $512^3$  simulations of 30, 45, and 60 Mpc boxes, relative to the Sheth and Tormen (1999) function. Right panel shows mass functions of 45 and 60 Mpc boxes simulations, relative to that of the 30 Mpc box simulation.

### 3.3.2 Density Structures of Most Massive Halos

Many groups have studied the density profile of dark matter haloes using high-resolution cosmological  $N$ -body simulations (e.g., Navarro et al. 1997; Fukushige and Makino 1997; Moore et al. 1999b; Ghigna et al. 2000; Jing and Suto 2000; Jing 2000; Fukushige and Makino 2001; Klypin et al. 2001; Taylor and Navarro 2001; Jing and Suto 2002; Power et al. 2003; Fukushige and Makino 2003; Fukushige et al. 2004; Diemand et al. 2004; Hayashi et al. 2004; Navarro et al. 2004; Diemand et al. 2005; Reed et al. 2005; Kazantzidis et al. 2006; Merritt et al. 2006; Diemand et al. 2008; Gao et al. 2008; Stadel et al. 2009; Navarro et al. 2010). In most of recent works, the slopes of radial density profiles were around  $-1$  in the inner region and around  $-3$  in the outer region. The slope of density became shallower as the radius becomes smaller. Thus, the central slope is not described by any single power. Furthermore, the density profile was not universal. In other words, the slope showed a significant halo-to-halo scatter.

Recent studies (Stadel et al. 2009; Navarro et al. 2010) based on high-resolution simulations of galactic haloes showed that the slopes of density became less than  $-1$  at the radius 0.001 times the virial radius of the halo as predicted by early works (e.g. Graham et al. 2006). Einasto profile showed better agreement than the NFW profile which has been widely used for modelling dark matter haloes because of its simplicity.

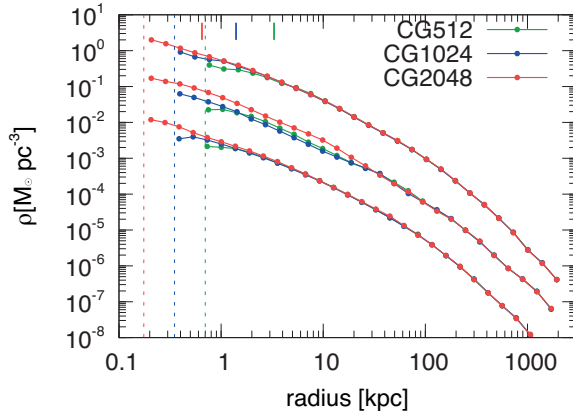


**Figure 3.6:** Spherically averaged radial density profiles of largest three haloes at  $z = 0$ . Two of three profiles (middle and bottom) are vertically shifted downward by 1 and 2 dex. Vertical dashed lines show the softening length of three simulations. Upside short vertical bars indicate the reliability limit of the most massive halo calculated using criterion proposed by Fukushige and Makino (2001) and Power et al. (2003). Red, blue, and green correspond to the CG2048, CG1024, and CG512 simulations, respectively.

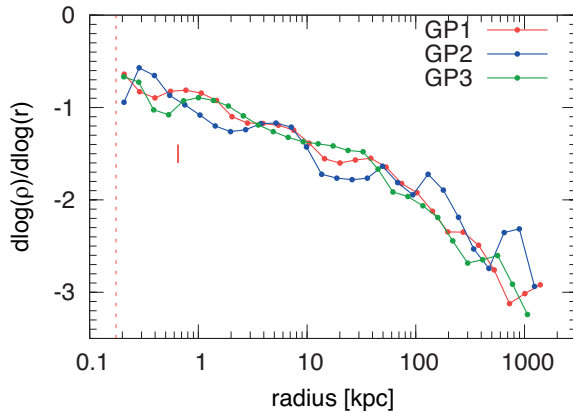
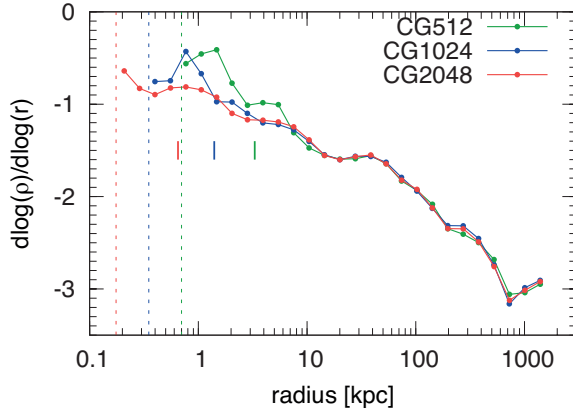


**Figure 3.7:** Slopes of radial density profiles of largest three haloes at  $z = 0$ . Top panel shows those of the largest halo for three different resolutions. Bottom panel shows those of the largest three haloes for the largest simulation (CG2048).

Almost all recent high-resolution simulations of single haloes used galaxy-sized haloes. Therefore, little is known if these findings can be applied to haloes of different masses. Here, we present the density profiles of three most massive haloes in our simulation. These haloes are galactic group-sized ones, with the mass of 5.24, 3.58, and  $2.25 \times 10^{13} M_{\odot}$ . They contain 408, 279, and 176 million particles.

Figure 3.6 shows the spherically averaged density profiles of these haloes at  $z = 0$ . We can see that the results of three simulations with different resolution are indistinguishable for radii larger than the reliability limits, except for the second massive halo. We calculated the reliability limits using the criterion proposed by Fukushima and Makino (2001) and Power et al. (2003). We cannot ignore the effects of the local two-body relaxation for radii smaller than these limits. As can be seen in Figure 3.3, the slight difference of the merging epoch of the central cores caused this difference.

The slopes of density profiles become gradually shallower as the radius becomes smaller. The top panel of Figure 3.7 shows the slopes of density profiles of the most massive halo. As in the case of the density profile itself, the slopes also agree well with each other. The bottom panel of Figure 3.7 shows the slopes of the three most massive haloes in the CG2048 run.

These profiles are significantly different from those of galactic haloes in recent other high-resolution simulations, even if the halo mass is scaled to be the same. The mass of the haloes of Aquarius simulation (Springel et al. 2008) or GHALO simulation (Stadel et al. 2009) is  $\sim 10^{12} M_{\odot}$ , which is an order of magnitude smaller than our three haloes. The slope at  $0.001 R_{\text{vir}}$  is  $-0.9 \sim -1.0$  for our three haloes. This value is in excellent agreement with the result of both simulations. Both of them gave the slope  $-1.0$  for  $r = 0.001 r_{200}$ . This agreement does not mean the density profile obtained by these simulation and those by our simulation are identical. The concentration parameter, which we define here as  $c_{\text{vmax}} = R_{\text{vir}}/R_{\text{vmax}}$ , is 4.8, where  $R_{\text{vir}}$  and  $R_{\text{vmax}}$  are the halo virial radius and the radius of the maximum rotational velocity. This value is significantly smaller than that of Aquarius A-1 halo. Thus, the Aquarius halo is significantly more centrally concentrated, and yet the slope at  $r = 0.001 R_{\text{vir}}$  is the same. Thus the rate of the shallowing of the slope is somewhat faster for the Aquarius halo than for our CG2048 haloes. Most likely, this difference is due to the difference in the mass of the halo.

### 3.3.3 Concentration Distributions

The concentration parameter has been widely used to describe the internal structure of haloes since it is tightly correlated with the formation epoch (Wechsler

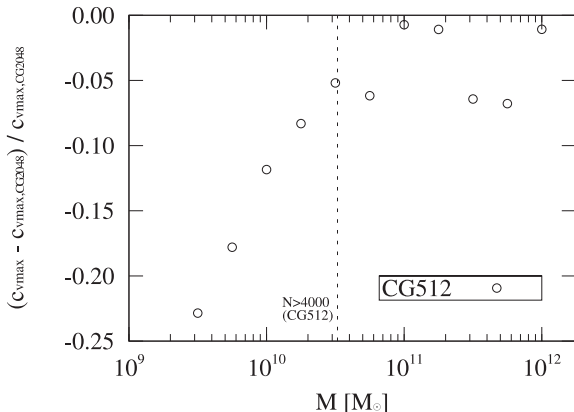


**Figure 3.8:** Residuals of concentration  $c_{\text{vmax}} = R_{\text{vir}}/R_{\text{vmax}}$  from the largest simulation (CG2048) to the lower resolution simulation (CG512).

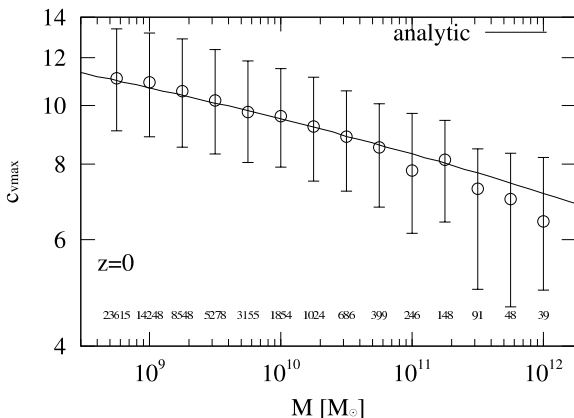


**Figure 3.9:** Concentration plotted against the halo virial mass  $M$  at  $z = 0$ . Circles show the median value on each bin. Whiskers are the first and third quartiles. The number of haloes on each bin is shown below circles. Thick solid line shows the result from an analytical model.

et al. 2002). Usually, the concentration is parametrised assuming that the density profiles of haloes can be fitted by the NFW profile (Navarro et al. 1997),

$$\rho(r) = \frac{\rho_0}{(r/r_s)(1 + r/r_s)^2}, \quad (3.2)$$

where  $\rho_0$  is a characteristic density and  $r_s$  is a scale radius. The concentration  $c_{\text{NFW}} = R/r_s$  is widely used (e.g., Bullock et al. 2001b; Zhao et al. 2003; Macciò et al. 2007; Neto et al. 2007; Macciò et al. 2008; Zhao et al. 2009; Muñoz-Cuartas et al. 2011). It is known that  $c_{\text{NFW}}$  depends weakly on the halo mass. Halos with higher mass have smaller concentration, since the average density of a halo reflects the cosmic density at its formation time. The dependence is weaker for higher redshift (Zhao et al. 2003).

The concentration based on the NFW profile is affected by fitting ranges and resolution (Neto et al. 2007). Furthermore, recent high-resolution simulations showed that the density profile is significantly different from the NFW profile

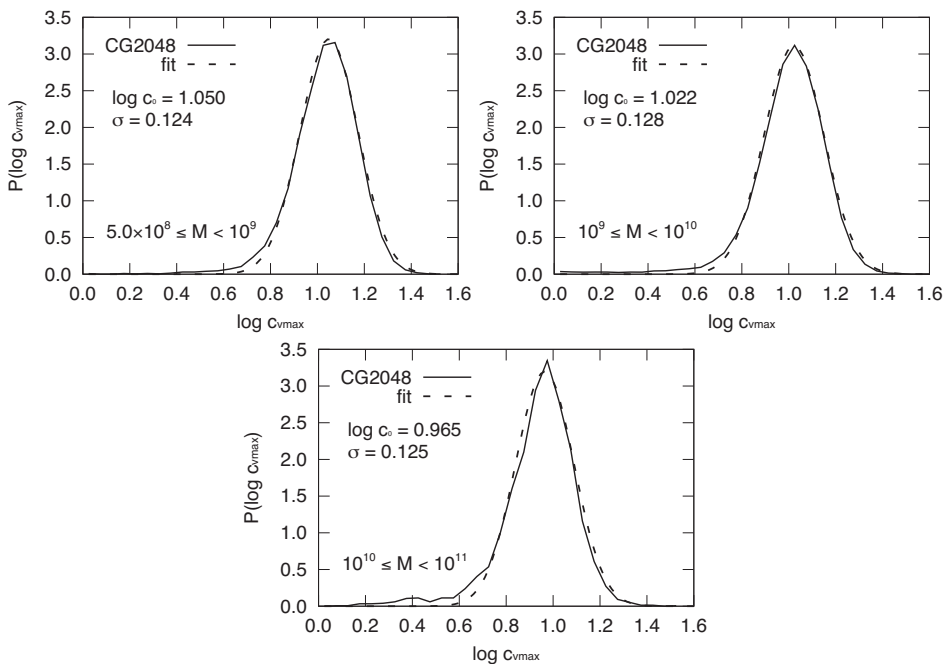


**Figure 3.10:** The probability distribution functions of the concentration at  $z = 0$ . These panels show the results of different mass ranges. Dashed curves are the best fits of the log-normal distribution.

(Stadel et al. 2009; Navarro et al. 2010, also see Section 3.3.2). Thus, the use of  $c_{\text{nfw}}$  might cause some systematic bias (Gao et al. 2008; Reed et al. 2011).

We use the concentration  $c_{\text{vmax}}$  defined in Section 3.3.2, which is a simpler quantity to measure the concentration. Note that  $R_{\text{vmax}}$  can be easily determined directly from spherically averaged mass distribution without the need of any fitting formulae. If the density profile is represented by the NFW profile, either concentration can be converted to the other.

First, we determine the minimum number of particles in a halo necessary to reliably determine the concentration. Figure 3.8 shows the normalized difference of average concentration between the G2048 run and the CG512 run as the function of halo mass. We can see that the difference is  $\sim 0.05$  for the halo mass larger than  $3.0 \times 10^{10} M_{\odot}$ . For halo mass less than  $3.0 \times 10^{10} M_{\odot}$ , the difference is larger. In the CG512 run, a halo of mass  $3.0 \times 10^{10} M_{\odot}$  contains  $\sim 4000$  particles. So we conclude that we need  $\sim 4000$  particles to reliably determine the concentration. For the CG2048 run, the reliability limit is  $5.0 \times 10^8 M_{\odot}$ .

Figure 3.9 shows the median, and first and third quantiles of the concentration

as a function of the virial mass of the halo. We can see a clear correlation between the halo mass and the concentration. Apparently, the dependence is weaker for smaller mass. Therefore, the fitting functions with a single power (e.g., Bullock et al. 2001a; Neto et al. 2007; Macciò et al. 2007; Klypin et al. 2011) cannot be used for haloes of the size of dwarf galaxies.

Theoretically, the concentration of a halo reflects the cosmic density at the formation time of the halo (Bullock et al. 2001a). The concentrations of haloes formed earlier are higher than that of haloes formed later. However, the dependence should be weak for small haloes since the dependence of the formation epoch to the halo mass is small for small (smaller than  $10^8 M_\odot$ ) haloes. The slope of the power spectrum of initial density fluctuations approaches to  $-3$  for small mass limit.

In Figure 3.9, we also plot an analytical prediction of the mass--concentration relation, obtained by the method used in Navarro et al. (1997) assuming that all haloes have the NFW profile. The formation redshift  $z_f$  of haloes with the mass  $M$  is defined as the epoch at which progenitors with the mass larger than  $fM$  first contained the half of the mass  $M$ . It is estimated by using the Press-Schechter formalism (e.g., Lacey and Cole 1993),

$$\operatorname{erfc} \left\{ \frac{\delta_{\text{crit}}(z_f) - \delta_{\text{crit}}(0)}{\sqrt{2 [\sigma_0^2(fM) - \sigma_0^2(M)]}} \right\} = \frac{1}{2}, \quad (3.3)$$

where  $\delta_{\text{crit}}(z)$  is the critical overdensity for the spherical collapse at  $z_f$ , and  $\sigma_0^2(M)$  is the variance of the density fluctuation at  $z = 0$  smoothed by a top-hat filter on a mass scale of  $M$ . Here, we used  $f = 0.01$ . The characteristic density  $\rho_0$  of a halo should reflect the cosmic density at the formation time. Thus, we assume

$$\rho_0 = \rho_{\text{norm}} (1 + z_f)^3, \quad (3.4)$$

where  $\rho_{\text{norm}}$  is chosen to fit the simulation results. The mass of a halo with the NFW profile is given by

$$M = 4\pi\rho_0 r_s^3 [\ln(1+c) - c/(1+c)]. \quad (3.5)$$

The mass and concentration at  $z = 0$  are related to each other by

$$M = \frac{4}{3}\pi R_{\text{vir}}^3 \Delta(0) \rho_{\text{crit}} = \frac{4}{3}\pi r_s^3 c^3 \Delta(0) \rho_{\text{crit}}, \quad (3.6)$$

where  $\rho_{\text{crit}}$  is the critical density. From Equations 3.1, 3.3, 3.4, 3.5, and 3.6, we can analytically estimate the concentration of haloes with the mass  $M$ .

As mentioned by Lacey and Cole (1993), the estimated formation epoch obtained using Equation 3.3 is not necessarily correct. This is because the formation time defined here corresponds to the epoch at which one of progenitors has a mass larger than  $fM$ . This does not mean that the main progenitor has this mass. Nevertheless, as seen in Figure 3.9, the analytical prediction based on Equation 3.3 shows a very good agreement with the result from CG2048 run for haloes with mass smaller than  $10^{11}M_{\odot}$ . For haloes with the mass larger than  $10^{11}M_{\odot}$ , the difference between CG2048 results and analytical ones are relatively large. However, these haloes are rare objects in CG2048 run, and the fact might affect the results in some degrees. We can conclude that the shallowing slope of the mass-concentration relation naturally emerges from the nature of the power spectrum of initial density fluctuations.

The slope is slightly shallower than that of  $c_{\text{NFW}}$  for larger haloes. For the case of  $c_{\text{NFW}}$ , the slope is around  $-0.10$  for relaxed haloes and  $-0.11$  for all haloes (Neto et al. 2007; Macciò et al. 2007). On the other hand, for the CG2048 simulation, the slope is around  $-0.07$  for haloes with the mass  $10^{10}M_{\odot}$ , and  $-0.06$  for haloes with the mass  $10^9M_{\odot}$ . Note that one overestimates the central density of haloes if one estimates the concentration of dwarf-sized haloes by extrapolating the mass-concentration relation of galaxy or cluster-sized haloes.

Figure 3.10 shows the probability distribution functions of the concentration parameter at  $z = 0$  in three different mass ranges. Both shapes are well fitted by the log-normal distributions,

$$P(\log c_{\text{vmax}}) = \frac{1}{\sqrt{2\pi}\sigma} \exp\left(-\frac{\log^2(c_{\text{vmax}}/c_0)}{2\sigma^2}\right). \quad (3.7)$$

We find  $\log c_0 = 1.050$ ,  $\sigma = 0.124$  for haloes with the mass of  $5.0 \times 10^8 M_{\odot} \leq M < 10^9 M_{\odot}$ ,  $\log c_0 = 1.022$ ,  $\sigma = 0.128$  for haloes with the mass of  $10^9 M_{\odot} \leq M < 10^{10} M_{\odot}$ , and  $\log c_0 = 0.965$ ,  $\sigma = 0.125$  for haloes with the mass of  $10^{10} M_{\odot} \leq M < 10^{11} M_{\odot}$ .

### 3.3.4 Spin Distributions

The dimensionless spin parameter is a good parameter to quantify the rotation of a halo. One often uses the spin parameter defined in Bullock et al. (2001a),

$$\lambda = \frac{J}{\sqrt{2}MVR}, \quad (3.8)$$

where  $M$ ,  $R$ ,  $V$ , and  $J$  are the virial mass of the halo, radius, rotational velocity at  $R$ , and total angular momentum inside  $R$ .



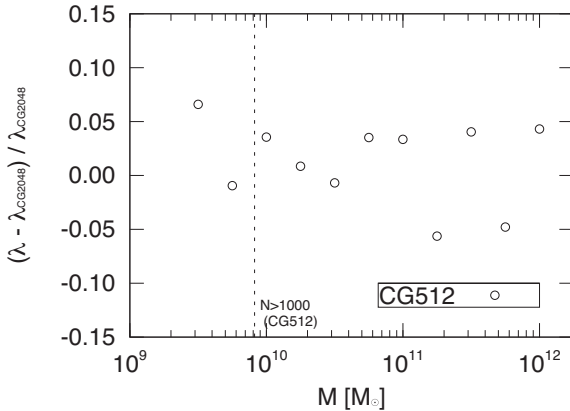


**Figure 3.11:** Residuals of spin from the largest simulation (CG2048) to lower resolution simulation (CG512).

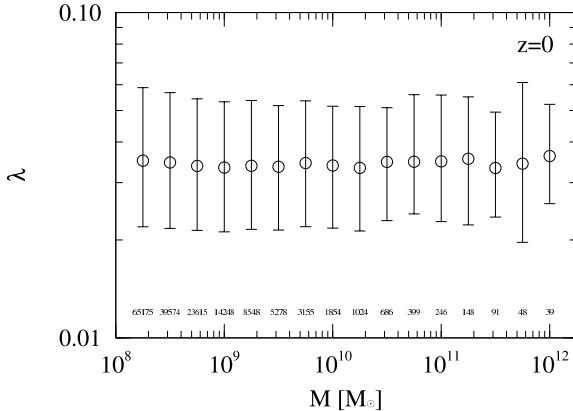


**Figure 3.12:** Spin parameter  $\lambda$  plotted against the halo virial mass  $M$  at  $z = 0$ . Circles show the median value on each bin. Whiskers are the first and third quantiles. The number of haloes on each bin is shown below circles.

The distribution, the dependence on the halo mass, and the evolution have been studied by a number of works (e.g., Bullock et al. 2001a; Bailin and Steinmetz 2005; Bett et al. 2007; Macciò et al. 2007; Knebe and Power 2008; Macciò et al. 2008; Antonuccio-Delogu et al. 2010; Muñoz-Cuartas et al. 2011; Wang et al. 2011). The spin of galaxy-sized haloes is well studied by using the results of sufficient resolution simulations. However, we do not understand those of dwarf-galaxy-sized haloes. The spin distribution of those haloes at only high redshifts is studied by the result of high-resolution simulation (Knebe and Power 2008). Here, we extend the spin distributions at  $z = 0$  to dwarf-galaxy-sized haloes (down to  $10^8 M_\odot$ ) in the same way as the concentration.

First, we determine the minimum number of particles in a halo necessary to reliably determine the spin as done for the concentration. Figure 3.11 shows the normalized difference of average spin between the CG2048 run and the CG512 run as a function of halo mass. We can see that the difference is  $\sim 0.05$  for halo

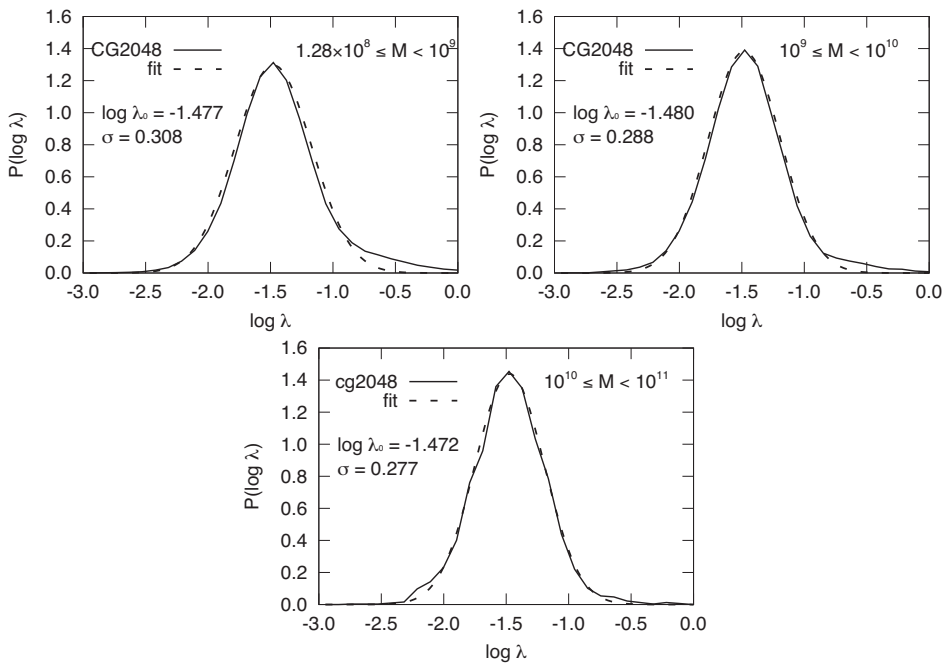


**Figure 3.13:** Probability distribution functions of the spin parameter at  $z = 0$ . These panels show the results of different mass ranges. Dashed curves are the best fits of the log-normal distribution.

mass larger than  $8.0 \times 10^9 M_\odot$ . For halo mass less than  $8.0 \times 10^9 M_\odot$ , the difference is large.

In the CG512 run, a halo of mass  $8.0 \times 10^9 M_\odot$  contains  $\sim 1000$  particles. So we conclude that we need  $\sim 1000$  particles to reliably determine the concentration. For the CG2048 run, the reliability limit is  $1.28 \times 10^8 M_\odot$ .

Figure 3.12 shows the median, and first third quantiles of the spin parameter as a function of the virial mass of the halo. Apparently, we can see the spin parameter is independent of the mass down to  $10^8 M_\odot$  as pointed out for larger haloes in previous works (Macciò et al. 2007; Muñoz-Cuertas et al. 2011). The median value is 0.0336.

Figure 3.13 shows the probability distribution functions of the spin parameter at  $z = 0$  in three different mass ranges. The distributions are well fitted by the log-normal distributions,

$$P(\log \lambda) = \frac{1}{\sqrt{2\pi}\sigma} \exp\left(-\frac{\log^2(\lambda/\lambda_0)}{2\sigma^2}\right). \quad (3.9)$$

We find  $\log \lambda_0 = -1.477$ ,  $\sigma = 0.308$  for haloes with the mass of  $1.28 \times 10^8 M_\odot \leq M < 10^9 M_\odot$ ,  $\log \lambda_0 = -1.480$ ,  $\sigma = 0.288$  for haloes with the mass of  $10^9 M_\odot \leq M < 10^{10} M_\odot$ , and  $\log \lambda_0 = -1.472$ ,  $\sigma = 0.277$  for haloes with the mass of  $10^{10} M_\odot \leq M < 10^{11} M_\odot$ . Thus, we conclude that there is no mass dependence of the spin parameter. Otherwise, it is extremely weak.

We can see that there are small deviations from the log-normal distributions at high spin regions as seen in previous works for larger haloes (Bett et al. 2007; Antonuccio-Delogu et al. 2010). We will discuss the effect of the dynamical state of haloes in Appendix 3.A.

### 3.3.5 Subhalo

The statistics of the subhalo abundance of galaxy-sized haloes have been well studied (e.g., Ishiyama et al. 2009a; Boylan-Kolchin et al. 2010; Busha et al. 2011). The subhalo abundance shows large halo-to-halo variations and depends on the concentration parameter. Halos with larger concentrations have a smaller number of subhaloes. This means that the number of subhaloes should increase as the halo mass increases since the concentration decreases. However, little is known on how the subhalo abundance depends on the halo mass. The reason is that we need a number of well-resolved haloes in a wide mass range to determine the mass dependence and it is computationally expensive to perform simulations for this purpose.

Contini et al. (2012) analysed the fraction of halo mass in subhaloes for group-sized to cluster-sized haloes and showed that the fraction increases with increasing

**Figure 3.14:** Residuals of the subhalo abundance from the largest simulation (CG2048) to lower resolution simulation (CG1024). Here,  $N_{>x}$  is the number of subhaloes with rotation velocity larger than  $x$  of that of the parent halo.

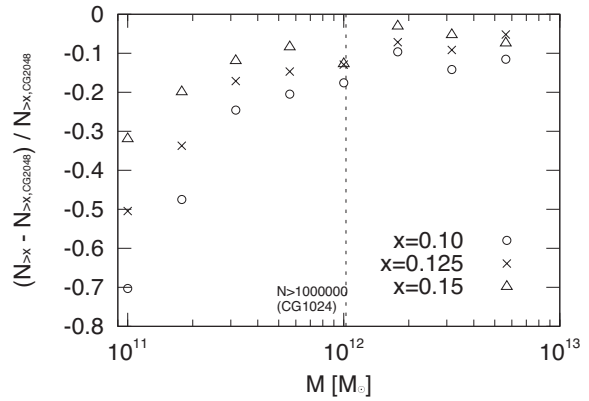
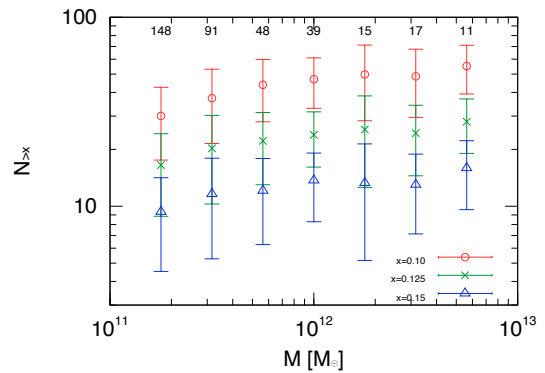


**Figure 3.15:** Number of subhaloes plotted against the halo virial mass  $M$  at  $z = 0$ . Each symbol shows the mean value on each bin. Whiskers are the standard deviation. The number of haloes on each bin is shown above.



mass. For group-sized haloes, it is approximately 5%, and for cluster-sized haloes approximately 10% (similar results are obtained in Gao et al. 2011, for a slightly different mass range). However, the number of particles per halo of their group-sized haloes is  $10^5$ , which is insufficient to robustly estimate the subhalo abundance (see also Ishiyama et al. 2009a). Therefore, it is possible that they have underestimated the subhalo abundance.

Our high-resolution simulations are suitable for the study of the statistics of the subhalo abundance for haloes with smaller mass. Therefore we can address a key question, how the subhalo abundance depends on the halo mass. Hereafter, we define  $N_{>x}$  as the subhalo abundance, which is the number of subhaloes with rotation velocity larger than  $x$  times that of the parent halo. Figure 3.14 shows the normalized difference of average subhalo abundance between the CG2048 run and the CG1024 run as a function of halo mass for  $x = 0.10, 0.125, 0.15$ . We can see that both results are well converged for haloes with more than one million particles for all values of  $x$ . For haloes with less particles, the difference becomes larger as the halo mass decreases. Thus, we can conclude that we need about one million particles to reliably determine the subhalo abundance. For the CG2048 run, the reliability limit is  $1.28 \times 10^{11} M_{\odot}$  for  $x = 0.1$ .

The reliability limit should be smaller for larger subhaloes (larger values of  $x$ ) since they consist of more particles than smaller ones. As seen in Figure 3.14, the residual of the subhalo abundance is systematically smaller for larger subhaloes (larger  $x$ ). However, for simplicity, we use the same reliability limit for all values of  $x$ . Thus, our choice of the reliability limit is quite conservative.

Figure 3.15 shows the mean and the standard deviation of the subhalo abundance as a function of the virial mass of the halo. We can see clearly that the subhalo abundance depends on the halo mass for all values of  $x$ . The average number of subhaloes  $N_{>0.10}, N_{>0.125}, N_{>0.15}$  are 30.1, 16.5, 9.3 for haloes with the mass of  $\sim 2 \times 10^{11} M_{\odot}$  and 47.0, 23.8, 13.7 for haloes with the mass of  $\sim 1 \times 10^{12} M_{\odot}$ . For haloes with the mass of larger than  $\sim 1 \times 10^{12} M_{\odot}$ , we can see that the dependence becomes weaker and gradually approaches to a constant value.

This trend has not been observed in previous works (Gao et al. 2011; Contini et al. 2012), since they analysed haloes with larger mass. However, our result is limited by the box size of the simulation. Since the number of subhaloes with the mass larger than  $1 \times 10^{12} M_{\odot}$  in our simulation is only 82, our haloes within this mass range might be a biased sample. In order to clarify the dependency, larger box simulations are needed.

### 3.4 Discussions and Summary

We present the first scientific results of the CosmoGrid simulation. Because of unprecedentedly high-resolution and powerful statistics, the simulation is suitable to resolve internal properties of haloes with the mass larger than dwarf galaxy and subhaloes whose scales are comparable to ultra-faint dwarf galaxies.

We summarize the main results of this paper as follows.

- The halo mass function is well described by the Sheth and Tormen (1999) fitting function down to  $\sim 10^7 M_\odot$  from  $1.0 \times 10^{13} M_\odot$ . The differences are less than 10% at  $z = 0$  from  $M = 5.0 \times 10^7 M_\odot$  to  $M = 2.0 \times 10^{12} M_\odot$ .
- We analysed the spherically averaged density profiles of the three most massive haloes which contain more than 170 million particles. Their masses are 5.24, 3.58, and  $2.25 \times 10^{13} M_\odot$ . We confirmed that the slopes of density profiles of these haloes become shallower than  $-1$  at the inner most radius. The results are consistent with the recent studies based on high-resolution simulations for galactic haloes.
- We studied internal properties of haloes at  $z = 0$  with the mass more than  $\sim 10^8 M_\odot$ . The concentration parameter measured by the maximum rotational velocity radius is weakly correlated with the halo mass. We found that the dependence of the concentration parameter with halo mass cannot be expressed by a single power law, but levels off at small mass. The slope of the mass--concentration relation is around  $-0.07$  for haloes with the mass  $10^{10} M_\odot$ , and  $-0.06$  for haloes with the mass  $10^9 M_\odot$ . The shallowing slope naturally emerges from the nature of the power spectrum of initial density fluctuations. A simple model based on the Press-Schechter theory gives reasonable agreement with the simulation result. The spin parameter does not show a correlation with the halo mass. The probability distribution functions of concentration and spin are well fitted by the log-normal distribution for haloes with the mass larger than  $\sim 10^8 M_\odot$ .
- The subhalo abundance depends on the halo mass. Galaxy-sized haloes have 50% more subhaloes than  $\sim 10^{11} M_\odot$  haloes have. We find a new result that the dependence becomes weaker for more massive haloes.

### Acknowledgements

*We thank the anonymous referee for his/her valuable comments. Numerical computations were partially carried out on Cray XT4 at Center for Computational Astrophysics, CfCA, of National Astronomical Ob-*

servatory of Japan, the K computer at the RIKEN Advanced Institute for Computational Science (Proposal number hp120286), Huygens at the Dutch National High Performance Computing and e-Science Support Center, SARA (Netherlands), HECToR at the Edinburgh Parallel Computing Center (United Kingdom), and Louhi at IT Center for Science in Espoo (Finland).

T.I. is financially supported by Research Fellowship of the Japan Society for the Promotion of Science (JSPS) for Young Scientists. This research is partially supported by the Special Coordination Fund for Promoting Science and Technology (GRAPE-DR project), Ministry of Education, Culture, Sports, Science and Technology, Japan.

We also thank the network facilities of SURFnet, DEISA, IEEAF, WIDE, Northwest Gigapop and the Global Lambda Integrated Facility (GLIF), NSF funded TransLight project, National LambdaRail, StarLight, NetherLight, T-LEX, Pacific and Atlantic Wave.

This research is supported by the Netherlands organization for Scientific research (NWO) grants #639.073.803, #643.200.503 and #643.000.803, the Stichting Nationale Computerfaciliteiten (project #SH-095-08), NAOJ, SURFnet (GigaPort project), the International Information Science Foundation (IISF), the Netherlands Advanced School for Astronomy (NOVA), the Leids Kerkhoven-Bosscha fonds (LKBF). We thank the DEISA Consortium (EU FP6 project RI-031513 and FP7 project RI-222919) for support within the DEISA Extreme Computing Initiative (GBBP project). This work has been funded by MEXT/HPCI STRATEGIC PROGRAM and MEXT/JSPS KAKENHI Grand Number 24740115.

### 3.A The Effect of Dynamical State of Halos

There are large variations in the dynamical state of haloes. Halos which formed in an early epoch tend to be dynamically relaxed, whereas haloes which experienced a recent major merger tend to be dynamically unrelaxed. The relaxation state of haloes might have some effect on properties of haloes such as the concentration and the spin. Here, we analyse these properties for only dynamically relaxed sample of haloes and discuss the effect of the relaxation state.

Power et al. (2012) argued that the centre-of-mass offset is a robust estimator of the relaxation state of haloes. The centre-of-mass offset is defined as

$$\Delta r = \frac{|\mathbf{r}_{\text{cen}} - \mathbf{r}_{\text{cm}}|}{R_{\text{vir}}}, \quad (3.10)$$

where  $\mathbf{r}_{\text{cen}}$ ,  $\mathbf{r}_{\text{cm}}$ , and  $R_{\text{vir}}$  are the centre of density, mass, and the virial radius of a halo. They found that  $\Delta r \leq 0.04$  is a sufficient condition to pick up dynamically relaxed haloes at  $z = 0$ . We use this condition to construct the relaxed sample of haloes from our all halo samples.

Figure 3.16 shows the average centre-of-mass offset and the fraction of relaxed haloes as a function of the halo virial mass. The offset increases with increasing the halo mass. This trend is in good agreement with the results of Power et al. (2012).

It is simply because lower mass haloes tend to form earlier than higher mass haloes from the nature of the hierarchical structure formation. As a result, the fraction of relaxed haloes becomes large for lower mass haloes. We can see the offset increases with decreasing the halo mass from  $\sim 5 \times 10^8 M_\odot$ . This may be caused by the resolution effect.

One may wonder whether the dependence of concentrations to the halo mass is caused by unrelaxed haloes or not. Figure 3.17 shows the median concentration and spin for all and the relaxed sample of haloes as a function of the virial mass of the halo. The relaxation state has little impact on the concentration for haloes smaller than  $10^{11} M_\odot$ . This can be interpreted as the fact that the fraction of relaxed haloes is large for lower mass haloes as we can see in Figure 3.16.

The spin parameters of relaxed haloes are systematically smaller than those of all haloes by  $\sim 8 - 10\%$  for all mass ranges. This result is consistent with early studies (Macciò et al. 2007, 2008). This is because unrelaxed haloes tend to experience a recent major merger, giving them higher spin values. Figure 3.18 shows the probability distribution functions of the spin parameter at  $z = 0$  in three different mass ranges. We can see clearly that the number of haloes with high spin values in the relaxed sample of haloes is smaller than that in all sample of haloes for all mass ranges. We find  $\log \lambda_0 = -1.514, \sigma = 0.286$  for haloes with the mass of  $1.28 \times 10^8 M_\odot \leq M < 10^9 M_\odot$ ,  $\log \lambda_0 = -1.520, \sigma = 0.265$  for haloes with the mass of  $10^9 M_\odot \leq M < 10^{10} M_\odot$ , and  $\log \lambda_0 = -1.519, \sigma = 0.265$  for haloes with the mass of  $10^{10} M_\odot \leq M < 10^{11} M_\odot$ . The standard deviations are also systematically smaller for relaxed haloes by  $\sim 4 - 8\%$ .

Small deviations from the log-normal distributions at high spin regions for all haloes are also seen for relaxed haloes. The deviations become weaker since unrelaxed haloes with higher spin are removed.

It is interesting that the spin is relatively influenced by the relaxation state more than the concentration. This might be because haloes grow in a self-similar way (e.g., Fukushige and Makino 2001). The self-similar growth means that the inner region of a halo forms earlier than the outer region. Here, the spin is calculated using all particles. The concentration is estimated using particles within the radius of the maximum rotational velocity, which should be more dynamically relaxed than particles in outer region. Therefore, it is natural that the effect of the relaxation state on the concentration and spin shows such difference.

In summary, we find that the relaxation state makes small difference on the concentration and spin distributions.

- The impact of the relaxation state on the concentration is negligible for haloes smaller than  $10^{11} M_\odot$ .



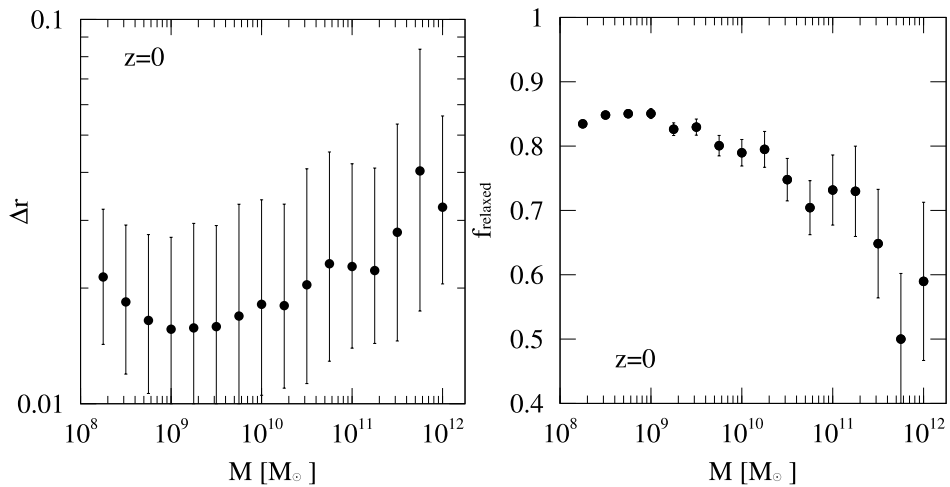


**Figure 3.16:** Left: the centre-of-mass offset of all haloes plotted against the halo virial mass  $M$  at  $z = 0$ . The median value of each bin is shown by circles. Whiskers are the first and third quantiles. Right: the fraction of relaxed haloes. Error bars are Poisson errors.

- The spin parameters of relaxed haloes are systematically smaller than those of all haloes by  $\sim 8 - 10\%$  for all mass ranges. The spin distributions of relaxed haloes deviate from the log-normal fitting less than those of all haloes.

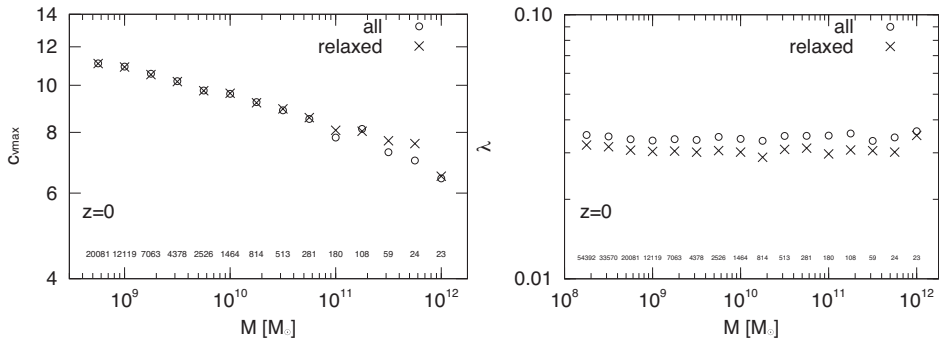


**Figure 3.17:** Concentration (left) and spin (right) plotted against the halo virial mass  $M$  at  $z = 0$ . The median values of all haloes are shown by circles. Crosses are for the values of only relaxed haloes. The number of relaxed haloes on each bin is shown below.

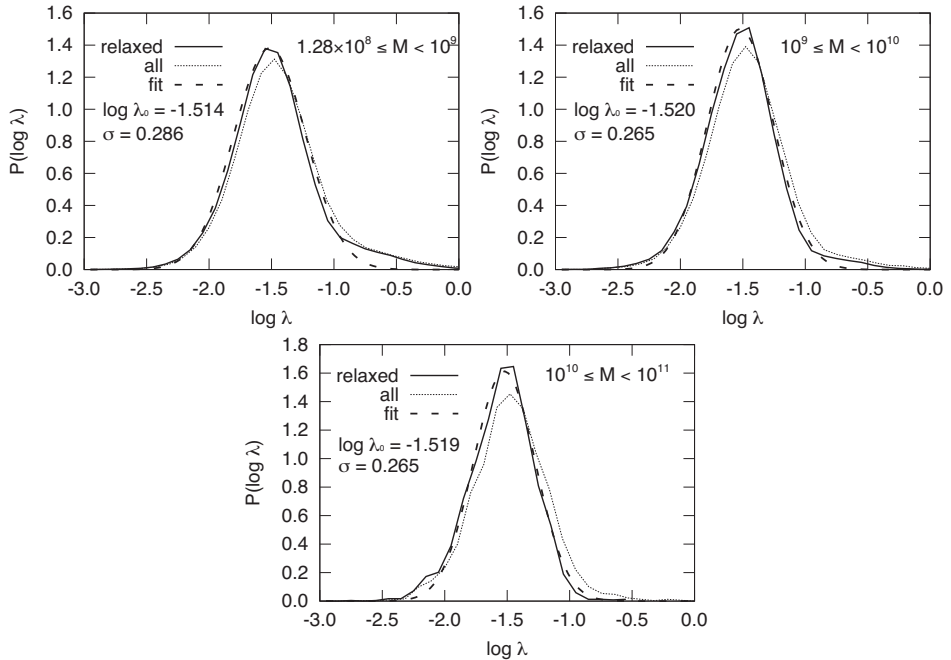


**Figure 3.18:** Probability distribution functions of the spin parameter at  $z = 0$  for relaxed haloes (solid) and all haloes (dotted). Dashed curves are the best fits of the log-normal distribution for relaxed haloes.

# 4 | Assembly of filamentary void galaxy configurations

*Based on:*

*Steven Rieder, Rien van de Weygaert, Marius Cautun, Burcu Beygu and Simon Portegies Zwart*

*Assembly of filamentary void galaxy configurations*

*Published in MNRAS*

We study the formation and evolution of filamentary configurations of dark matter haloes in voids. Our investigation uses the high-resolution  $\Lambda$ CDM simulation CosmoGrid to look for void systems resembling the VGS\_31 elongated system of three interacting galaxies that was recently discovered by the Void Galaxy Survey (VGS) inside a large void in the SDSS galaxy redshift survey. HI data revealed these galaxies to be embedded in a common elongated envelope, possibly embedded in intravoid filament.

In the CosmoGrid simulation we look for systems similar to VGS\_31 in mass, size and environment. We find a total of eight such systems. For these systems, we study the distribution of neighbour haloes, the assembly and evolution of the main haloes and the dynamical evolution of the haloes, as well as the evolution of the large-scale structure in which the systems are embedded. The spatial distribution of the haloes follows that of the dark matter environment.

We find that VGS\_31-like systems have a large variation in formation time, having formed between 10 Gyr ago and the present epoch. However, the environments in which the systems are embedded evolved resemble each other substantially. Each of the VGS\_31-like systems is embedded in an intra-void wall, that no later than  $z = 0.5$  became the only prominent feature in its environment. While part of the void walls retain a rather featureless character, we find that around half of them are marked by a pronounced and rapidly evolving substructure. Five haloes find themselves in a tenuous filament of a few  $h^{-1}$ Mpc long inside the intra-void wall.

Finally, we compare the results to observed data from VGS\_31. Our study implies that the VGS\_31 galaxies formed in the same (proto)filament, and did not meet just recently. The diversity amongst the simulated halo systems indicates that VGS\_31 may not be typical for groups of galaxies in voids.

## 4.1 Introduction

Voids form the most prominent aspect of the Megaparsec distribution of galaxies and matter (Chincarini and Rood 1975; Gregory and Thompson 1978; Zeldovich et al. 1982; Kirshner et al. 1981; Kirshner et al. 1987; de Lapparent et al. 1986). They are enormous regions with sizes in the range of  $20 - 50 h^{-1}\text{Mpc}$  that are practically devoid of any galaxy, usually roundish in shape and occupying the major share of volume in the Universe (see van de Weygaert and Platen 2011, for a recent review). The voids are surrounded by sheet-like walls, elongated filaments and dense compact clusters together with which they define the *Cosmic Web* (Bond et al. 1996), i.e. the salient web-like pattern given by the distribution of galaxies and matter in the Universe. Theoretical models of void formation and evolution suggest that voids act as the key organizing element for arranging matter concentrations into an all-pervasive cosmic network (Icke 1984; Regos and Geller 1991; van de Weygaert and van Kampen 1993; Sahni et al. 1994; Sheth and van de Weygaert 2004; Einasto et al. 2011; Aragon-Calvo and Szalay 2013).

Voids mark the transition scale at which density perturbations have decoupled from the Hubble flow and contracted into recognizable structural features. At any cosmic epoch, the voids that dominate the spatial matter distribution are a manifestation of the cosmic structure formation process reaching a non-linear stage of evolution. Voids emerge out of the density troughs in the primordial Gaussian field of density fluctuations. Idealized models of isolated spherically symmetric or ellipsoidal voids (Hoffman and Shaham 1982; Icke 1984; Bertschinger 1985; Blumenthal et al. 1992; Sheth and van de Weygaert 2004) illustrate how the weaker gravity in underdense regions results in an effective repulsive peculiar gravitational influence. As a result, matter is evacuating from their interior of initially underdense regions, while they expand faster than the Hubble flow of the background Universe. As the voids expand, matter gets squeezed in between them, and sheets and filaments form the void boundaries.

While idealized spherical or ellipsoidal models provide important insights into the basic dynamics and evolution of voids, computer simulations of the gravitational evolution of voids in realistic cosmological environments show a considerably more complex situation. Sheth and van de Weygaert (2004) (also see Dubinski et al. 1993; Sahni et al. 1994; Goldberg and Vogeley 2004; Furlanetto and Piran 2006; Aragon-Calvo and Szalay 2013) treated the emergence and evolution of voids within the context of *hierarchical* gravitational scenarios. It leads to a considerably modified view of the evolution of voids, in which the interaction with their surroundings forms a dominant influence. The void population in the Universe evolves hierarchically, dictated by two complementary processes. Emerging

from a primordial Gaussian field, voids are often embedded within a larger underdense region. The smaller voids, matured at an early epoch, tend to merge with one another to form a larger void, in a process leading to ever larger voids. Some, usually smaller, voids find themselves in collapsing overdense regions and will get squeezed and demolished as they collapse with their surroundings.

A key aspect of the *hierarchical* evolution of voids is the substructure within their interior. N-body simulations show that while void substructure fades, it does not disappear (van de Weygaert and van Kampen 1993). Voids do retain a rich yet increasingly diluted and diminished infrastructure, as remnants of the earlier phases of the *void hierarchy* in which the substructure stood out more prominent. In fact, the slowing of growth of substructure in a void is quite similar to structure evolution in a low  $\Omega$  Universe (Goldberg and Vogeley 2004). Structure within voids assumes a range of forms, and includes filamentary and sheet-like features as well as a population of low mass dark matter haloes and galaxies (see e.g. van de Weygaert and van Kampen 1993; Gottlöber et al. 2003). Although challenging, void substructure has also been found in the observational reality. For example, the SDSS galaxy survey has uncovered a substantial level of substructure within the Boötes void (Platen 2009), confirming tentative indications for a filamentary feature by Szomoru et al. (1996).

The most interesting denizens of voids are the rare galaxies that populate these underdense region, the *void galaxies* (Szomoru et al. 1996; Kuhn et al. 1997; Popescu et al. 1997; Karachentseva et al. 1999; Grogin and Geller 1999, 2000; Hoyle and Vogeley 2002, 2004; Rojas et al. 2004, 2005; Tikhonov and Karachentsev 2006; Patiri et al. 2006a,b; Ceccarelli et al. 2006; Park et al. 2007; von Benda-Beckmann and Müller 2008; Wegner and Grogin 2008; Stanonik et al. 2009; Kreckel et al. 2011; Pustilnik and Tepliakova 2011; Kreckel et al. 2012; Hoyle et al. 2012). The relation between void galaxies and their surroundings forms an important aspect of the recent interest in environmental influences on galaxy formation. Void galaxies appear to have significantly different properties than average field galaxies. They appear to reside in a more youthful state of star formation and possess larger and less distorted gas reservoirs. Analysis of void galaxies in the SDSS and Two-degree-Field Galaxy Redshift Survey (2dFGRS) indicate that void galaxies are bluer and have higher specific star formation rates than galaxies in denser environments.

#### 4.1.1 The Void Galaxy Survey

A major systematic study of void galaxies is the Void Galaxy Survey (VGS), a multi-wavelength program to study  $\sim 60$  void galaxies selected from the SDSS DR7 redshift survey (Stanonik et al. 2009; Kreckel et al. 2011, 2012). These galaxies were selected from the deepest inner regions of voids, with no a priori bias on

the basis of the intrinsic properties of the void galaxies. The voids were identified using of a unique geometric technique, involving the Watershed Void Finder (Platen et al. 2007) applied to a Delaunay Tessellation Field Estimator (DTFE) density field reconstruction. An important part of the program concerns the gas content of the void galaxies, and thus far the HI structure of 55 VGS galaxies has been mapped. In addition, it also involves deep B and R imaging of all galaxies,  $H\alpha$  and GALEX UV data for assessing the star formation properties of the void galaxies.

Perhaps the most interesting configuration found by the Void Galaxy Survey is VGS\_31 (Beygu et al. 2013). Embedded in an elongated common HI cloud, at least three galaxies find themselves in a filamentary arrangement with a size of a few hundred kpc. One of these objects is a Markarian galaxy, showing evidence for recent accretion of minor galaxies. Along with the central galaxy, which shows strong signs of recent interaction, there is also a starburst galaxy.

We suspect, from assessing the structure of the void, that the gaseous VGS\_31 filament is affiliated to a larger filamentary configuration running across the void and visible at one of the boundaries of the void. This elicits the impression that VGS\_31 represents a rare specimen of a high density spot in a tenuous dark matter void filament. Given the slower rate of evolution in voids, it may mean that we find ourselves in the unique situation of witnessing the recent assembly of a filamentary galaxy group, a characteristic stage in the galaxy and structure formation process.

#### 4.1.2 Outline

In this study we concentrate on implications of the unique VGS\_31 configuration for our understanding of the dynamical evolution of void filaments and their galaxy population. We are interested in the assembly of the filament configuration itself, as well as that of the halo population in its realm. In fact, we use the specific characteristics of the VGS\_31 galaxies, roughly translated from galaxy to dark matter halo, to search for similar dark halo configurations in the CosmoGrid simulation (Portegies Zwart et al. 2010a; Ishiyama et al. 2013, see Figure 4.1).

Subsequently, we study in detail the formation and evolution of the entire environment of these haloes. In this way, we address a range of questions. What has been the assembly and merging history of the configuration? Did the VGS\_31 galaxies recently meet up and assemble into a filament, or have they always been together? Is the filament an old feature, or did it emerge only recently? May we suspect the presence of more light mass galaxies in the immediate surrounding of VGS\_31, or should we not expect more than three such galaxies in the desolate void region?

Our study uses a pure dark matter N-body simulation. While a full under-

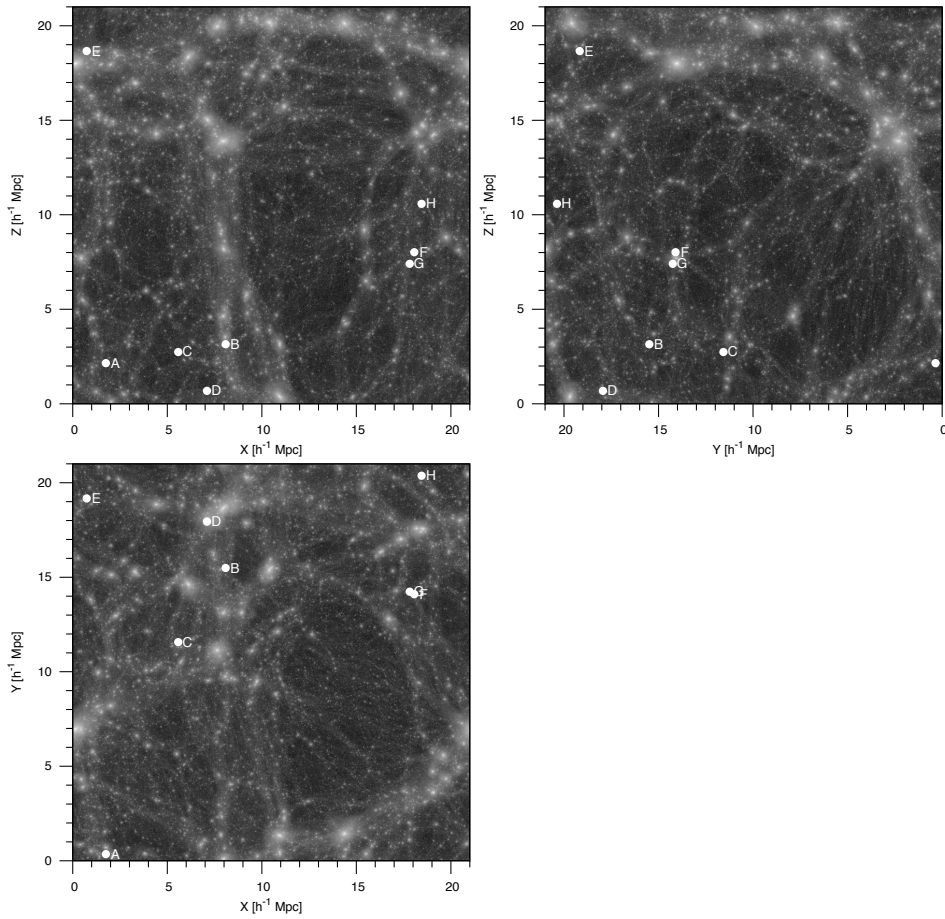


**Figure 4.1:** A snapshot of the full CosmoGrid volume seen from different sides, with dots indicating the locations of the void halo systems. The images display the full  $(21 h^{-1}\text{Mpc})^3$  volume.

standing of the unique properties of VGS\_31 evidently should involve the complexities of its gas dynamical history, along with that of the stellar populations, here we specifically concentrate on the overall gravitational aspects of its dynamical evolution. The reason for this is that the overall evolution of the filamentary structure will be dictated by the gravitational influence of the mass concentrations in and around the void. For a proper understanding of the context in which VGS\_31 may have formed, it is therefore better to concentrate solely on the gravitational evolution.

The outline of this paper is as follows. In section 4.2.1, we discuss the simulation used in this article, along with the criteria which we used for the selecting VGS-31 resembling halo configurations. The properties and evolution of the eight selected halo groups are presented and discussed in section 4.3. Section 4.4 continues the discussion by assessing the large scale environment in which the VGS\_31 resembling configurations are situated, with special attention to the walls and filaments in which they reside. We also investigate the evolution of the surrounding filamentary pattern as the haloes emerge and evolve. Finally, in section 4.5 we evaluate and discuss the most likely scenario for the formation of void systems like VGS\_31. In section 4.6 we summarize and discuss our findings.

## 4.2 Simulations

### 4.2.1 Setup

In order to evaluate possible formation scenarios for systems like VGS\_31, we investigate the formation of systems with similar properties in a cosmological simulation. For this purpose, we use the CosmoGrid  $\Lambda$ CDM simulation (Ishiyama et al. 2013). The CosmoGrid simulation contains  $2048^3$  particles within a volume of  $21 h^{-1}\text{Mpc}^3$ , and has high enough mass resolution ( $8.9 \times 10^4 h^{-1}M_{\odot}$  per particle) to study both dark matter haloes and the dark environment in which the haloes form. The CosmoGrid simulation used a gravitational softening length  $\epsilon$  of 175 parsec, and the following cosmological parameters:  $\Omega_m = 0.3$ ,  $\Omega_{\Lambda} = 0.7$ ,  $h = 0.7$ ,  $\sigma_8 = 0.8$  and  $n = 1.0$ .

The first reduction step concerns the detection and identification of haloes and their properties in the CosmoGrid simulation. For this, we use the Rockstar halo finder. Rockstar uses a six-dimensional friends-of-friends algorithm to detect haloes in phase-space. It excels in tracking substructure, even in ongoing major mergers and in halo centres (e.g. Knebe et al. 2011; Onions et al. 2012).

Since we are interested in the formation history of the haloes, we analyse multiple snapshots. Merger trees are constructed to identify haloes across the snapshots,



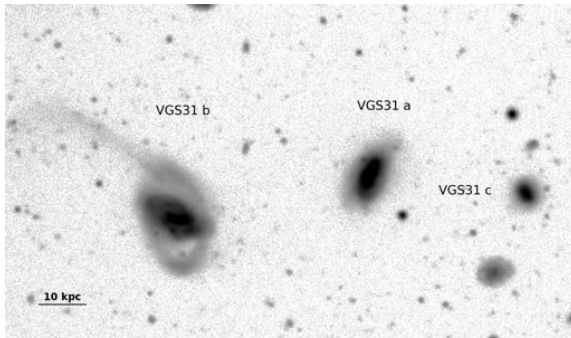


**Figure 4.2:** B band image of the VGS\_31 system: VGS\_31\_b (left), VGS\_31\_a (centre) and VGS\_31\_c (right). The physical scale of the system may be inferred from the bar in the lower left-hand corner.

for which we use the gravitationally consistent merger tree code from Behroozi et al. (2013b). For this we use 193 CosmoGrid snapshots, equally spaced in time at 70 Myr intervals.

Finally, to compare the CosmoGrid haloes to the galaxies observed in void regions, we need to identify the regions in CosmoGrid that can be classified as voids. In doing so we compute the density field using the Delaunay Tessellation Field Estimator (DTFE, Schaap and van de Weygaert 2000; van de Weygaert and Schaap 2009; Cautun and van de Weygaert 2011). We express the resulting density in units of the mean background density  $\langle \rho \rangle$  as  $1 + \delta = \rho / \langle \rho \rangle$ . The resulting density field is smoothed with  $1 h^{-1} \text{Mpc}$  Gaussian filter to obtain a large scale density field. We identify voids as the regions with a  $1 h^{-1} \text{Mpc}$  smoothed density contrast of  $\delta < -0.5$ .

#### 4.2.2 Selection of the simulated haloes

The VGS\_31 system consists of three galaxies with spectrophotometric redshift  $z = 0.0209$ . The principal galaxies VGS\_31a and VGS\_31b, and the 2 magnitudes fainter galaxy VGS\_31c, are stretched along an elongated configuration of  $\sim 120 \text{ kpc}$  in size (see Figure 4.2). The properties of the VGS\_31 galaxies are listed in Table 4.1. The three galaxies are connected by an HI bridge that forms a filamentary structure in the void (Beygu et al. 2013). Both VGS\_31a and VGS\_31b show strong signs of tidal interactions. VGS\_31b has a tidal tail and a ring like structure wrapped around the disk. This structure can be the result of mutual gravitational interaction with VGS\_31a or may be caused by a fourth object that fell in VGS\_31b.

We use the CosmoGrid simulation to select halo configurations that resemble VGS\_31. In doing so we define a set of five criteria that the halo configuration should fulfil at  $z = 0$ . The first two criteria involve the properties of individual haloes:

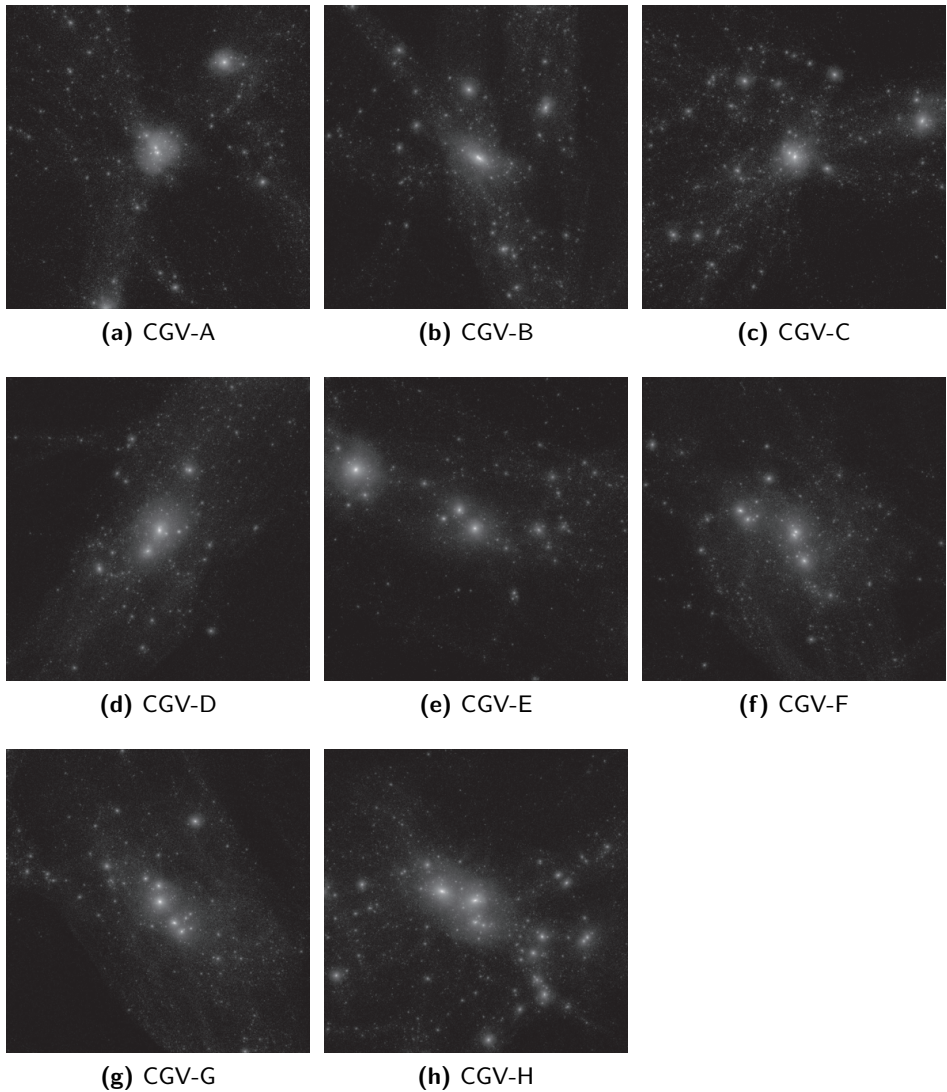


**Figure 4.3:** CosmoGrid Void systems A - H. The frames show the dark matter density distribution in regions of  $1 h^{-1} \text{Mpc}^3$  around the principal haloes of each CGV system.

**Table 4.1:** Some of the properties of VGS\_31 member galaxies.

Name	$M_*$ $10^8 M_\odot$	$M_{HI}$ $10^8 M_\odot$	$M_{\text{dyn}}$ $10^{10} M_\odot$	$\delta$
(1)	(2)	(3)	(4)	(5)
VGS_31a	35.1	$19.89 \pm 2.9$	$< 2.31$	-0.64
VGS_31b	105.31	$14.63 \pm 1.97$		
VGS_31c	2.92	$1.66 \pm 0.95$		

Object name (1). Stellar mass (2). HI mass (3). Dynamic mass (4). Density contrast after applying a  $1 h^{-1}\text{Mpc}$  Gaussian filter (5).

- We select only haloes with mass  $M_{\text{vir}}$  in the range  $2 \times 10^{10} h^{-1}M_\odot$  to  $10^{11} h^{-1}M_\odot$ . This represents a reasonable estimate for the mass of the most massive dark matter halo in the VGS\_31 system.
- Out of the haloes found above, we keep only the ones which reside in void-like region, where the  $1 h^{-1}\text{Mpc}$  smoothed density fulfils  $\delta \leq -0.50$ .

There are 84 haloes in the CosmoGrid simulation that fulfil the above two criteria. Subsequently, we further restrict the selection to those haloes that are located within a system that is similar to VGS\_31. To that end, we look at the properties of all haloes and subhaloes within a distance of  $200 h^{-1}\text{kpc}$  from the main haloes selected above. A system is selected when the primary halo has, within  $200 h^{-1}\text{kpc}$ :

- a secondary (sub)halo with  $M_{\text{vir}} > 5 \times 10^9 h^{-1}M_\odot$ ,
- a tertiary (sub)halo with  $M_{\text{vir}} > 10^9 h^{-1}M_\odot$ ,
- no more than 5 neighbour (sub)haloes with  $M_{\text{vir}} > 5 \times 10^9 h^{-1}M_\odot$ .

Following the application of these criteria, we find a total of 8 VGS\_31-like systems in the CosmoGrid simulation. We call these systems the CosmoGrid Void systems. The individual haloes in the eight void halo systems are indicated by means of a letter, eg. CGV-A\_a and CGV-A\_b. In the subsequent sections we investigate the halo evolution, merger history and large scale environment of the eight void halo configurations.

### 4.2.3 Analysis of the environment

We investigate the formation and evolution of the eight CGVs within the context of the large scale environment in which they reside. In doing so we use the NEXUS+ method (Cautun et al. 2013) to identify the morphology of large scale

**Table 4.2:** Properties of the eight CosmoGrid Void systems found to resemble VGS\_31.

Name	$M_{\text{vir}}$ $10^{10} h^{-1} M_{\odot}$	$R_{\text{vir}}$ $h^{-1} \text{kpc}$	$V_{\text{max}}$ km/s	$r$ $h^{-1} \text{kpc}$	$\theta$ $^{\circ}$	$\phi$ $^{\circ}$	$\delta$	last MM Gyr	$\angle_{\text{wall}}$ $^{\circ}$	$\angle_{\text{fil}}$ $^{\circ}$
(1)	(2)	(3)	(4)	(5)	(6)	(7)	(8)	(9)	(10)	(11)
CGV-A_a	3.15	64.5	48.7				-0.68	-	51.45	-
CGV-A_b	0.59	36.8	34.6	17	94.0	111.2	-0.68	-	12.48	-
CGV-A_c	0.16	23.9	22.1	76	61.9	122.6	-0.68	-	59.24	-
CGV-B_a	3.95	69.5	63.5				-0.51	5.24	20.80	80.71
CGV-B_b	0.87	42.0	47.6	23	20.1	141.5	-0.51	-	46.76	62.02
CGV-B_c	0.16	23.7	29.8	20	26.9	135.8	-0.51	-	17.04	86.71
CGV-C_a	2.99	63.3	54.8				-0.51	1.19	11.94	-
CGV-C_b	0.54	35.8	34.0	37	36.1	142.7	-0.51	-	34.79	-
CGV-C_c	0.14	23.0	24.2	64	2.9	81.4	-0.51	-	5.49	-
CGV-C_d	0.13	22.3	22.6	113	93.4	-19.5	-0.51	-	82.73	-
CGV-D_a	4.60	73.1	61.3				-0.63	10.9	23.18	20.41
CGV-D_b	0.93	42.9	38.9	86	114.0	-119.2	-0.63	-	2.36	55.11
CGV-D_c	0.16	23.6	30.7	71	65.9	-4.1	-0.63	-	40.89	62.16
CGV-D_d	0.13	22.3	24.1	32	52.7	-25.2	-0.63	-	18.54	86.89
CGV-E_a	1.99	55.3	54.4				-0.57	2.44	8.54	30.67
CGV-E_b	1.01	44.1	44.7	82	104.9	130.1	-0.57	-	68.28	85.00
CGV-E_c	0.23	26.8	33.5	120	115.7	162.7	-0.57	-	72.48	81.23
CGV-F_a	2.27	57.8	55.0				-0.62	-	49.25	73.83
CGV-F_b	0.74	39.8	40.1	14	124.3	-119.7	-0.62	-	77.65	89.75
CGV-F_c	0.11	21.2	28.9	6	169.6	-101.4	-0.62	-	63.99	82.47
CGV-G_a	2.14	56.7	57.4				-0.61	5.80	4.26	12.07
CGV-G_b	0.93	42.9	47.8	139	37.2	-55.6	-0.61	-	20.95	34.20
CGV-G_c	0.38	31.8	34.4	74	45.3	94.0	-0.61	-	18.27	15.73
CGV-H_a	4.63	73.3	66.0				-0.50	8.45	4.01	-
CGV-H_b	4.69	73.6	68.7	199	145.5	164.4	-0.50	-	17.65	-
CGV-H_c	0.69	38.8	38.0	153	151.8	-89.4	-0.50	-	8.84	-
CGV-H_d	0.28	28.6	28.4	92	111.7	-71.6	-0.50	-	43.94	-
CGV-H_e	0.10	20.6	27.9	33	147.3	67.0	-0.50	-	67.46	-
CGV-H_f	0.10	20.5	22.7	86	142.1	-76.8	-0.50	-	54.10	-

Object name (1). Virial mass (2). Virial radius (3). Maximum rotational velocity (4). Position relative to most massive system (5,6,7). Density contrast at halo position (smoothed with  $1 h^{-1} \text{Mpc}$  Gaussian filter) (8). Time at which the last major merger took place (9). Angle between the angular momentum axis of the halo and the normal of the wall (10). Angle between the angular momentum axis of the halo and the filament. (11)

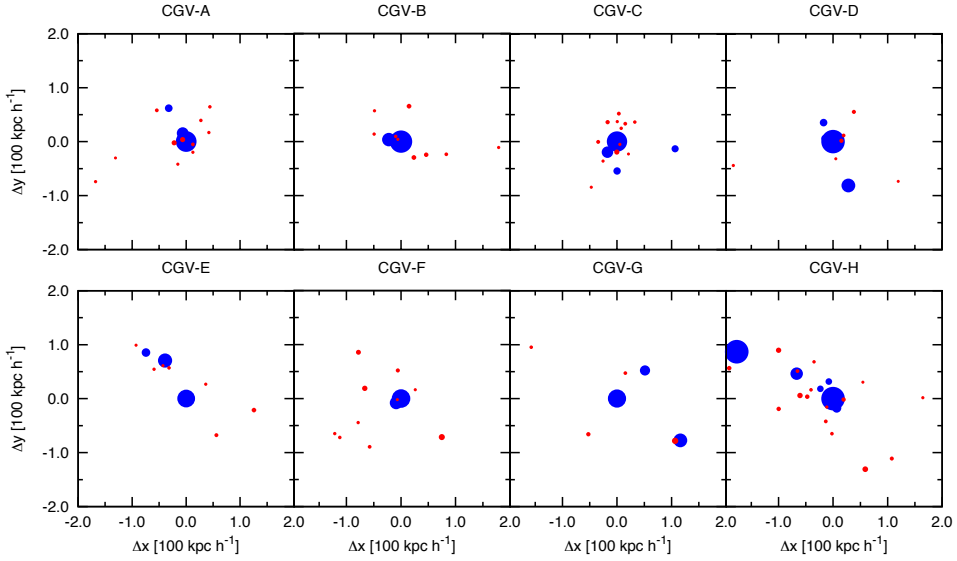


**Figure 4.4:** The spatial distribution of the haloes and subhaloes in the eight CGVs. The blue points show objects more massive than  $10^9 h^{-1}M_{\odot}$ , with point sizes proportional to halo mass. Red points show haloes and subhaloes in the mass range  $(0.1 - 1) \times 10^9 h^{-1}M_{\odot}$ . The plane of the projection is along the large scale wall in which these systems are embedded.

structure around the selected haloes. At each location within the simulation box, it determines whether it belongs to a void or field region, a wall, a filament or a dense cluster node.

The NEXUS+ algorithm is a multiscale formalism that assigns the local morphology on the basis of a scale-space analysis. It is an elaboration and extension of the MMF algorithm introduced by Aragón-Calvo et al. (2007). It translates a given density field into a scale-space representation by smoothing the field on a range of scales. The morphology signature at each of the scales is inferred from the eigenvalues of the Hessian of the density field. The final morphology is determined by selecting the scale which yields the maximum signature value. To discard spurious detections, we use a set of physical criteria to set thresholds for significant morphology signatures.

For a detailed description of the NEXUS+ algorithm, along with a comparison with other Cosmic Web detection algorithms, we refer to Cautun et al. (2013). The method involves the following sequel of key steps:

1. Application of the Log-Gaussian filter of width  $R_n$  to the density field.
2. Calculation of the Hessian matrix eigenvalues for the filtered density field.

3. Assigning to each point a cluster, filament and wall signature on the basis of the three Hessian eigenvalues computed in the previous step.
4. Repetition of steps (i) to (iii) over a range of smoothing scales ( $R_0, R_1, \dots, R_N$ ). For this analysis we filter from  $R_0 = 0.1 h^{-1}\text{Mpc}$  to  $4 h^{-1}\text{Mpc}$ , in steps  $R_n = R_0 2^{n/2}$ .
5. Combination of the morphology signatures at each scale to determine the final scale independent cluster, filament and wall signature.
6. Physical criteria are used to set detection thresholds for significant values of the morphology signatures.

Two important characteristics of NEXUS+ makes it the ideal tool for studying filamentary and wall-like structures in lower density regions. First of all, NEXUS+ is a scale independent method which means that it has the same detection sensitivity for both large and thin filaments and walls. And secondly, Cautun et al. (2013) showed that the method picks up even the more tenuous structures that permeate the voids. Usually these structures have smaller densities and are less pronounced than the more massive filaments and walls, but locally they still have a high contrast with respect to the background and serve as pathways for emptying the voids. Both of these two strengths are crucial for this work since the CGV haloes populate void-like regions with very thin and tenuous filaments and walls.

### 4.3 Evolution of void haloes

In the CosmoGrid simulation we find a total of eight systems (see Figure 4.3) adhering to the search parameters specified in section 4.2.2. We label these CGVs A to H. These systems contains from 3 up to 6 haloes with masses larger than  $10^9 M_\odot$ . They are labelled by an underscore letter, eg. CGV-H\_a or CGV-H\_f. In Figure 4.1, we show the locations of these systems in three mutually perpendicular projections of the  $21 h^{-1}\text{Mpc}$  CosmoGrid box. Figure 4.3 further zooms in on the structure of these systems by showing the density distribution in boxes of  $1 h^{-1}\text{Mpc}$  surrounding the eight configurations.

At  $z=0$ , the CGV haloes have a similar appearance. Within a radius of  $500 h^{-1}\text{kpc}$ , the primary halo of most of the systems is the largest object. The exceptions are the CGV-E and CGV-H systems, which have a larger neighbouring halo. The general properties of the CGVs are listed in Table 4.2.

Figure 4.4 provides an impression of the spatial distribution of the haloes in these eight CVG systems. The principal haloes, those with a mass in excess of  $10^9 M_\odot$ , are represented by a blue dot whose size is proportional to its mass. They

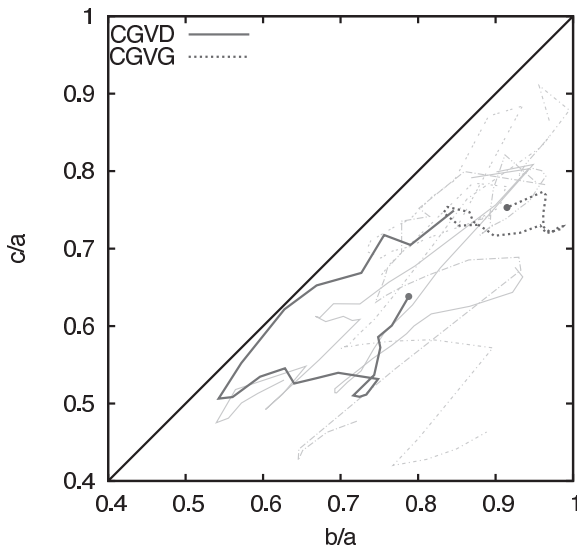


**Figure 4.5:** Shape of the primary CGV haloes, CGV-A\_a to CGV-G\_a. Each track represents the change in the shape of the halo with distance from the halo centre, out to the virial radius (indicated with a dot). We distinguish three interesting regions in the plot: top right ( $a \approx b \approx c$ , i.e.  $c/a = b/a = 1$ ) indicates a spherical halo, bottom left ( $a > b \approx c$ , i.e.  $c/a \approx b/a$ ) indicates a stretched halo (cigar shaped), bottom right ( $a \approx b \gg c$ , i.e.  $c/a \ll b/a = 1$ ) indicates a flattened halo. We emphasize the tracks for CGV-D\_a (solid) and CGV-G\_a (dashed).

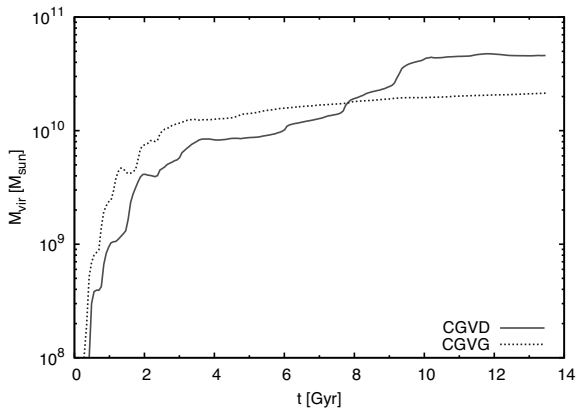


**Figure 4.6:** Mass accretion history for two selected haloes, CGV-D\_a (solid) and CGV-G\_a (dashed). The plot gives the mass contained within each halo as a function of time. CGV-D\_a is marked by three sudden major mass accretions after  $t = 4$  Gyr, while CGV-G\_a leads a quiescent life after it experience an early major merger at  $t = 2.5$  Gyr.

are the haloes listed in Table 4.2. In addition, we plot the location of surrounding small haloes with a mass in the range of  $10^8 < M < 10^9 M_\odot$ . While there are substantial differences between the small-scale details of the mass distribution, we can recognize the global aspect of a filamentary arrangement of a few dominant haloes that characterizes VGS\_31. This is particularly clear for the systems CGV-D, CGV-E, CGV-G and CGV-H.

### 4.3.1 Halo Structure

To investigate the shape characteristics of the principal haloes, we evaluate the shape of their mass distribution as a function of radius. To this end, we measure the

principal axis ratios of the mass distribution contained within a given radius. These are obtained from the moment of inertia tensor for the mass contained within that radius. In Figure 4.5 we plot the resulting run of shape - characterized by the two axis ratios  $b/a$  and  $c/a$ , where  $a \geq b \geq c$  - for a range of radii smaller than the virial radius,  $r < R_{\text{vir}}$ . Spherical haloes would be found in the top right-hand of the figure, with  $b/a \approx c/a \approx 1$ . Haloes at the bottom left-hand corner, where  $c \approx b \ll a$ , resemble elongated spindles while those at the bottom right-hand corner, with  $c \ll b \approx a$ , have a flattened shape.

Each halo is represented by a trail through the shape diagram, with each point on the trail representing the shape of the halo at one particular radius. Figure 4.5 emphasizes the trails of CGV-D\_a (solid) and CGV-G\_a (dashed), while the results for the remaining six haloes are presented in grey. The shape of the quiescently evolving CGV-G\_a halo tends towards a near-spherical shape, as one may expect (Araya-Melo et al. 2009). By contrast, the strongly evolving primary CGV-D\_a halo has a strongly varying shape. In the centre and near the virial radius it is largely spherical, while in between it is more stretched.

### 4.3.2 Halo Assembly and Evolution

Using the merger trees of the primary CGV haloes, we investigate the evolution and assembly history of the eight systems.

We find that only the CGV-D and CGV-H systems experienced major mergers in the last half Hubble time, the other systems undergoing only smaller mergers. From the CGVs we select the two most extreme cases that we study in more detail: CGV-D as a recently formed system and CGV-G as a system that formed very early on. The primary halo of the CGV-D system (CGV-D\_a) formed at a very late moment from many similar-sized progenitors. It only appears as the dominant halo around  $t = 10$  Gyr, when it experiences its last big merger event. By contrast, the central CGV-G halo (CGV-G\_a) formed much earlier, and did not experience any significant merger after  $t = 5.5$  Gyr.

In Figure 4.6, we show the mass accretion history of the primary haloes of both systems. After  $t = 4$  Gyr, CGV-D\_a shows sudden, major accretions of mass on three occasions, at  $t = 6$ , 7.7 and 9.2 Gyr. This halo reached 50% of its final virial mass only at  $t = 8.8$  Gyr. CGV-G\_a, on the other hand, had already reached 50% of its virial mass at  $t = 2.5$  Gyr and does not show any large increases of mass after  $t = 4$  Gyr.

The detailed merger histories of systems CGV-D and CGV-G - limited to haloes larger than  $5 \times 10^7 h^{-1} M_{\odot}$  - are shown in Figure 4.7. The figure depicts the merger tree, along with a corresponding sequence of visual images of the assembly of these systems.



The sequence of images from Figure 4.7 suggests that the assembly takes place within a spatial configuration of hierarchically evolving filamentary structures. For both systems, the many filaments that are clearly visible in the first snapshot merge into a single, thicker filament by the second snapshot. As the system evolves, it collects most of the mass from the filament as it gets accreted onto the haloes. We analyse this in more detail in section 4.4.

### 4.3.3 Dynamical Evolution

We use the dominant mass concentrations in each CGV to get an impression of the global evolution of the mass distribution around the central halo. Using the merger tree of each void halo configuration, we obtain the location of the main and secondary halo for each of the CGVs. To assess the overall dynamics, we first look at the physical dimension of the emerging systems. Figure 4.8 shows the physical distance between the main and secondary halo of each system. In all cases we see the typical development of an overdense region: a gradual slow-down of the cosmic expansion, followed by a turnaround into a contraction and collapse. We find that the average physical distance between the main and secondary haloes increases from about 100 kpc at  $t = 1$  Gyr to 200 kpc at  $t = 6$  Gyr. Subsequently, the systems start to contract to 100 kpc at  $t = 13.5$  Gyr. The exceptions are CGV-H and CGV-G, and as well CGV-E and CGV-F. CGV-E and CGV-F display more erratic behaviour. For a long timespan, CVG-E hovers around the same physical size, turning around only at  $t \approx 9$  Gyr. To a large extent, this is determined by the dominant external mass concentration in the vicinity of CGV-E. Even more deviant is the evolution of CGV-F, where we distinguish an early and a later period of recession and approach between the principal and secondary halo. It is a reflection of a sequence of mergers, in which the two principal haloes at an early time merged into a halo which subsequently started its approach towards a third halo.

The corresponding evolution of the co-moving distance between the two main haloes of each CGV provides complementary information on their dynamical evolution. The evolving co-moving distance is plotted in Figure 4.9. Evidently, each of these overdense void halo systems is contracting in co-moving space. We find that the distance between main and secondary halo decreases from about 400 – 600  $h^{-1}$ kpc at  $t = 1$  Gyr to its current value at  $z = 0$  of less than 200  $h^{-1}$ kpc. CGV-G, CGV-E and CGV-F have a markedly different history than the others. A rapid decline at early times is followed by a shallow decline over the last 10 Gyr. It is the reflection of an early merger of haloes, followed by a more quiescent period in which the merged haloes gradually move towards a third halo.

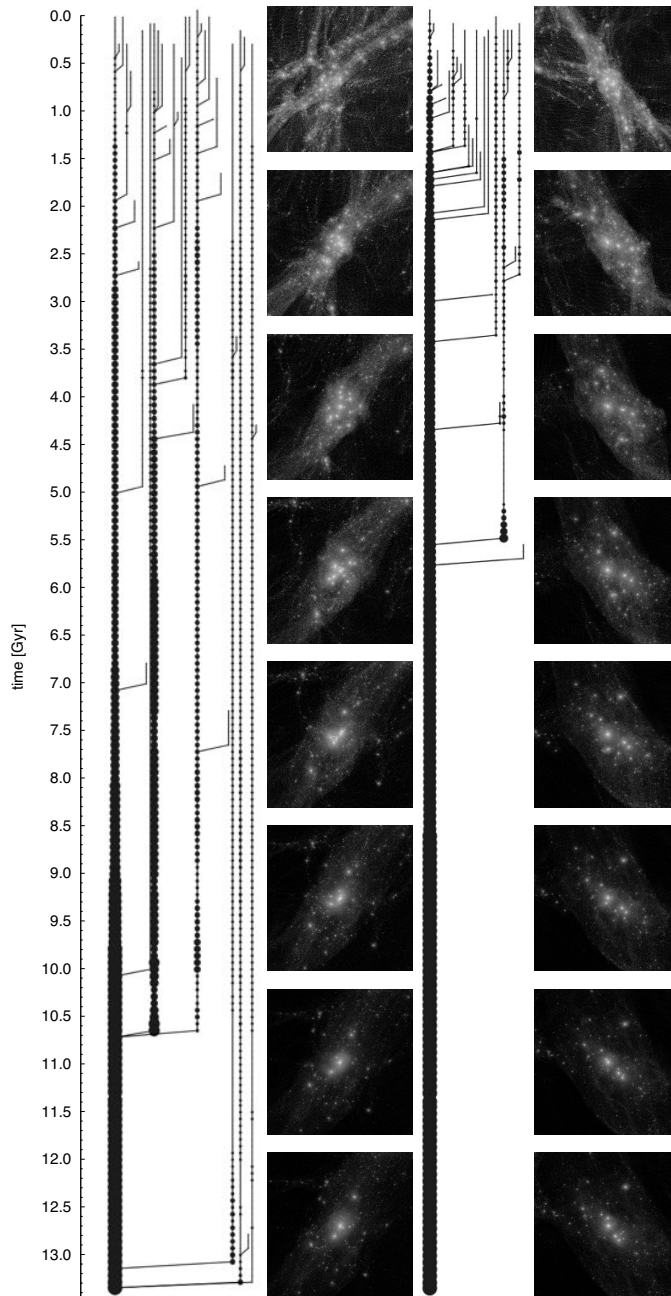


**Figure 4.7:** The merger history of the central haloes of CGV-D (left) and CGV-G (right). The size of the filled circles is proportional to the virial mass of the halo. We show only haloes and subhaloes with a peak mass larger than  $5 \times 10^7 h^{-1} M_{\odot}$  that are accreted before  $z = 0$ . Halo D had a violent merger history, originating from many smaller systems, whereas halo G has remained virtually unchanged since very early in its history.

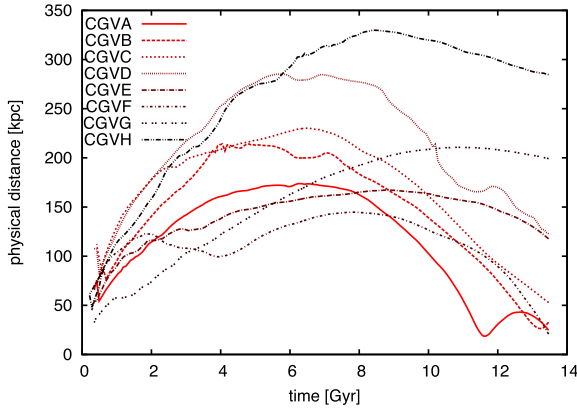


**Figure 4.8:** The relative physical distance between the main and secondary haloes for each of the eight CGVs. Plotted is physical distance, in kpc, as a function of cosmic time (Gyr).

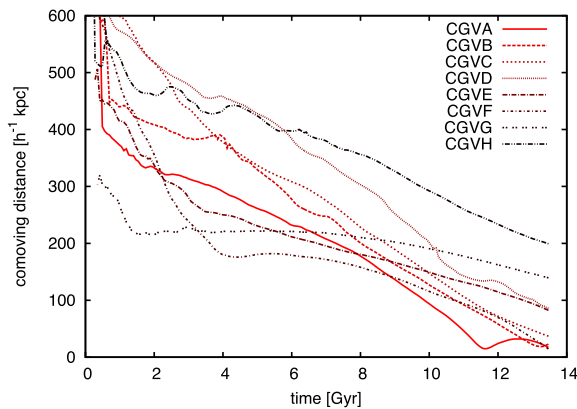


**Figure 4.9:** The relative co-moving distance between the main and secondary haloes for each of the eight CGVs. Plotted is co-moving distance, in kpc, as a function of cosmic time (Gyr).

## 4.4 Large scale environment

The various VGS\_31 resembling halo configurations are embedded in either walls or filaments within the interior of a void. For our study, it is therefore of particular interest to investigate the nature of the large-scale filamentary and planar features in which the CGVs reside.

We first look at the specific structural environment of one particular CGV complex, CGV-G. Subsequently, we inspect the generic structural morphology of the mass and halo distribution around the CGVs. Finally, we assess the dynamical evolution of the anisotropic mass distribution around the CGVs.

### 4.4.1 The web-like environment of CGV-G

The mass distribution within a  $7 h^{-1}$ Mpc box around the CGV-G halo complex is shown in Figure 4.10. It depicts the projected mass distribution along three mutually perpendicular planes. It includes a  $1 h^{-1}$ Mpc sized zoom-in, in the XY plane, onto the halo complex.

The global structure of the mass distribution is that of a wall extending over the YZ plane. In the XY- and XZ-projections, the wall is seen edge-on. They convey the impression of the coherent nature of the wall, in particular along the ridge in the Z-direction. This is confirmed by the NEXUS+ analysis of the morphological nature of the mass distribution, presented in Figure 4.11. At the current epoch we clearly distinguish a prominent wall-like structure (dark grey, lower central frame). Within the plane of the wall, the halo - indicated by a white dot - is located in a filament (light grey, lower right-hand frame). These findings suggest that in the immediate vicinity of the CGVs we should expect haloes to be aligned along the filament.

The filamentary nature of the immediate halo environment may also be inferred from the pattern seen in the Mollweide sky projection of the surrounding dark matter distribution. Figure 4.12 shows this for the dark matter distribution around CGV-G out to a radius of  $1 h^{-1}$ Mpc. At  $z = 0$ , the angular distribution is marked by the typical signature of a filament (lower right-hand frame): two high density spots at diametrically opposite locations. These spots indicate the angular direction of the filament in which CGV-G is embedded. In the same figure, we also follow the sky distribution for the CGV-D halo (lower left-hand frame). A similar pattern is seen for this halo, although its embedding filament appears to be more tenuous and has a lower density.

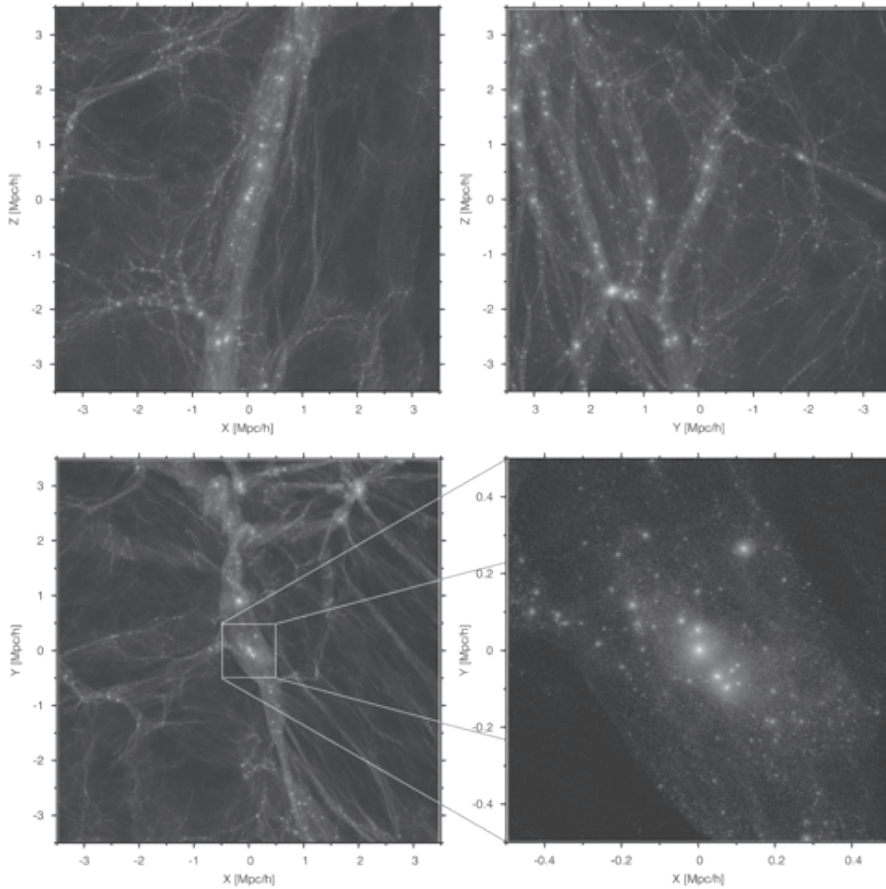


**Figure 4.10:** CGV-G and its large-scale void environment. Each of the frames shows the projected density distribution, within a  $1 h^{-1}$  Mpc thick slice in a  $7 h^{-1}$  Mpc wide region around CGV-G. Top left: XZ plane; top right: YZ plane; bottom left: XY plane. Bottom right: a  $1 h^{-1}$  Mpc wide zoom-in onto the XY plane, centred on CGV-G. Particularly noteworthy is the pattern of largely aligned tenuous intravoid filaments in the YZ plane.

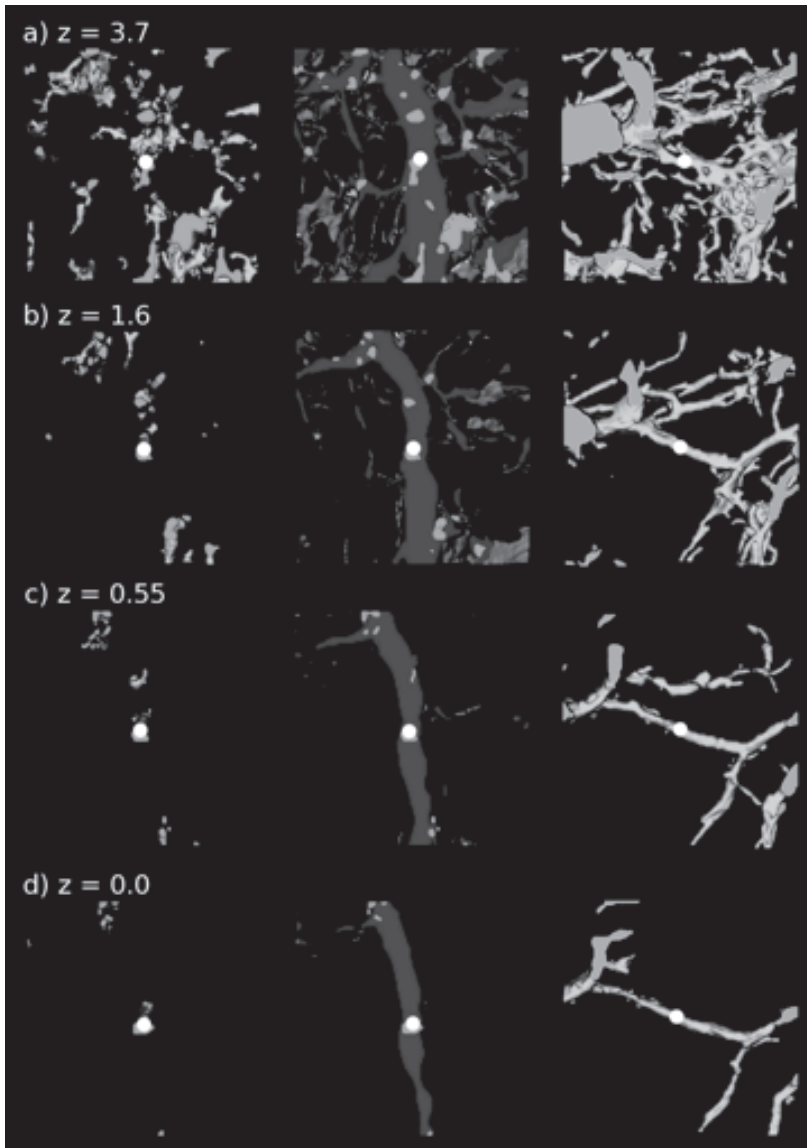


**Figure 4.11:** The evolution of the morphology of the mass distribution around the central halo of CGV-G. The wall-like (dark grey) and filamentary (light grey) features have been identified with the help of NEXUS+ . The frames show the features in a box of  $5 h^{-1}\text{Mpc}$  (co-moving) size and  $1 h^{-1}\text{Mpc}$  thickness. Within each frame the location of CGV-G\_a is indicated by a white dot. The figure shows the evolution of the morphological features at four redshifts:  $z = 3.7$ ,  $z = 1.6$ ,  $z = 0.55$  and  $z = 0.0$ . The first two columns correspond to edge-on orientations of the wall, with the leftmost ones showing the filamentary evolution along the wall and the central one that of the evolution of the wall-like features. The right-hand column depicts the evolution of the filamentary structures within the plane of the wall.

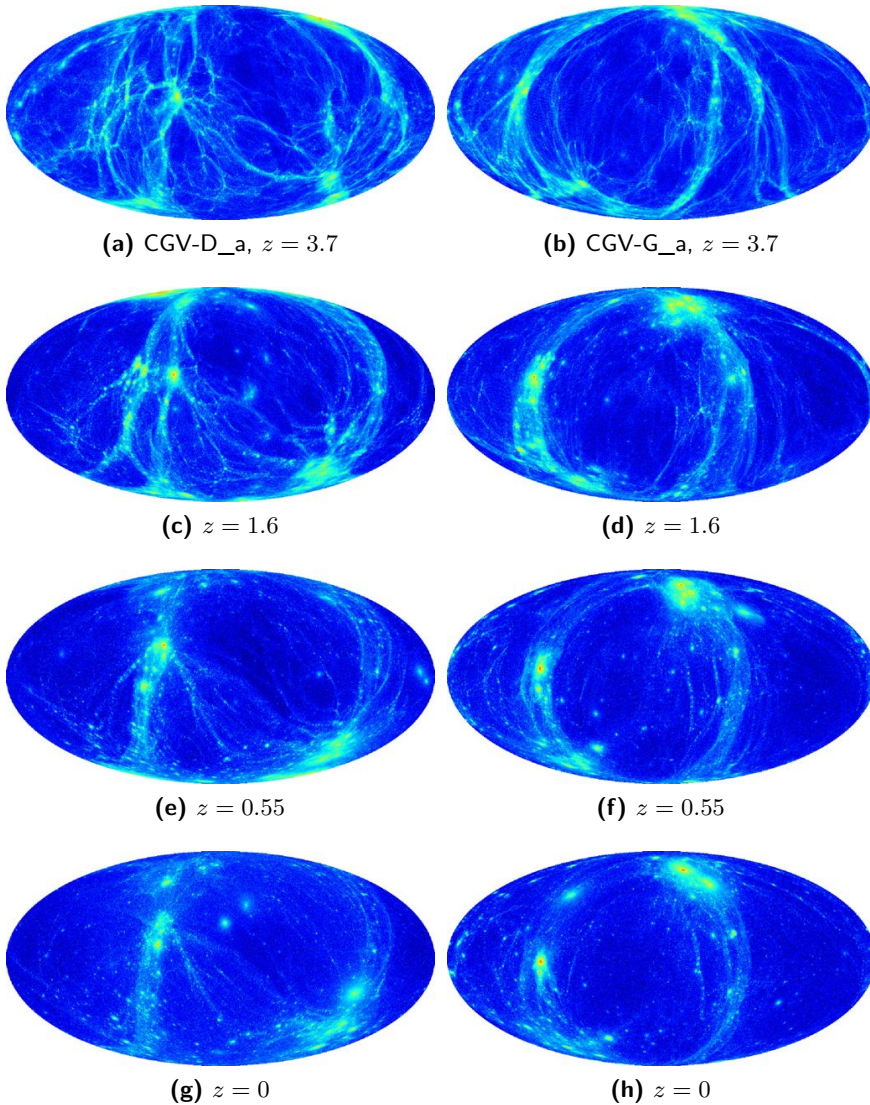


**Figure 4.12:** Mollweide projection of the angular dark matter density distribution around haloes CGV-D\_a (left) and CGV-G\_a (right). To obtain the sky density we projected the dark matter density within a distance of  $1 h^{-1} \text{Mpc}$  from the primary halo centre. The figure depicts the evolution of the sky density at four redshifts:  $z = 3.7$ ,  $z = 1.6$ ,  $z = 0.55$  and  $z = 0$ . The signature of a wall-like configuration is a circular mass arrangement over the sky, that of a filamentary structure consist of two dense spots at diametrically opposite angular positions. In the case of both CGV-D and CGV-G, the evolution towards a wall with an intersecting filament at  $z = 0$  is clearly visible. Dark blue areas correspond to a mass count  $< 10^5 h^{-1} M_{\odot}$ , whereas red areas correspond to a mass count  $> 10^{10} h^{-1} M_{\odot}$ .

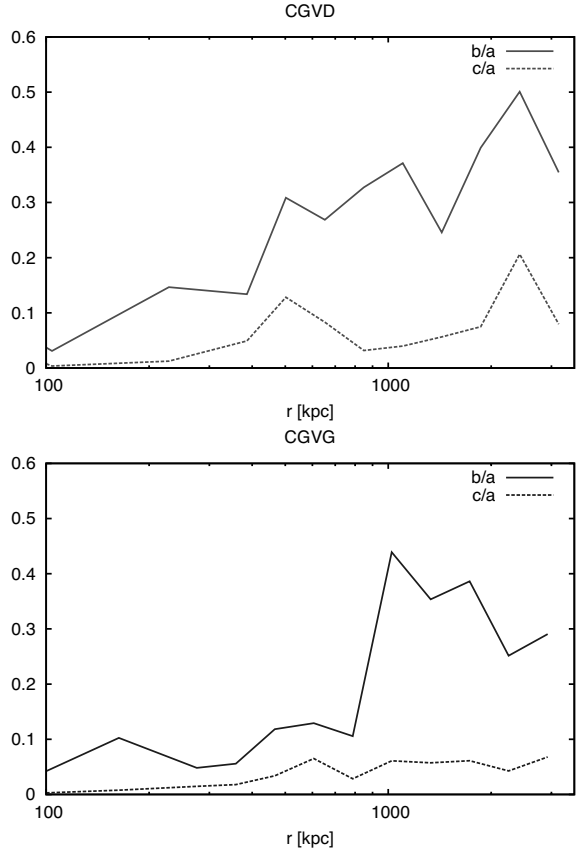


**Figure 4.13:** Shape of the neighbour halo distribution for central haloes CGV-D\_a (top) and CGV-G\_a (bottom) (haloes included have a mass  $M_{\text{vir}} > 10^8 h^{-1} M_{\odot}$ ). The shape is quantified by the ratio of second largest axis to largest axis of the inertia tensor ( $b/a$ ) and the ratio of the smallest over the largest axis ( $c/a$ ).

#### 4.4.2 The wall-like environment of CGVs

The CGV-G constellation is quite generic for void halo systems. We find that all 8 void halo configurations are embedded in prominent walls. The void walls have a typical thickness of around  $0.4 h^{-1} \text{Mpc}$ . They show a strong coherence and retain the character of a highly flattened structure out to a distance of at least  $3 h^{-1} \text{Mpc}$  at each side of the CGV haloes. Five out of the eight haloes reside in filamentary features embedded within the surrounding walls. Most of these filaments are rather short, not longer than  $4 h^{-1} \text{Mpc}$  in length, and have a diameter of around  $0.4 h^{-1} \text{Mpc}$ . Compared to the prominent high-density filaments of the cosmic web on larger scales, void haloes live in very feeble structures.

An additional quantitative impression of the morphology of the typical void halo surroundings may be obtained from Figure 4.13. For haloes CGV-D\_a (top) and CGV-G\_a (bottom), the figure plots the shape of the spatial distribution of neighbouring haloes larger than  $10^8 h^{-1} M_{\odot}$  up to a distance of  $3500 h^{-1} \text{kpc}$ . In



both situations we see that for close distances of the halo, out to  $< 500 h^{-1} \text{kpc}$ , the distribution of surrounding halo is strongly filamentary ( $a > b, c$  and  $c/a < b/a < 0.1 - 0.15$ ). Beyond a distance of  $\approx 800 h^{-1} \text{kpc}$ , the distribution quickly attains a more flattened geometry, characteristic of a wall-like configuration ( $a > b > c$ ).

In all, we find that the environment of our selected void haloes displays the expected behaviour for structure in underdense void regions. Since Zel'dovich's seminal publication (Zel'dovich 1970), we know that walls are the first structures to emerge in the Universe. Subsequently, mass concentrations in and around the wall tend to contract into filamentary structures. Within the context of structure emerging out of a primordial Gaussian density field, (Pogosyan et al. 1998) observed on purely statistical grounds that infrastructure within underdense regions will retain a predominantly wall-like character. Following the same reasoning, overdense regions would be expected to be predominantly of a filamentary nature, as we indeed observe them to be.

It is reassuring that our analysis of the large scale environment of void haloes appears to be entirely in line with the theoretical expectation of predominantly wall-like intravoids structures. This conclusion is also confirmed by the evolution of the CGV configurations, as we will discuss extensively in section 4.4.4.

#### 4.4.3 Intravoids Filaments

Within the confines of the wall surrounding the CGV-G void halo complex (Figure 4.10, top right-hand frame), we find a large number of thin tenuous filamentary features. A particularly conspicuous property of these tenuous intravoids filaments is that they appear to be stretched and aligned along a principal direction. It evokes the impression of a filigree of thin parallel threads. The principal orientation of the filigree coincides with that of more pronounced filamentary and planar features that span the extent of the void (see Figure 4.1).

The phenomenon of a tenuous filigree of parallel intravoids filaments, stretching along the principal direction of a void, is also a familiar aspect of the mass distribution seen in many recent large scale cosmological computer simulations. An outstanding and well-known example is that of the mass distribution seen in the Millennium simulation (Springel et al. 2005; Park and Lee 2009). The pattern of aligned thin intravoids filaments is a direct manifestation of the large scale tidal force field which so strongly influences the overall dynamics and evolution of low-density regions (see van de Weygaert and Bond 2008; Platen et al. 2008). Because of the restricted density deficit of voids (limited to  $\delta > -1$ ) the structure, shape and intravoids mass distribution are strongly influenced by the surrounding mass distribution (Platen et al. 2008). Often this is dominated by two, or even more, massive clusters at opposite sides of a void. These are usually responsible for most

of the tidal stretching of the contracting features in the voids interior. Given the collective tidal source, we may readily understand the parallel orientation of the intravoid filaments.

The same external tidal force field is also responsible for directing the filaments in the immediate surroundings of the wall. As may be appreciated from the XZ and XY frame in Figure 4.10, the surrounding void filaments tend to direct themselves towards and along the plane of the wall. Besides affecting the anisotropic planar collapse of the wall, the tidal force field is also instrumental in influencing the orientation of mass concentrations in the surroundings. Walls and filaments are the result of the hierarchical assembly of smaller scale filaments and walls. The first stage towards their eventual merging with the large scale environment is the gradual re-orientation of the small scale filaments and walls towards the principal plane or axis of the dominant large scale mass concentration.

While the crowded filigree of tenuous intravoid filaments forms such a characteristic aspect of the dark matter distribution in voids, it is quite unlikely we may observe such filaments in the observed galaxy distribution. Most matter in the universe finds itself in prominent large scale filaments. Filaments with diameters larger than  $2 h^{-1}\text{Mpc}$  represent more than 80% of the overall mass and volume content of filament. For walls, 80% of the mass and volume is represented by walls with a thickness larger than  $0.9 h^{-1}\text{Mpc}$  (Cautun et. al, in preparation). The large number of low density void filaments will have hardly sufficient matter content to form any sizeable galaxy-sized dark halo.

#### 4.4.4 Evolution of the intravoid cosmic web

The intention of our study is to investigate the possible origin of the VGS\_31 system. To this end, we have followed the evolution of the web-like void environment of the eight CGVs.

In Figure 4.14, we display the evolution of CGV-D (left) and CGV-G (right) and their environment. At  $z = 0$ , both systems are in a very similar configuration, within a clearly defined wall-like environment. In earlier stages of formation, we see a system consisting of a large number of thin filaments. These filaments rapidly merge into a more substantial dark matter filament, which is embedded in a wall-like plane. The tenuous walls and filaments get rapidly drained of their matter content, while they merge with the surrounding peers. By redshift  $z = 0.55$ , only the most prominent wall remains, aside from a few faint traces of the other sheet-like structures. By that time, the filamentary network is nearly completely confined to the plane of the large wall. Small tenuous filaments have been absorbed by the wall, while the ones within the wall have merged to form ever larger filaments. In the interior of the dominant wall we find the corresponding CGV haloes.

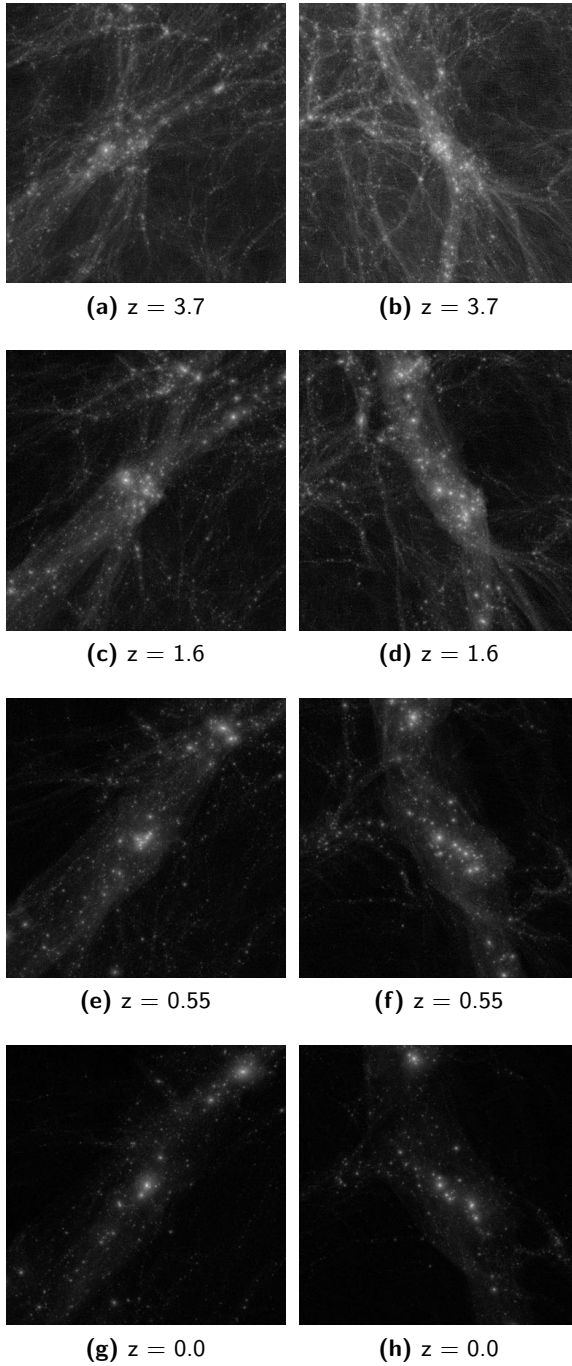


**Figure 4.14:** Evolution of web-like environment of CGV haloes. The density distribution in a box of  $2 h^{-1}\text{Mpc}$  around each halo is shown at four redshifts:  $z = 3.7, 1.6, 0.55$  and  $z = 0.0$ . Left: CGV-D. Right: CGV-G.

Over the most recent 5 billion years, there is very little evolution of the web-like environment of the haloes, with most of the changes being confined to the main sheet. However, there is some variation in time-scale between the different halo configurations. While the CGV-D system has not fully materialized until  $z = 0.55$ , the CGV-G system is already in place at  $z = 1.6$ . Interestingly, as we will notice below, this correlates with a substantial difference between the morphological evolution of the surroundings at high redshifts. From early times onward, CGV-G is found to be embedded in a locally prominent wall. CGV-D, on the other hand, finds itself in the midst of a vigorously evolving complex of small-scale walls and filaments that gradually merge and accumulate in more substantial structures (eg. Figure 4.12).

The evolutionary trend of the voids infrastructure is intimately coupled to the dynamics of the evolving mass distribution. Figure 4.15 correlates the density field in and around two central CGV haloes with the corresponding velocity field. To this end, we depict the mass and velocity field in two mutually perpendicular  $0.5 h^{-1}\text{Mpc}$  slices. The XY plane is the plane of the wall in which the halo is embedded. The YZ plane is the one perpendicular to that and provides a edge-on view of the wall. The vector arrows show the velocity with respect to the bulk velocity of the primary halo.

The wall in which CGV-A is embedded still contains an intricate network of small and thin filaments. Within the wall we observe a strong tendency for mass to flow out of the area centred around the CGV-A haloes. In the XY plane of the wall we recognize stronger motions along the filaments. However, the flow pattern is dominated by the outflow from the sub-voids in the region. The edge-on view of the YZ plane illustrates this clearly, showing the strength of the outflow from the voids below and above the wall. In general, we recognize the outflow in the entire region, inescapably leading to a gradual evacuation from the region and the dissolution of the structural pattern. The mass distribution in the environment of the CGV-D halo has a somewhat different character. It is dominated by the presence of a massive and prominent filament, oriented along the diagonal in the XY-plane. This filament is embedded in a flattened planar mass concentration that also stretches along the filament direction. We clearly observe that the CGV-D halo is participating in a strong shear flows along the filament. The strong migration flow along the filament stands out in the lower part of the YZ plane. In the YZ plane we find it combines with a void outflow out of a large sub-void below the wall, and a weaker outflow out of a less pronounced void above the wall.

Evidently, as matter continues to flow out of the sub-voids and subsequently moves in the walls towards the filaments in their interior and at their boundaries, we will see a gradual dissolution of the intravoid web-like features. In an upcoming

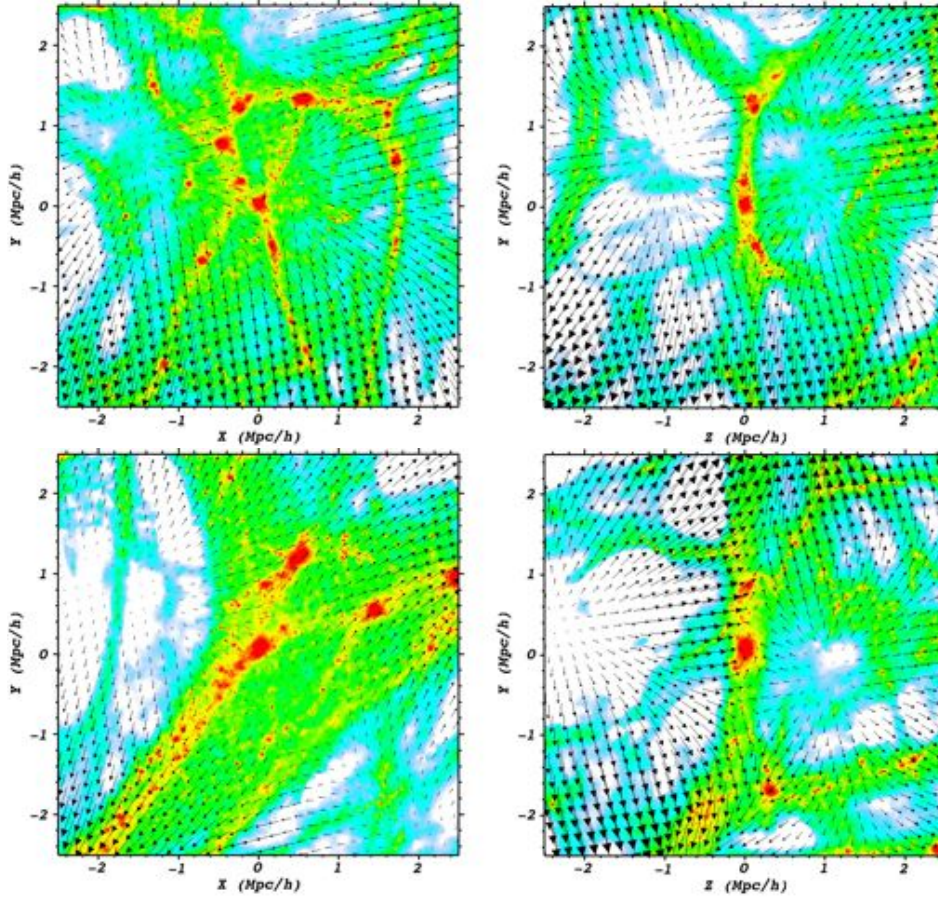


**Figure 4.15:** Density and velocity field around two central haloes, CGV-A\_a and CGV-D\_a. The fields are shown in two mutually perpendicular  $0.5 h^{-1} \text{Mpc}$  thick central slices, the central XY plane (left) and the central YZ plane (right). The XY plane is the plane of the wall in which the halo is embedded. The YZ plane is the one perpendicular to that and provides the edge-on view on the wall. The vector arrows show the velocity with respect to the halo bulk velocity. The density levels are the same in each diagram, the length of the vector arrows is scaled to the mean velocity in the region around the halo (and thus differs in top and bottom row).

publication, we will focus in more detail on the dynamics of the walls, filaments and voids.

A more systematic analysis of the structural morphology around the CGV haloes confirms the visual impression of the evolving system of filaments. Particularly telling is the observed evolution of the (Mollweide) sky projection of evolving mass distribution around the CGV haloes. Figure 4.12 shows how the dark matter sky configuration around primary haloes CGV-D\_a (left column) and CGV-G\_a (right column) evolves from redshift  $z=3.7$  to the present epoch,  $z = 0$ . In both cases, we recognize a circular ring of matter around the sky, the archetypical signature of the wall-like arrangement of the surrounding mass distribution at high redshifts ( $z=3.7$  and  $z=1.6$ ).

Towards later times we observe the gradual evacuation of matter out of the main body of the wall, and its accumulation at the two diametrically opposite spots indicating the direction of the filament in which the haloes are located. In other words, the evolutionary sequence reveals the draining of matter from the main plane of the wall towards its dominant filamentary spine. In particular the evolving CGV-D environment provides a nice illustration of how this process is accompanied by a gradual merging of thin tenuous walls and filaments into a dominant planar structure (cf. the distribution at  $z=1.6$  with  $z=0.55$ ). At  $z = 3.7$ , we cannot yet recognize a coherent wall. Instead, the "spiderlike" pattern on one hemisphere is that of a plethora of small-scale incoherent planar features that subsequently merge and contract into a solid wall, via an intermediate stage marked by two planar structures ( $z=1.6$ ). The situation is somewhat different for CGV-G, which even at a high redshift is already embedded in a solid wall marking a coherent circle over the sky projection.

With the help of the NEXUS+ technique, we systematically analyse the evolution of the morphology and composition of the large-scale mass distribution. Figure 4.11 shows the evolution of the filamentary and wall-like network around CGV-G. Proceeding from  $z=2.4$ , the central row confirms the dramatic evolution of the wall-like structures around the system. At high redshift the region around the halo is dominated by a large wall, the one we recognized in the Mollweide sky projection of Figure 4.12. Perpendicular to the dominant wall, we find the presence of numerous additional sheets. However, these tend to be very tenuous and rapidly merge with the more prominent wall. The entire planar complex has condensed out by  $z=1.6$ . When assessing the evolution of the corresponding filaments, we find that their concentration towards the plane of the wall is keeping pace with the contraction of the major wall. This is clearly borne out by the left-hand column of Figure 4.11, which shows the filamentary features visible at the edge-on orientation of the wall. Within the plane of the wall, on the other hand, we find that

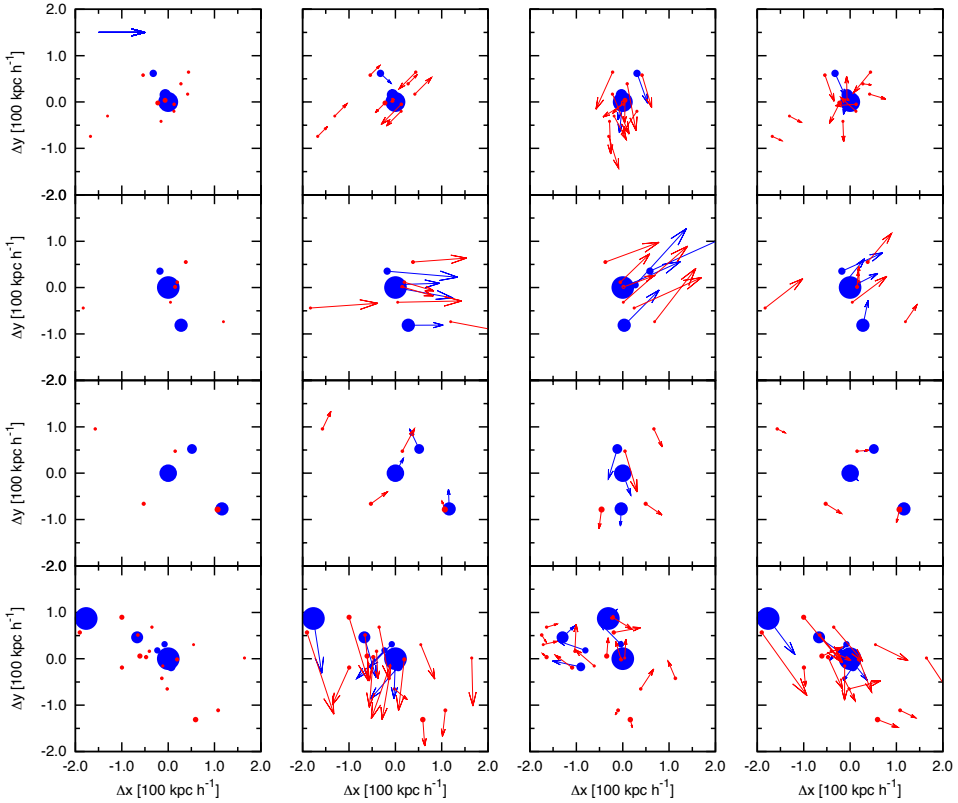


**Figure 4.16:** CGV haloes and subhaloes: spatial distribution and velocities. The figure shows the spatial distribution, in  $200 h^{-1}\text{kpc}$  boxes, of haloes and subhaloes, projected onto the plane along the large scale wall in which the systems are embedded. Blue dots: principal haloes with mass  $M > 10^9 h^{-1}M_{\odot}$ . Red dots: small surrounding haloes with masses between  $10^8 < M < 10^9 h^{-1}M_{\odot}$ . The size of the dots is proportional to the mass of the haloes. In each row, we show the spatial distribution of the haloes (left), the total peculiar velocity (arrow) of each of the objects (central left), the distribution and total peculiar velocity of each of the objects perpendicular to the wall (central right) and the velocity of the haloes/subhaloes wrt. the centre of mass of the objects (right). We show four systems: CGV-A (top row), CGV-D (second row), CGV-G (third row) and CGV-H (bottom row). The arrow in the top left figure indicates a velocity of  $100\text{km/s}$ .

there is a dynamically evolving system of intra-wall filaments. It defines an intricate network of small filaments at high redshifts, especially prominent in the plane of the large wall and somewhat less pronounced perpendicular to this wall. At later times the filamentary network retracts to only a few pronounced filaments, with the CGV-G system solidly located within the locally dominant filament within the wall. The filaments at later times are especially pronounced at the intersection of two or more walls.

We find that the structural evolution shown in Figure 4.11 is archetypical for all eight void halo systems. All systems begin their evolution in a wall, and within the wall in clearly outlined filaments. By  $z = 0.55$ , these structures are the only noticeable web-like features left in the immediate surroundings of the haloes. At later times, the morphology of the large scale distribution hardly evolves any more. The principal difference between the eight void systems is their morphological affiliation at later time. At  $z = 0$  not all are located in a filament. Some of these systems are exclusively located in the main wall, while others find themselves within a remaining filamentary condensation. In other words, void haloes always find themselves within intravoid walls, but not necessarily within intravoid filaments.

## 4.5 CGV halo configurations and VGS\_31: a comparison

Following our investigation of the CGV void haloes and the intravoid filaments in which they reside, we assess the possible dynamical and evolutionary status of a system like VGS\_31 (see section 4.2.2, Beygu et al. (2013)).

A visual inspection of the spatial configuration of haloes and subhaloes in and around the CGVs is presented in Figure 4.16. The blue dots are the principal haloes with mass  $M > 10^9 M_\odot$ , the red dots are small surrounding haloes whose masses range between  $10^8 < M < 10^9 M_\odot$ . The location of the primary halo is taken as the origin of the coordinates.

In four halo systems - CGV-D, CGV-E, CGV-G and CGV-H - the principal haloes have arranged themselves in a conspicuous elongated configuration, much resembling the situation of the VGS\_31 system. On the other hand, we have not found a configuration consisting of two massive primary haloes accompanied by one or two minor haloes. In this respect, none of the eight CGVs resembles VGS\_31. Instead, most systems appear to comprise one dominant principal halo and a few accompanying ones that are less massive.

When considering the distribution of the minor haloes around the CGVs, we find that they tend to follow the spatial pattern defined by the major haloes. The CGV-H system is different: the minor haloes have a much wider and more



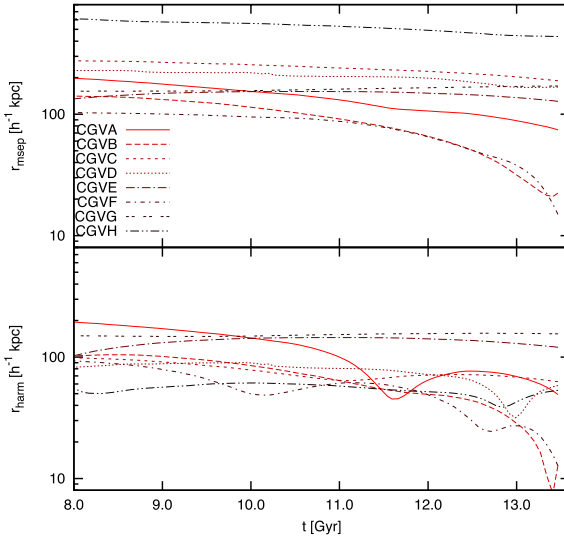


**Figure 4.17:** Evolution of mean separation (top frame) and harmonic radius (bottom frame) of the CGVs. Plotted are  $r_{\text{mseps}}$  and  $R_{\text{harm}}$ , in co-moving units, against cosmic time (in Gyr). Each CGV is represented by a different line character, tabulated in the left bottom corner of the top frame.

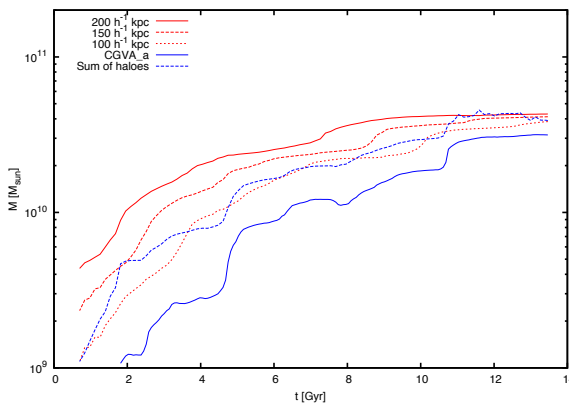


**Figure 4.18:** Mass growth CGV-A haloes and environment. Plotted are the growth of mass  $M$  against cosmic time  $t$ . Solid blue line: central CGV-A halo. Dashed blue line: sum of mass in all three CGV-A haloes. Red lines: dark matter mass growth spherical region centred on centre of mass CGV-A system (excluding mass in haloes). Dotted red line: spherical region with radius  $100 h^{-1} \text{ kpc}$ . Dashed red line: spherical region with radius  $150 h^{-1} \text{ kpc}$ . Solid red line: spherical region of radius  $200 h^{-1} \text{ kpc}$ . Note that over the past 3 Gyr, the haloes represent the major share of mass in the region.

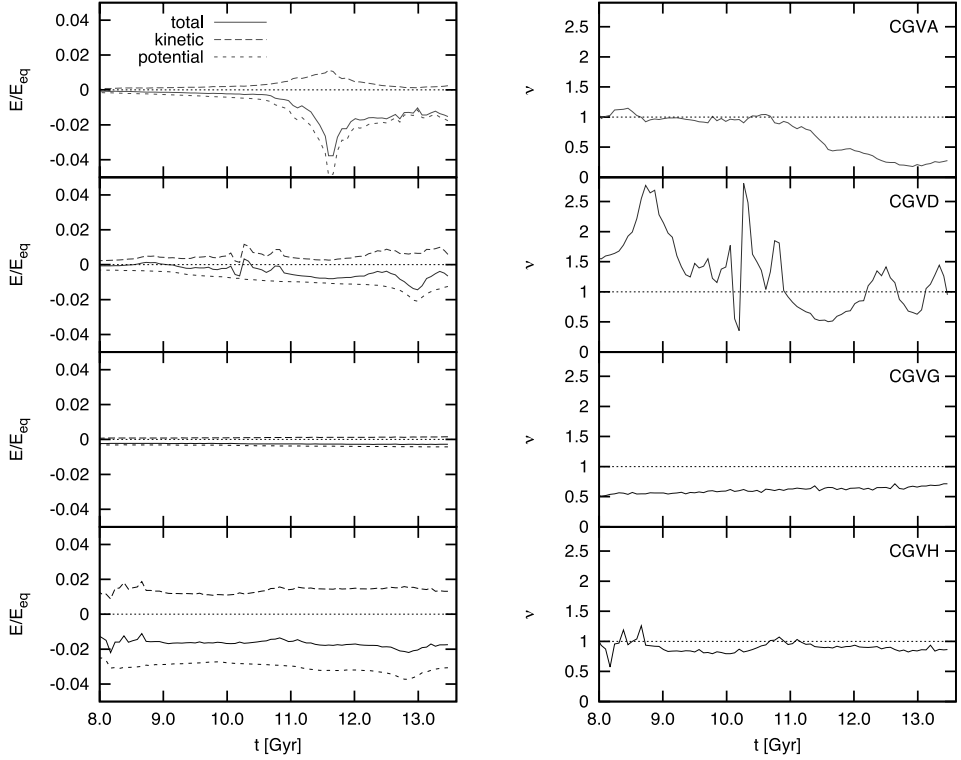


**Figure 4.19:** Energy of evolving CGV halo systems. Left-hand column: time evolution of "Halo system" kinetic energy, potential energy and total energy (see text for definition). Energy is plotted in units of  $E_{eq} = 2 \times 10^{58}$  erg, the potential energy of a  $2 \times 10^{12} M_{\odot}$  halo. Solid line: total energy  $E_{tot}$ . Dashed line: kinetic energy  $E_{kin}$ , dotted line: potential energy  $E_{pot}$ . Right-hand column: evolution of virial ratio  $\mathcal{V}$  (see Equation 4.5). Top row: CGV-A. 2nd row: CGV-D. 3rd row: CGV-G. Bottom row: CGV-H.

random distribution than the more massive ones that are arranged in a filamentary configuration. Overall, however, we do not expect a large number of smaller haloes in the vicinity of these systems.

Part of the systems are moving with a substantial coherent velocity flow along the walls or filaments in which they are embedded. When inspecting the central row of Figure 4.16, we clearly recognize this with the CGV-A and CGV-D systems. Interestingly, they also turn out to be the systems that are undergoing the most active evolution. The latter obviously correlates with a strong evolution of the surrounding mass distribution.

#### 4.5.1 Size evolution of the CGVs

To assess whether the systems have recently formed, we have determined the mean separation and harmonic radius of the CGVs,

$$r_{msep} = \frac{1}{N} \sum_{i,j;i \neq j} |r_{ij}|$$

$$\frac{1}{r_h} = \frac{1}{N} \sum_{i,j;i \neq j} \frac{1}{|r_{ij}|} \quad (4.1)$$

While the mean separation is sensitive to outliers and represents a measure for the overall size of the entire halo system, the harmonic radius of the system quantifies the size of the inner core of the halo system. The evolution of the (co-moving) mean separation and in particular the harmonic radius, shown in Figure 4.17, reflect the gradual contraction of the systems. While CGV-B and CGV-F show a strong contraction over the past 1-2 Gyrs, the overall size of the other systems does not change strongly. This contrasts to the evolution of the core region. As the lower frame of Figure 4.17 shows, in most systems we see a strong and marked evolution over the past 2 to 3 Gyrs, leading to a contraction to a size considerably less than  $100 h^{-1} \text{kpc}$ . The haloes in the core will therefore have interacted strongly, involving either infall of small haloes, mergers of major ones and certainly strong tidal influences on each other.

#### 4.5.2 Energy considerations

One of the remaining issues concerns the level to which the haloes of the CGVs are gravitationally bound. In this respect, we should first evaluate the fraction of matter contained in the haloes. Figure 4.18 plots the growth of mass in a region around the central CGV-A halo. The red lines show the developing dark matter mass content in a spherical region of radius 100, 150 and 200  $h^{-1} \text{kpc}$  around the

central halo (excluding the mass in the haloes themselves). In addition, the figure plots the halo mass evolution. The solid blue line depicts the growing mass of the central halo, the dashed blue line is the sum of the mass of the three main CGV-A haloes.

As time proceeds, we see that a larger and larger fraction of mass in the environment of the CGV-A system gets absorbed by the haloes. At the current epoch, most of the mass within  $100 h^{-1}\text{kpc}$  and  $150 h^{-1}\text{kpc}$  is concentrated in those haloes. Assuming that we may therefore approximate the kinetic and potential energy of the region by that only involving the mass in the haloes, we may get an impression of in how far the halo system is gravitationally bound and tends towards a virial equilibrium.

To this end, we make a rough estimate of the energy content of the halo system. We approximate the kinetic and potential energy by considering each of the haloes as point masses with mass  $m_i$ , location  $\vec{r}_i$  and velocity  $\vec{v}_i$ . Note that by doing so we ignore the contribution of the more diffusely distributed dark matter in the same region, which at earlier times is dynamically dominant but gradually decreases in importance (see Figure 4.18). Also, it ignores the contribution of the surrounding mass distribution to the potential energy. The kinetic energy of the system of  $N$  CGV haloes, wrt. its centre of mass, is

$$E_K = \frac{1}{2} \sum_{i=1}^N m_i (\vec{v}_i - \vec{v}_{CM})^2, \quad (4.2)$$

while the potential energy of the system is computed from

$$E_G = - \sum_{i=1}^N \sum_{j=1}^N \frac{Gm_i m_j}{|\vec{r}_i - \vec{r}_j|}. \quad (4.3)$$

In the left-hand column of Figure 4.19 we plot the evolution of the kinetic, potential and total energy,

$$E_{tot} = E_K + E_G \quad (4.4)$$

of four halo systems (CGV-A, CGV-D, CGV-G and CGV-H). The energy is plotted in units of  $E_{eq} = 2 \times 10^{58}$  erg, which is approximately the potential energy of  $2 \times 10^{12} M_\odot$  haloes at 1Mpc distance. We see that half of the systems have a rather quiescent evolution. Of these, CGV-H strongly and CGV-H marginally gravitationally bound. A far more interesting and violent evolution of the energy content of the halo systems CGV-A and CGV-D. Both involve an active and violent merger history, marked by a continuous accretion of minor objects and a few

major mergers. In particular the major mergers are accompanied by a strong dip in the potential and binding energy.

To get an impression of the corresponding energy stability, we plot the evolution of the virial ratio,

$$\mathcal{V} = \frac{2E_K}{E_G}, \quad (4.5)$$

in the second column of Figure 4.19. For a fully virialised object,  $\mathcal{V} = 1$ . While the computed  $\mathcal{V}$  parameter only provides an impression of the energy state of the systems, it does confirm the impression that CGV-H and CGV-G are halo systems that are in largely in equilibrium. At the same time, the same diagrams for the CGV-A and CGV-D systems reflect their violent history. This appears to continue up to recent times.

### 4.5.3 The origin of VGS\_31

Translating the CGVs to VGS\_31, we note that all haloes detected at  $z = 0$ , are local to their environment. They, and their progenitors, were never further removed than 330 kpc from the main halo. Even if so far removed, we find that the distance between the haloes rapidly decreased at early times. We therefore conclude that the galaxies in VGS\_31 originated in the same region, and originally were probably located in the same proto-wall, and possibly even proto-filament. In other words, the galaxies in the VGS\_31 system did not meet just recently, but have been relatively close to each other all along their evolution. It answers our question whether VGS\_31 might consist of filamentary fragments that only recently assembled.

Moreover, the strong evolution of the several CGV halo cores is an indication for the fact that the two dominant galaxies VGS\_31 - VGS\_31a and VGS\_31b, may recently have undergone strong interactions as indeed their appearance confirms. It would imply that the disturbed nature of the galaxies of VGS\_31 is a result of recent interactions between the galaxies. On the other hand, other CGVs had a rather quiescent history. If VGS\_31 would correspond to one of these systems, we may not have expected the marks of recent interaction that we see in VGS\_31a and VGS\_31b.

## 4.6 Discussion & Conclusions

In this study, we have investigated the formation history of dark matter halo systems resembling the filamentary void galaxy system VGS\_31 (Beygu et al. 2013). The VGS\_31 system is a 120kpc long elongated configuration of 3 galaxies found

in the Void Galaxy Survey (Kreckel et al. 2011). In the CosmoGrid simulation we looked for systems of dark haloes that would resemble the VGS\_31 system. To this end, we invoked a set of five criteria. In total, eight systems were identified, CGV-A to CGV-H.

The  $2048^3$  particle CosmoGrid simulation has a rather limited volume,  $V = 21 h^{-1}\text{Mpc}^3$ , but a very high spatial resolution. While its limited size impedes statistically viable results on large scale clustering as its volume is not representative for the universe, its high mass resolution renders it ideal for high-resolution case studies such as the one described in this study.

While the CosmoGrid simulation is a pure dark matter simulation, a more direct comparison with the HI observations of VGS\_31 will have to involve cosmological hydro simulations that include gas, stars, and radiative processes. Nonetheless, as galaxies will form in the larger dark matter haloes and gaseous filaments will coincide with the more substantial dark matter filaments, our study provides a good impression of the expected galaxy configurations in voids. Nonetheless, it is good to realize that most of the intricate structure seen in our simulations would contain too small amounts of gas to be observed.

For each of the CGVs we examined the formation history, the merging tree, and the morphology of the large scale environment. In our presentation, we focus on the two systems that represent the extremes of the VGS\_31 resembling halo configurations. System CGV-G formed very early in the simulation and remained virtually unchanged over the past 10 Gyr. CGV-D, on the other hand, formed only recently and has been undergoing mergers even until  $z = 0$ .

We find that all CGVs are located in prominent intra-void walls, whose thickness is in the order of  $0.4 h^{-1}\text{Mpc}$ . Five halo complexes are located within filaments embedded in the intra-void wall. In all situations the filamentary features had formed early on, and were largely in place at  $z \approx 1.6$ . These intra-void filaments are short and thin, with lengths less than  $4 h^{-1}\text{Mpc}$  and diameters of  $\sim 0.4 h^{-1}\text{Mpc}$ .

The spatial distribution of dark matter haloes resembles that of the dark matter. We see the same hybrid filament-wall configuration as observed in the dark matter distribution. Close to the main halo, within a distance smaller than  $700 h^{-1}\text{kpc}$ , the neighbouring haloes are predominantly distributed along a filament. On larger scales, up to  $\approx 3.5 h^{-1}\text{Mpc}$ , the haloes are located in a flattened wall-like structure.

In addition to our focus on the evolving dark matter halo configurations, we also studied the morphology and evolution of the intricate filament-wall network in voids. Our study shows the prominence of walls in the typical void infrastructure. Unlike the larger scale overdense filaments, intra-void filaments are far less outstanding with respect to the walls in which they are embedded.

What about VGS\_31? Our study implies it belongs to a group of galaxies that was formed in the same (proto)filament and has undergone a rather active life over the last few Gigayears. The galaxies in the VGS\_31 system did not meet just recently, but have been relatively close to each other all along their evolution. We also find that it is unlikely for VGS\_31 to have many smaller haloes in its vicinity. The fact that we find quite a diversity amongst the CGVs also indicates that VGS\_31 may not be typical for groups of galaxies in voids.

## Acknowledgements

*We thank Katherine Kreckel, Jacqueline van Gorkom and Thijs van der Hulst for discussions within the context of the VGS project. We also gratefully acknowledge many helpful and encouraging discussions with Bernard Jones, Sergei Shandarin, Johan Hidding and Patrick Bos. Furthermore, we thank Peter Behroozi, Dan Caputo, Arjen van Elteren, Inti Pelupessy and Nathan de Vries for their assistance and useful suggestions. Finally, we thank the anonymous referee for his or her helpful comments.*

*This work was supported by NWO (grants IsFast [#643.000.803], VICI [#639.073.803], LGM [#612.071.503] and AMUSE [#614.061.608]), NCF (grants [#SH-095-08] and [#SH-187-10]), NOVA and the LKBF in the Netherlands. RvdW acknowledges support by the John Templeton Foundation, grant nr. FP05136-O.*

*The CosmoGrid simulations were partially carried out on Cray XT4 at Center for Computational Astrophysics, CfCA, of National Astronomical Observatory of Japan; Huygens at the Dutch National High Performance Computing and e-Science Support Center, SURFsara (The Netherlands); HECToR at the Edinburgh Parallel Computing Centre (United Kingdom) and Loubi at IT Center for Science in Espoo (Finland).*





# 5 | Evolution of star clusters in a cosmological tidal field

*Based on:*

*Steven Rieder, Tomoaki Isbiyama, Paul Langelan, Junichiro Makino, Stephen McMillan and Simon Portegies Zwart*

*Evolution of star clusters in a cosmological tidal field*

*Accepted for publication in MNRAS*

We present a method to couple  $N$ -body star cluster simulations to a cosmological tidal field, using the Astrophysical Multipurpose Software Environment. We apply this method to star clusters embedded in the CosmoGrid dark matter-only  $\Lambda$ CDM simulation. Our star clusters are born at  $z = 10$  (corresponding to an age of the Universe of about 500 Myr) by selecting a dark matter particle and initializing a star cluster with 32,000 stars on its location. We then follow the dynamical evolution of the star cluster within the cosmological environment.

We compare the evolution of star clusters in two Milky-Way size haloes with a different accretion history. The mass loss of the star clusters is continuous irrespective of the tidal history of the host halo, but major merger events tend to increase the rate of mass loss. From the selected two dark matter haloes, the halo that experienced the larger number of mergers tends to drive a smaller mass loss rate from the embedded star clusters, even though the final masses of both haloes are similar. We identify two families of star clusters: native clusters, which become part of the main halo before its final major merger event, and the immigrant clusters, which are accreted upon or after this event; native clusters tend to evaporate more quickly than immigrant clusters. Accounting for the evolution of the dark matter halo causes immigrant star clusters to retain more mass than when the  $z=0$  tidal field is taken as a static potential. The reason for this is the weaker tidal field experienced by immigrant star clusters before merging with the larger dark matter halo.

## 5.1 Introduction

Globular clusters are dense self gravitating systems of a few  $10^4$  to  $\sim 10^6$  stars (Brodie and Strader 2006). With an age of about 12.6 Gyr (Krauss and Chaboyer

2003) they are among the oldest objects in the universe and tend to populate the haloes of galaxies. Their age is consistent with being born between  $z = 12$  to 7, which is consistent with the results of  $\Lambda$ CDM simulations (Kravtsov and Gnedin 2005).

From the time the clusters were born on galaxies grow by about a factor 100 in mass via mergers to their current mass, size and morphology (White and Rees 1978; Peacock 1999). The environment in which the globular clusters evolved since their birth has consequently changed quite dramatically over their lifetimes. These changes may have a profound effect on the evolution of star clusters.

Most modern star-cluster simulations take some sort of background potential of the host galaxy into account. This started already in the early 1990s with Chernoff and Weinberg (1990), and soon afterwards became a lively industry. Many simulations have been performed with a fixed tidal limit (Vesperini and Heggie 1997; Portegies Zwart et al. 1998; Giersz 2001) whereas other include some sort of tidal potential with a more fluent description of the tidal field (Gnedin and Ostriker 1997; Takahashi and Portegies Zwart 2000; Lamers et al. 2010). In most of these simulations the cluster orbit was circular and did not change with time. In a few cases the orbit was allowed to be eccentric, but still did not change with time (Baumgardt and Makino 2003; Giersz and Heggie 2011, 2009). The next refinement was the relaxing of the orbital parameters, allowing the cluster orbit to change (Tanikawa and Fukushige 2005, 2010; Praagman et al. 2010; Renaud et al. 2011; Berentzen and Athanassoula 2012; Renaud and Gieles 2013). The evolution of star clusters in a live galactic potential combined with parametrized cluster evolution was studied by Kruijssen et al. (2011), and Matsui et al. (2012) performed simulations in which they resolve the formation of star clusters in a single galaxy merger event.

However, the mass evolution of the parent galaxy is generally ignored in all these simulations, except for the few cases with a galaxy merger (Saitoh et al. 2009; Renaud et al. 2011; Kruijssen et al. 2012; Renaud and Gieles 2013).

In this paper we study the evolution of star clusters in a cosmological environment. The background potential against which the star clusters are evolved, are taken from the CosmoGrid dark-matter only  $\Lambda$ CDM simulation (Portegies Zwart et al. 2010a). We selected two Milky Way like haloes in which the star clusters are simulated. The coupling between the cosmological simulation and the star cluster is realized via the Astrophysical Multipurpose Software Environment (AMUSE) (Portegies Zwart et al. 2009, 2011, 2013; Pelupessy et al. 2013). In these simulations we initialize a total of 30 star cluster at  $z = 10$ , and evolve them together with the cosmological simulation up to  $z = 0$ .

## 5.2 The experimental setup

We simulate star clusters in a  $\Lambda$ CDM environment. We do this in two steps, first by calculating the  $\Lambda$ CDM environment and then using the tidal field from this environment as an external tidal field for the star cluster simulations. We investigate the results of two distinct regions in the  $\Lambda$ CDM environment.

### 5.2.1 The CosmoGrid $N$ -body simulation

The cosmological simulation employed in this article originates from the CosmoGrid calculation (Portegies Zwart et al. 2010a; Ishiyama et al. 2013), which is a dark matter-only  $\Lambda$ CDM simulation of  $2048^3$  particles in a  $(21 h^{-1} \text{Mpc})^3$  co-moving cosmological volume. We performed these simulations using the GreeM (Ishiyama et al. 2009b, 2012) and SUSHI (Groen et al. 2011) codes. GreeM is a massively parallel TreePM code based on the implementation of Yoshikawa and Fukushige (2005). The SUSHI code is an extension of the GreeM code, which can run on a planet wide grid of supercomputers. Within both codes, the equations of motion are integrated in co-moving coordinates using the leap-frog scheme with a shared, adaptive timestep. In this simulation each particle has a mass of  $1.28 \times 10^5 M_{\odot}$ . In total, we have 556 snapshots, separated by  $dt \simeq 35 \text{Myr}$  (for  $t < 7.5 \text{Gyr}$ ) and  $dt \simeq 17.5 \text{Myr}$  (for  $t \geq 7.5 \text{Gyr}$ ). The CosmoGrid simulation lasted from  $z = 65$  to  $z = 0$ . We employed the following cosmological parameters:  $\Omega_0 = 0.3$ ,  $\lambda_0 = 0.7$ ,  $h = 0.7$ ,  $\sigma_8 = 0.8$ ,  $n = 1.0$ . For more details on the simulation see Portegies Zwart et al. (2010a); Ishiyama et al. (2013).

### 5.2.2 Halo catalogue

We use the halo finder Rockstar (Behroozi et al. 2013a) to identify haloes in each snapshot. Rockstar is based on adaptive hierarchical refinement of friends-of-friends groups in six dimensions and allows for the robust tracking of subhaloes. We use the Consistent Trees merger tree code from Behroozi et al. (2013b) to construct the merger history for all haloes identified by Rockstar. We use AMUSE to find the radial density profiles for our haloes.

From the  $z = 0$  haloes, we then select two haloes, based on their relative isolation and a mass comparable to that of the Milky-Way Galaxy. The two haloes are quite similar in many respects, but have a different merger history and the number of subhaloes at  $z = 0$  is different.

In Figure 5.1, we present the merger history of the two haloes, both schematically and visually. Halo A completes a major merger at around  $t = 6.5 \text{Gyr}$ , the halo it merges with can be seen in the third figure from the top. At the end of the

**Table 5.1:** Properties of the selected haloes in the final CosmoGrid snapshot.

Halo	$M_{\text{vir}}$ $10^{11} h^{-1}M_{\odot}$	$R_{\text{vir}}$ $h^{-1}\text{kpc}$	$V_{\text{max}}$ $\text{km/s}$	$c_{\text{vmax}}$	$N_{\text{sub}}$	$D_{\text{n}}$ $h^{-1}\text{Mpc}$	b/a	c/a
A	6.33	173.8	140.2	3.53	61	6.30	0.81	0.63
B	4.78	159.4	133.1	3.76	29	0.97	0.73	0.68

$M_{\text{vir}}$  and  $R_{\text{vir}}$  are the virial mass and radius (Bryan and Norman 1998),  $V_{\text{max}}$  is the maximum of the rotation curve,  $c_{\text{vmax}}$  is the concentration parameter,  $N_{\text{sub}}$  is the number of subhaloes with a mass larger than  $10^8 h^{-1}M_{\odot}$ ,  $D_{\text{n}}$  is the distance of the nearest more massive halo. a, b and c are the principal axes of the halo.

simulation (see Figure 5.4a), it is in the process of merging with another similar-sized halo. Other than that, there is no significant interaction between  $t = 6.5$  Gyr and  $t = 13.7$  Gyr. By the end of the simulation, halo A is the largest object within a radius of  $6.3 h^{-1}\text{Mpc}$  (see Table 5.1). Halo B exists in a denser part of the volume, and as a result more structure is visible in the outskirts of its environment (see Figure 5.4b). By  $z = 0$ , it is the largest halo within only  $0.97 h^{-1}\text{Mpc}$ . During its history, it underwent many small merger events, and one long-lasting major merger event that completed around  $t = 11$  Gyr.

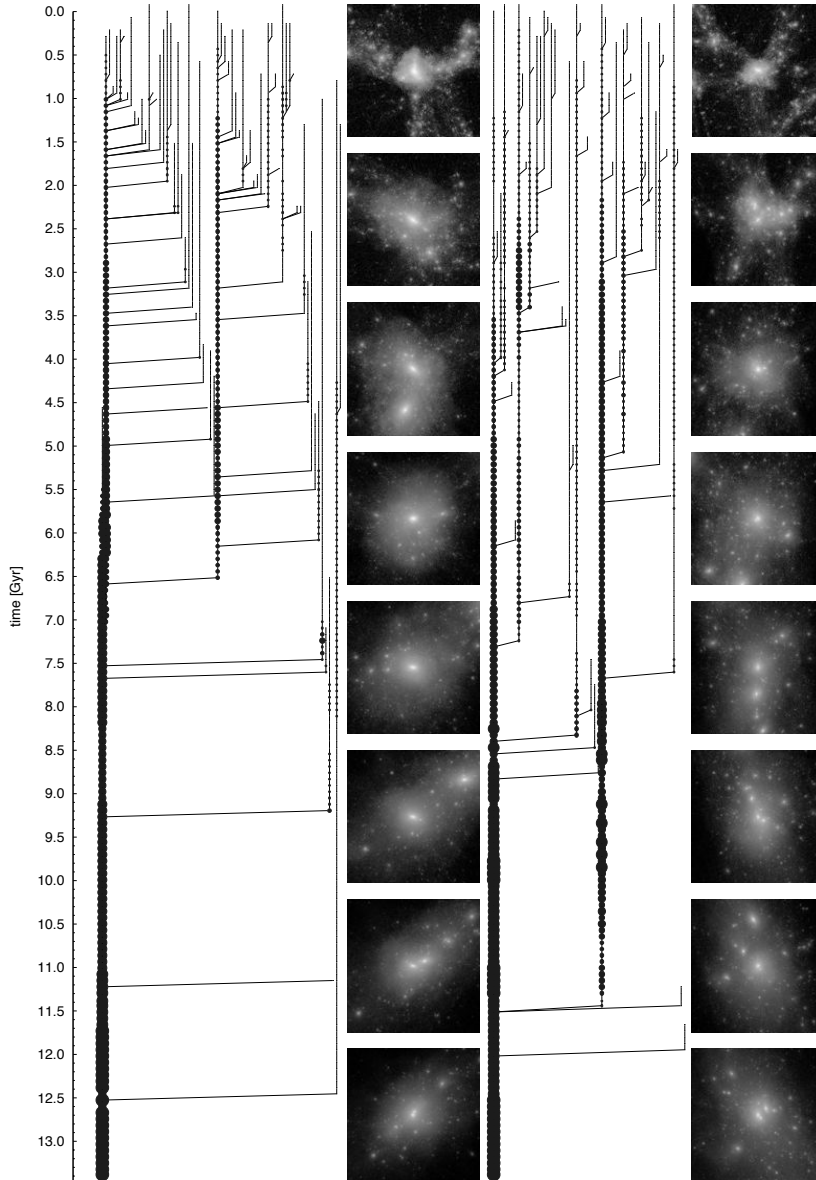
In the mass evolution of both haloes (Figure 5.2), the larger merger events are clearly visible. Since the virial mass includes the mass from subhaloes, the mergers are visible here at the start of interaction, rather than at the end as in Figure 5.1.

The halo density profiles at  $z = 0$  (see Figure 5.3) are consistent with the haloes described in Ishiyama et al. (2013), with concentration parameters  $c_{\text{vmax}}$  of 3.53 and 3.76 for haloes A and B respectively. The lower concentration of halo A may be explained by its ongoing major merger event, which causes the halo to have two cores (see Figure 5.4a).

### 5.2.3 The clusters

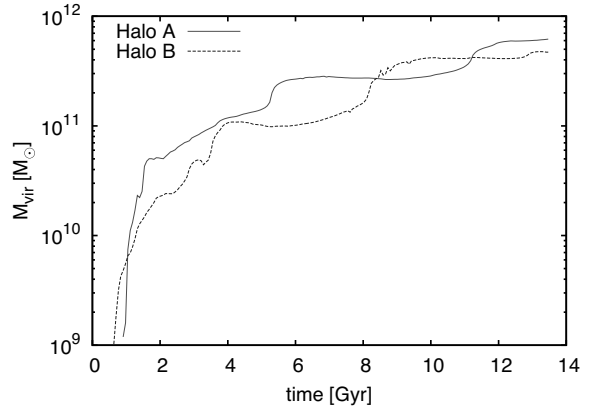
We select a total of 30 dark-matter particles from the  $z = 0$  snapshot. For both haloes we select 15 particles at random, equally divided over three bins at galactocentric radius  $3 \pm 0.05 h^{-1}\text{kpc}$ ,  $6 \pm 0.05 h^{-1}\text{kpc}$  and  $12 \pm 0.05 h^{-1}\text{kpc}$ . These selected particles are considered the globular clusters for which we will calculate the evolution. Since we do not apply further restrictions in the selection criteria, the clusters may (and likely will) have their peri- and apocentres well outside these bins. In Figure 5.5, we show a projection of these particles in the central region of their host halo at  $z = 0$ .

We locate the selected dark-matter particles at  $z = 10$ , which corresponds

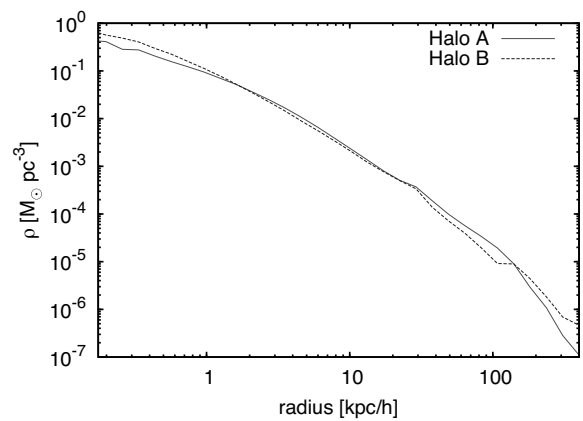


**Figure 5.1:** The merger history of the two selected dark-matter haloes A (left) and B (right). The size of each circle is proportional to the virial mass of the halo. Only haloes and subhaloes with a peak mass larger than  $5 \times 10^8 h^{-1} M_{\odot}$  that are accreted at  $z = 0$  are plotted. The bottom two halo images are identical to those in Figure 5.4.

**Figure 5.2:** Evolution of the virial mass of the two selected haloes A and B. Halo A experiences major merger events around 5 Gyr and 11 Gyr, while halo B experiences a long-lasting major merger event from around 8 Gyr on.



**Figure 5.3:** Radial density profiles of the two selected haloes A and B and their environment out to  $400 h^{-1} \text{kpc}$  at  $z = 0$ . The clusters are selected at galactocentric radii of 3, 6 and  $12 h^{-1} \text{kpc}$ .



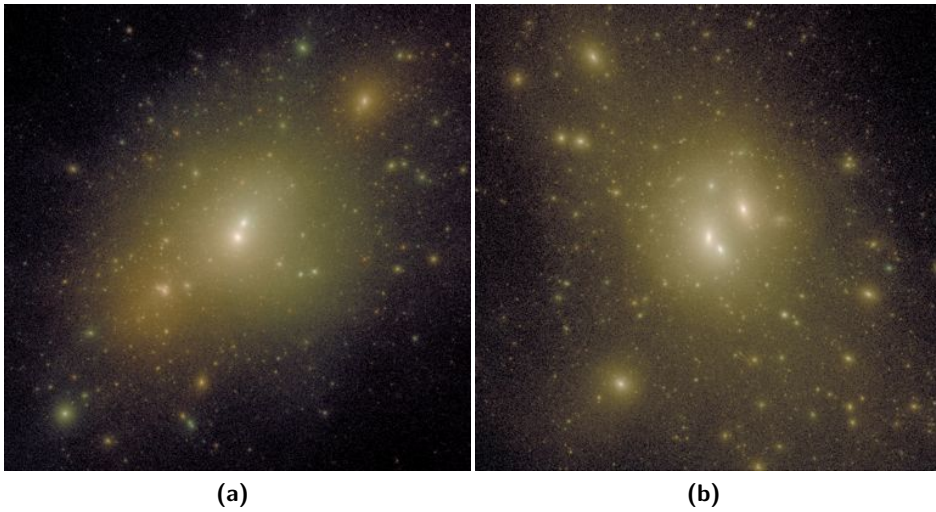


**Figure 5.4:** Projected image of the two selected haloes A (left panel) and B (right panel), in the final snapshot ( $z = 0$ ). The linear dimension of the image is  $400 h^{-1}\text{kpc}$ . The intensity represents the column density (scaled to minimum/maximum values) and the colour is scaled to the velocity dispersion. Each galaxy halo contains about 5 million dark-matter particles.

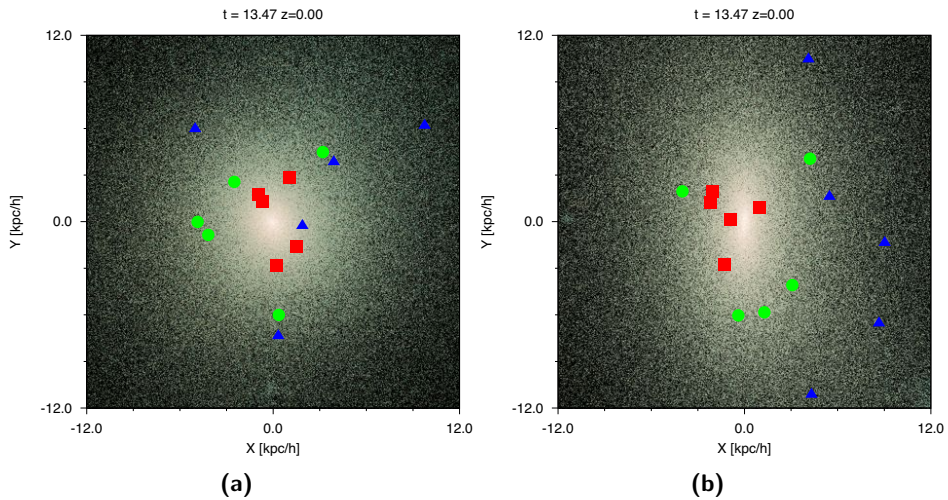


**Figure 5.5:** Projected image of the central portion of the two selected haloes A (left panel) and B (right panel) with their 'globular clusters' at  $z = 0$ . The image size is  $24 h^{-1}\text{kpc}$ . Red squares indicate clusters at  $3 h^{-1}\text{kpc}$  from the halo centre, green circles those at  $6 h^{-1}\text{kpc}$  and blue triangles those at  $12 h^{-1}\text{kpc}$ .

to an age of the universe of  $\sim 0.5$  Gyr. In Figure 5.6 we present the  $z = 10$  image of the two selected haloes with their selected dark-matter particles that will represent globular clusters, and the distributions from which these particles are drawn. In both haloes, the particles that end up in the more central parts of the halo are already the most concentrated in density centres at  $z = 10$ . The particles of halo A are largely concentrated in two regions, in which the haloes that merge around  $t = 6.5$  Gyr form. In contrast, the particles of halo B are more spread out, reflecting the more violent history of this halo.

At the  $z = 10$  snapshot we initialize a 'globular cluster'. Our clusters have 32 000 stars distributed in a Plummer (1911) sphere with a virial radius of 3 pc. The clusters are assumed to be born in virial equilibrium. All stars in the clusters have the same mass and we did not include stellar evolution.

The star clusters are simulated using the AMUSE framework (Portegies Zwart et al. 2009, 2011, 2013; Pelupessy et al. 2013). Our simulation code solves for the equations of motion using Bonsai (Bédorf et al. 2012) and ph4 (McMillan et al. 2012). Bonsai is a Barnes and Hut (1986) tree code that runs on GPUs. It supports both shared timesteps and block timesteps, the latter allowing individual blocks to have different timesteps for increased accuracy in dense regions without slowing the simulation down too much. For this code, we adopted an opening angle (which controls the accuracy, smaller angles being more accurate) of 0.6, we set the smallest timestep to be used to  $1/65536$   $N$ -body time units (Heggie and Mathieu 1986) and we used a softening length of  $0.00125$   $N$ -body length units (0.00375 parsec). Ph4 is a direct  $N$ -body integrator with block time steps and GPU acceleration. In order to directly compare the results to those obtained with Bonsai, we apply the same softening length as before to the runs with ph4.

In order to validate the use of the tree code, we compare a cluster simulated with Bonsai to a reference simulation using ph4. In Figure 5.7, we present the mass and the Lagrangian radii of this simulated cluster as a function of time, for both Bonsai and ph4.

The difference in mass evolution between ph4 and Bonsai remains quite small until about 5 Gyr. After this moment, both clusters go into core collapse and the two codes start to deviate more. Until about 8.5 Gyr, the ph4 cluster displays much higher mass loss than the Bonsai cluster as it expands following core collapse. After 8.5 Gyr, both codes again show similar behaviour.

The Lagrangian radii of the clusters are nearly equal until core collapse occurs at about 5 Gyr. After this, the core collapse is initially deeper in ph4, while after 8.5 Gyr Bonsai reaches the same depth.

From these results, we infer that our Bonsai simulations are not as well suited for determining the internal structure and evolution of the star clusters as ph4



would be, and underestimates mass loss due to core collapse. However, the effect of the tidal field on the mass loss rate is similar in ph4 and Bonsai. Since we investigate only the mass evolution of the clusters due to the tidal field in this article, we conclude that Bonsai gives an adequate indication of the effect of tidal fields on the cluster mass loss, and that it can be used to study the survivability of star clusters.

### 5.2.4 The tidal field

In each snapshot of the CosmoGrid simulation we calculate the tidal tensor at the location of the selected dark-matter particle, which represents a star cluster. The contribution to the tidal tensor  $\mathbf{T}_t$  from a particle with relative position  $\mathbf{r}$  is given by the second derivative of the gravitational potential  $\phi$ :

$$T_t^{ij}(\mathbf{r}') = -\frac{\partial^2 \phi}{\partial r'^i \partial r'^j} \quad (5.1)$$

where  $\mathbf{r}' = \mathbf{r} + \epsilon$ . For the CosmoGrid simulation, the value for the softening length  $\epsilon$  was 175 parsec.

The strength of the tidal field scales as  $\frac{\partial^2 \phi}{\partial^2 \mathbf{r}} \sim \frac{1}{r^3}$ . Any particle at a distance of about  $\epsilon$  will have as much effect on the tidal tensor as the largest halo in the CosmoGrid simulation (containing  $\sim 3 \times 10^8$  particles) would have at a distance of  $\sim 117$  kpc. We therefore include the contribution from all particles within a radius of 125 kpc from our clusters to determine  $\mathbf{T}_t$ .

The strength of the tidal field is calculated from the eigenvalues  $\lambda_i$  and eigenvectors  $\nu_i$  of this tensor  $\mathbf{T}_t$ . The eigenvalues give the magnitude of tidal field, whereas the eigenvectors give the direction along which the system is stretched. This method for calculating the tidal tensor is similar to the one employed in Renaud et al. (2011).

Since we calculate the tidal tensor  $\mathbf{T}_t$  from snapshots of the CosmoGrid simulation and the number of snapshots is limited, we do not have a continuous tidal field. In order to prevent large, sudden changes, we linearly interpolate the tidal tensor between snapshots to create a continuous tidal tensor. In Section 5.2.7, we validate this interpolation method.

### 5.2.5 Combining the clusters and the tidal field

We use the tidal tensor to calculate the external potential acting on each of the stars in the simulated clusters. We integrate the internal potential of the clusters with this external potential using a Bridge-like scheme (Fujii et al. 2007), which is implemented in AMUSE (Portegies Zwart et al. 2013).

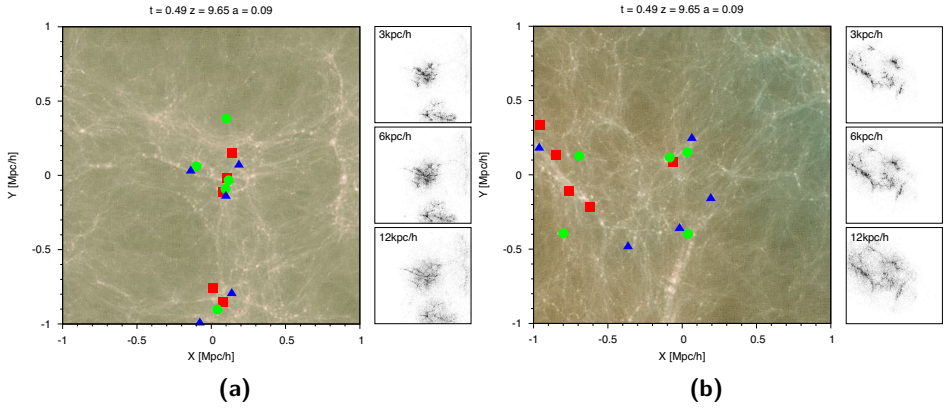


**Figure 5.6:** Projected image of halo A (left) and B (right) at  $z = 9.65$ . The image size is  $2 h^{-1}\text{Mpc}$ . Red squares indicate clusters that at  $z = 0$  were selected at  $3 h^{-1}\text{kpc}$  from the halo centre, green circles those at  $6 h^{-1}\text{kpc}$  and blue triangles those at  $12 h^{-1}\text{kpc}$ . The panels on the right display (from top to bottom) the distributions of particles that end up in spherical shells at  $3, 6$  and  $12 h^{-1}\text{kpc}$  from the halo centres at  $z = 0$ .

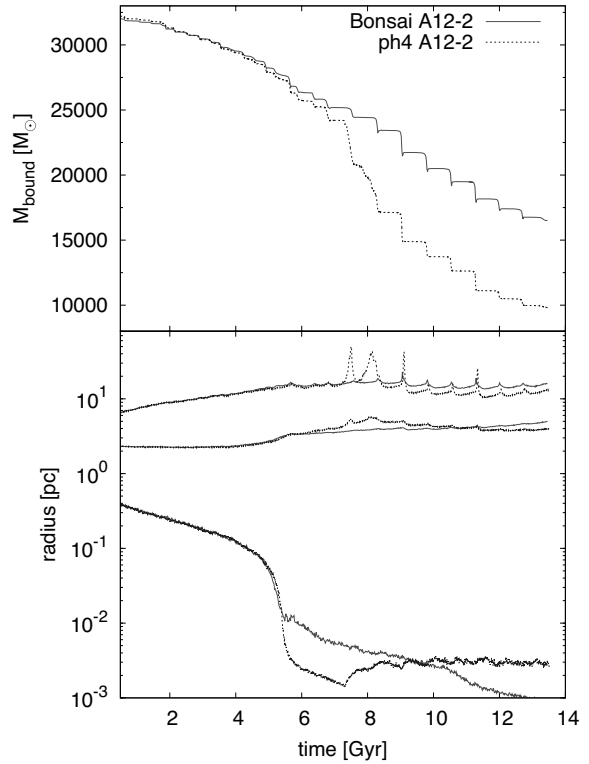


**Figure 5.7:** Evolution of the bound mass (top panel) and the 90%, 50% and 1% Lagrangian radii (top to bottom, bottom panel) of star cluster A12-2. The cluster was simulated with Bonsai (solid curves) and ph4 (dashed curves).

This scheme can be used to combine interacting systems that are calculated in different instances and/or using different codes, i.e. multiple interacting star clusters, globular clusters in a galactic environment, a galactic disk in a halo potential or embedded star clusters (Pelupessy and Portegies Zwart 2011).

In this scheme, the cluster experiences the gravity from the external field through periodic velocity kicks. It alternates between these velocity kicks and a drift due to self gravity evolution of the system. During one time step, the system first experiences a kick of the velocities over a time step  $dt/2$ , then a drift over a time step  $dt$ , and finally another kick over  $dt/2$ . In our setup, the external potential is derived from the CosmoGrid simulation and therefore necessarily fixed, while the clusters receive velocity kicks from the external tidal field.

### 5.2.6 Escaping and bound stars

In the simulations, we calculate a tidal radius from the cluster mass and the strength of the tidal field (given by the largest eigenvalue of the tidal tensor  $\lambda_{\max}$ ). This tidal radius is equal to

$$R_{\text{tidal}} = \left( \frac{GM}{\lambda_{\max}} \right)^{1/3}. \quad (5.2)$$

Particles at a distance from the cluster centre larger than  $R_{\text{tidal}}$  will experience a larger force from the external tidal field than from the cluster's own internal mass. It is then considered an 'escaping particle', and not included in the cluster's bound mass (defined as the total mass inside  $R_{\text{tidal}}$ ). If the particle returns to a position within the tidal radius, this is reversed. If it moves to a distance  $> 10R_{\text{tidal}}$ , the particle is removed from the simulation.

At times when the cluster is located in the centre of a local subconcentration of dark matter or near a halocentre, the value of  $\lambda_{\max}$  may become negative for a short period. In such cases, the tidal radius is not defined. At such times, the bound mass of the cluster is not evaluated and no mass loss is experienced by the cluster. Stars that may have escaped from the cluster during this period will however still be removed once the tidal radius is again defined.

### 5.2.7 Validation

We validate the simulation environment by comparing our results with those obtained using a different method and to a star cluster in isolation. As a reference model, we simulate a star cluster in an orbit with  $R_{\text{apo}} = 12 h^{-1} \text{kpc}$  and  $e = 0.71$  around a point-mass of  $10^{10} M_{\odot}$ , by including this point-mass in the simulation. The simulated cluster contains 8 000 equal-mass stars of  $1 M_{\odot}$  within a Plummer (1911) sphere with a virial radius of 3 pc. We compare this model to a simulation

where we first calculated the tidal field that would be experienced by such a cluster and used this as an external field for the simulation using the Bridge scheme. For this test, we run simulations with ph4, as the large difference in particle masses would make the reference simulation unsuitable for a single-precision tree code like Bonsai.

The mass evolution of these test simulations are presented in Figure 5.8. The difference in the mass evolution of the cluster in the simulations with and without Bridge is quite small, indicating the validity of this method for this set of parameters.

Also, we validate the effect of the discretisation at which the tidal tensor is evaluated. Since the time-resolution of the cosmological simulation is limited to about 35 Myr at high  $z$  and 17.5 Myr at low  $z$ , anomalies will be visible for clusters with an orbital period of this order. Ideally, one would like to increase the number of snapshots for the cosmological simulation in order to obtain a higher time-resolution for the tidal tensor.

In Figure 5.9 we present the mass evolution of a cluster in a static halo potential (Paczynski 1990) with a core mass of  $10^9 M_\odot$  and a core radius of 1 kpc, now using tidal tensors sampled with a time resolution ranging from 1 to 35 Myr. The orbital parameters of the cluster in this potential are  $R_{\text{apo}} = 15$  kpc,  $e = 0.85$ , and the cluster orbits the potential in 670 Myr. The mass loss rates for the clusters using a tidal tensor sampled with a time interval of 1 Myr and 9 Myr have converged in this orbit, while the clusters using tensors sampled with a 17.5 or 35 Myr time interval show a slightly reduced mass loss rate and therefore longer lifetimes. For clusters with closer orbits, this effect will be stronger. In a cosmological setting, any change in the potential that takes place on a timescale similar to or smaller than the sampling rate cannot be taken into account properly, and may also lead to errors in the mass loss rate.

## 5.3 Results

### 5.3.1 The evolution of the selected haloes

We perform simulations of star clusters in two selected haloes, which we call halo A and halo B. Halo A experiences two major merger events, the last of which is not completed by  $z = 0$  (see Figures 5.1 and 5.2), but otherwise its evolution is rather gradual from  $z = 65$  to  $z = 0$ . By the end of the simulation (at  $z = 0$ ) its mass is  $6.3 \times 10^{11} h^{-1} M_\odot$ .

Halo B has a more violent history; it experiences two major mergers, one between 4 Gyr and 5 Gyr and one with comparable mass between 8 Gyr and 10 Gyr

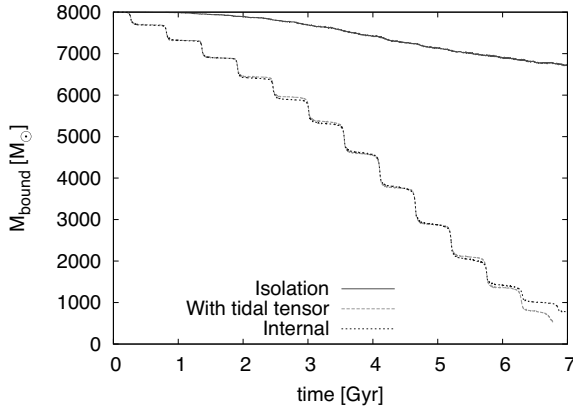


**Figure 5.8:** Mass evolution of a 8000 star cluster in isolation (solid curve), and in orbit around a point mass of  $10^{10} M_{\odot}$  (dashed and dotted curves). The dashed curve gives the mass-evolution of the cluster when the tidal field is incorporated in the gravitational  $N$ -body simulation using Bridge. The tidal field in the latter case was resolved at the resolution of the  $N$ -body integrator. The dotted curve gives the mass-evolution when the point mass is directly included in the simulation.

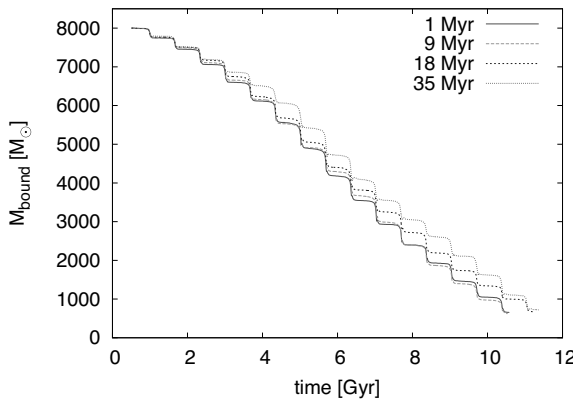


**Figure 5.9:** Mass evolution of a 8000 star cluster with tidal field calculated from a halo potential using the tidal tensor and evaluated using Bridge at discrete time intervals. The cluster orbits in the halo potential with  $R_{\text{apo}} = 15 \text{ kpc}$  and  $e = 0.85$ . In order to study the effect of the time resolution of the tidal field, we evaluate the tidal tensor with time intervals of 1, 9, 18 and 35 Myr.

(see also Figures 5.1 and 5.2). By the end of the simulation at  $z = 0$  it has a mass of  $4.8 \times 10^{11} h^{-1} M_{\odot}$  (see Table 5.1). Even though the total mass of halo B is slightly smaller than that of halo A, both haloes contain a mass of  $7 \times 10^9 h^{-1} M_{\odot}$  within 3 kpc from the halo centre (see Figure 5.3).

In each halo we have selected 15 dark-matter particles which are initialized at  $z = 10$  as star clusters, and evolved with the cosmological simulation as a background potential.

### 5.3.2 The evolution of the star clusters

We perform 30 simulations of star clusters with a tidal field; 15 are initialized in halo A and 15 in halo B. An additional cluster is simulated in isolation, to identify the mass loss component caused by relaxation. For this cluster, a radius of 200 pc is used to determine if stars are bound. All clusters are born at  $z = 10$  (corresponding to an age of the Universe of about 500 Myr) with a total mass of  $\sim 32\,000 M_{\odot}$  and an initial virial radius of 3 parsec for each cluster. All stars have the same mass and we did not include stellar evolution.

In Figure 5.12 and Table 5.2 we present the mass evolution and final masses of these simulations. The mass evolution of all simulated clusters is rather gradual irrespective of the sudden events in the growth of the host haloes. The small and rather sudden changes in mass are caused by the pericentre passages of the clusters in its orbit around the dark matter host. The clusters with a smaller orbital separation at  $z=0$  tend to lose mass at a higher rate.

The averaged final mass of the star clusters in halo A is smaller than the final mass of those that evolved in halo B for each of the radial bins (see Table 5.2). This is consistent with halo B originating from a larger number of less massive haloes, causing the tidal forces experienced by clusters in this halo over time to be smaller. For both haloes the clusters selected around  $3 h^{-1}$  kpc show the strongest mass loss; this is noticeable from the first few Gyr on. This behaviour is as expected from the distribution of particles at  $z = 10$  (see Figure 5.6), where we see that the particles that end up in the central parts are already more concentrated at high redshift. The rate of mass loss for these clusters proceeds more gradual compared to the clusters in wider orbits. Integrated over time clusters lose mass at a rather constant rate.

In Table 5.2 we distinguish between two types of clusters: those that were part of the main halo before the final completed major merger event (at  $t = 6$  Gyr and  $t = 8$  Gyr for haloes A and B, respectively), and those that are accreted upon or after this event. The former we identify with 'native' clusters, and the others as 'immigrants'. The difference between immigrant clusters and native clusters is apparent in Figure 5.10.

In Figure 5.10 we present the orbital evolution of the selected dark-matter

**Table 5.2:** Results for star cluster simulations using Bonsai, with various tidal tensors. Each cluster contains 32 000 equal mass stars of about  $1 M_{\odot}$ , and has an initial radius of 3 parsec. We use a softening length of  $40/N$ . Cluster type is Immigrant (I) or Native (N). The clusters indicated with a bold font are displayed in Figures 5.11 and 5.14.

Cluster ID	Halo	Type	Distance at z=0	Mass at z=0
<b>Isolated</b>				<b>28174 <math>M_{\odot}</math></b>
A3-1	A	I	$3 h^{-1} \text{kpc}$	10157 $M_{\odot}$
A3-2	A	I	$3 h^{-1} \text{kpc}$	15171 $M_{\odot}$
A3-3	A	N	$3 h^{-1} \text{kpc}$	10969 $M_{\odot}$
A3-4	A	N	$3 h^{-1} \text{kpc}$	11085 $M_{\odot}$
A3-5	A	N	$3 h^{-1} \text{kpc}$	10169 $M_{\odot}$
<b>Average</b>				<b>11510 <math>M_{\odot}</math></b>
<b>A6-1</b>	A	I	$6 h^{-1} \text{kpc}$	17906 $M_{\odot}$
A6-2	A	N	$6 h^{-1} \text{kpc}$	24130 $M_{\odot}$
A6-3	A	N	$6 h^{-1} \text{kpc}$	14964 $M_{\odot}$
<b>A6-4</b>	A	N	$6 h^{-1} \text{kpc}$	17978 $M_{\odot}$
A6-5	A	N	$6 h^{-1} \text{kpc}$	18430 $M_{\odot}$
<b>Average</b>				<b>18682 <math>M_{\odot}</math></b>
A12-1	A	I	$12 h^{-1} \text{kpc}$	21677 $M_{\odot}$
A12-2	A	I	$12 h^{-1} \text{kpc}$	16487 $M_{\odot}$
A12-3	A	N	$12 h^{-1} \text{kpc}$	17574 $M_{\odot}$
A12-4	A	N	$12 h^{-1} \text{kpc}$	15873 $M_{\odot}$
A12-5	A	N	$12 h^{-1} \text{kpc}$	16904 $M_{\odot}$
<b>Average</b>				<b>17703 <math>M_{\odot}</math></b>
B3-1	B	I	$3 h^{-1} \text{kpc}$	19422 $M_{\odot}$
B3-2	B	N	$3 h^{-1} \text{kpc}$	18974 $M_{\odot}$
B3-3	B	N	$3 h^{-1} \text{kpc}$	16366 $M_{\odot}$
B3-4	B	N	$3 h^{-1} \text{kpc}$	15633 $M_{\odot}$
B3-5	B	N	$3 h^{-1} \text{kpc}$	20839 $M_{\odot}$
<b>Average</b>				<b>18247 <math>M_{\odot}</math></b>
B6-1	B	I	$6 h^{-1} \text{kpc}$	24774 $M_{\odot}$
<b>B6-2</b>	B	N	$6 h^{-1} \text{kpc}$	18446 $M_{\odot}$
<b>B6-3</b>	B	I	$6 h^{-1} \text{kpc}$	15988 $M_{\odot}$
B6-4	B	N	$6 h^{-1} \text{kpc}$	21128 $M_{\odot}$
B6-5	B	N	$6 h^{-1} \text{kpc}$	21398 $M_{\odot}$
<b>Average</b>				<b>20347 <math>M_{\odot}</math></b>
B12-1	B	I	$12 h^{-1} \text{kpc}$	19986 $M_{\odot}$
B12-2	B	I	$12 h^{-1} \text{kpc}$	23479 $M_{\odot}$
B12-3	B	N	$12 h^{-1} \text{kpc}$	25819 $M_{\odot}$
B12-4	B	N	$12 h^{-1} \text{kpc}$	26374 $M_{\odot}$
B12-5	B	I	$12 h^{-1} \text{kpc}$	22137 $M_{\odot}$
<b>Average</b>				<b>23559 <math>M_{\odot}</math></b>

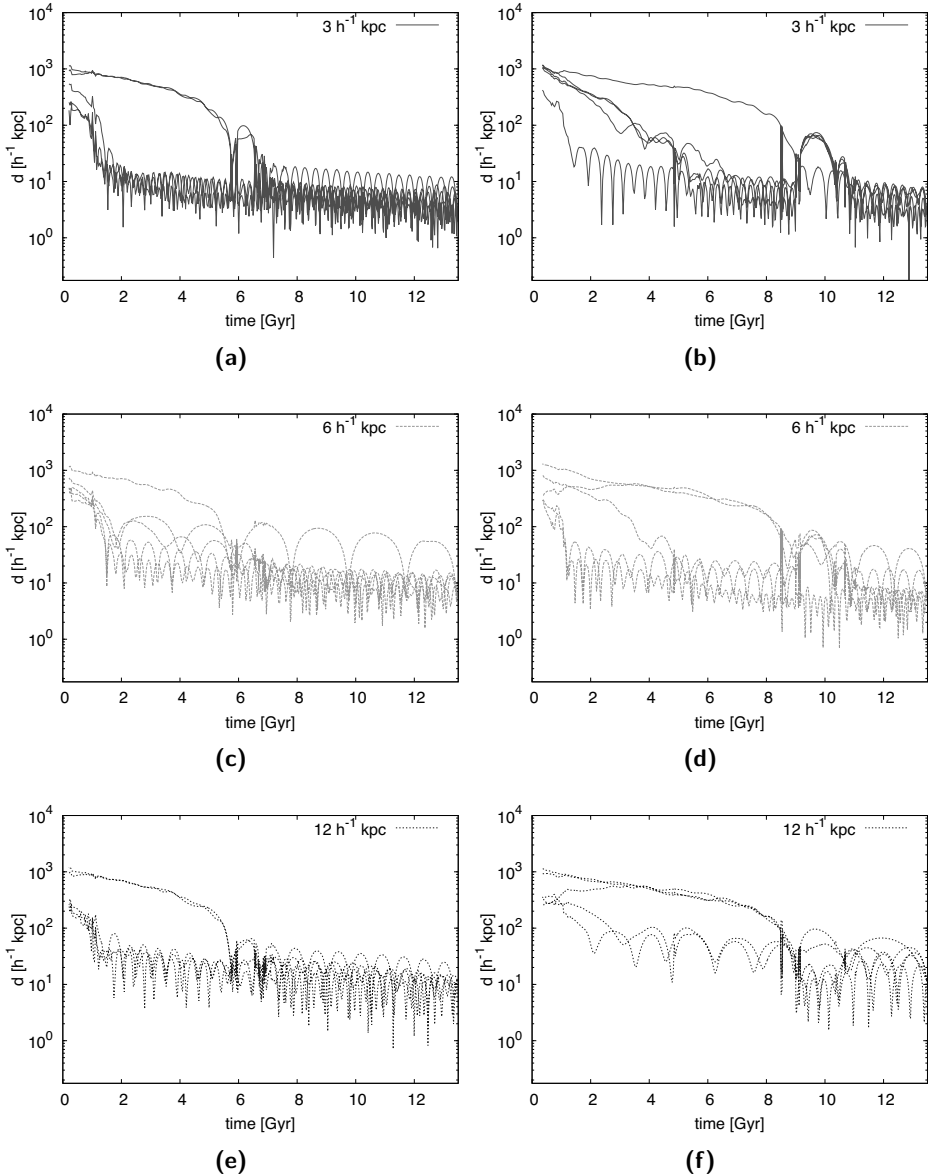


**Figure 5.10:** Co-moving distance of the clusters to the main halo centre for clusters in halo A (left) and halo B (right). Top, middle and bottom figures show clusters selected at  $3$ ,  $6$  and  $12 h^{-1} \text{ kpc}$ , respectively. Merger events in both haloes are visible as particles fall towards the halo centre. The orbital periods of the clusters are clearly visible.



particles (i.e. the clusters) from halo A (left) and halo B (right). In the following paragraphs, we discuss the evolution of two clusters from each halo; one immigrant and one native cluster in more detail.

### The clusters in halo A

In Figure 5.11, we show the mass evolution, mass loss rate over intervals of 10 Myrs and tidal field strength for an immigrant cluster (nr. A6-1, left) and a native cluster (nr. A6-4, right). This halo experiences a major merger which starts at about 6 Gyr, at that time the immigrant cluster is also captured by the main halo. The merger lasts until about 8 Gyr (see also Figure 5.1). When the merger is finished, the tidal field strength  $\lambda_{\max}$  shows more frequent peaks, indicating it has a shorter orbital period than before the merger. However, there is little change in the mass-loss rate.

The native cluster of halo A experiences the same merger but was already member of the major halo. Its orbit becomes somewhat less eccentric after the merger, while its apocentric distance and orbital period decrease. The mass-loss rate from this cluster is mostly unaffected by the merger.

In Figure 5.13, we show the result of two star clusters (A12-1 and A12-4), both using the tidal tensor calculated from the evolving CosmoGrid halo and using a tidal tensor calculated from the static  $z = 0$  CosmoGrid halo. For the static halo case, we sampled the tensor using the orbital trajectory of the cluster around its parent halo. For the native cluster, the resulting mass evolution differs only marginally, while the immigrant cluster suffers considerably higher mass loss in the static halo case, especially around the time the halo merger takes place, when its orbit is erratic. The static halo is a good approximation for the native cluster, while it falls short for the immigrant cluster.

### The clusters in halo B

In Figure 5.14 we present the details of the evolution of an immigrant cluster (nr. B6-3, left) and a native cluster (nr. B6-2, right) of halo B. The immigrant cluster is captured during the major merger event that starts around  $t = 8$  Gyr. Different from the clusters in halo A, the orbital period of the cluster around the dark matter halo is hardly visible in the cluster's mass evolution (see Figure 5.14, left, top panel). Just before the merger (around  $t = 7$  Gyr) the mass-loss rate is slightly smaller than before or after the merger. This is caused by the distortion of the infalling halo of which this cluster is a member at that time. When the merger is completed the cluster mass-loss rate has resumed to be as high as before the merger (see Figure 5.14, left, second panel).

The native cluster becomes part of the main halo during its first major merger,

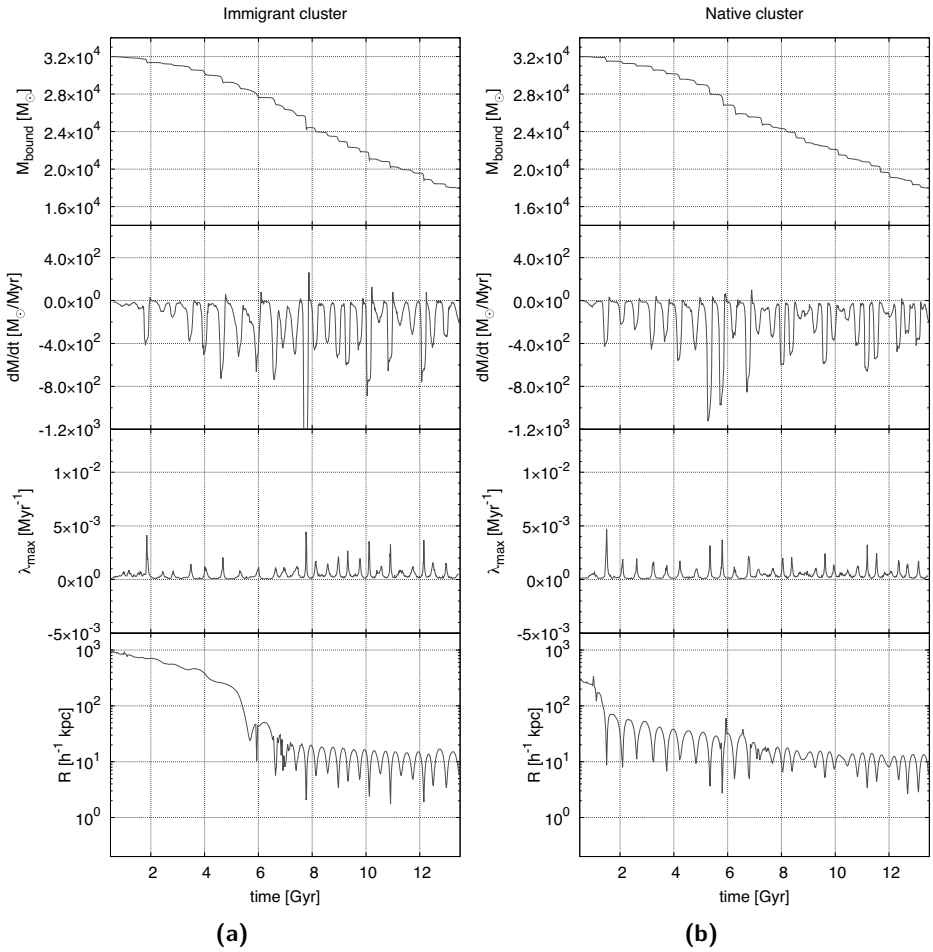


**Figure 5.11:** Evolution of two star clusters in orbit around halo A. To the left is a typical immigrant cluster identified with dark-matter particle nr A6-1 and to the right we present a native cluster, particle nr A6-4 (see also Table 5.2). From top to bottom the panels show the bound mass, the mass-loss rate, the strength of the tidal field ( $\lambda_{\max}$ ) and the co-moving distance of the cluster to the centre of the dark matter halo.

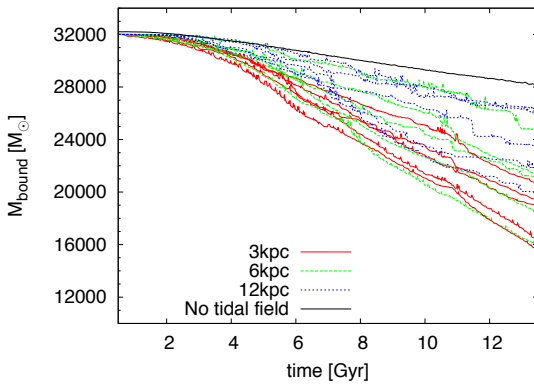
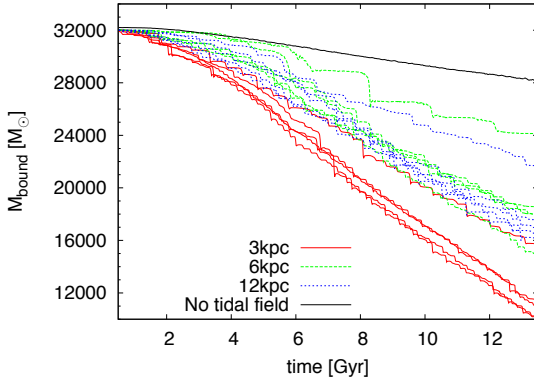


**Figure 5.12:** Bound mass in the simulated clusters for haloes A (top figure) and B (bottom figure). The red, solid; green, dashed and blue, dotted lines indicate clusters selected at 3, 6 and  $12 h^{-1} \text{kpc}$ , respectively. The black line indicates the mass of a cluster without an external tidal field.

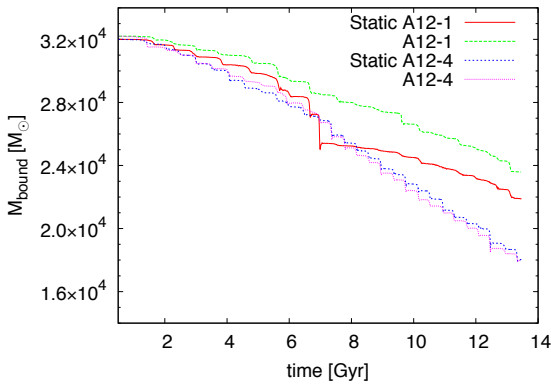


**Figure 5.13:** Evolution of two star clusters A12-1 (immigrant) and A12-4 (native). Both are simulated in an evolving halo as well as a static halo.

at around  $t = 5$  Gyr. After this merger, the tidal forces experienced by the cluster are stronger than before, visible in Figure 5.14 (right, third panel) as a sudden increase of  $\lambda_{\max}$  after  $t = 6$  Gyr. Its mass-loss rate is also increased, as can be seen from Figure 5.14 (right, second panel) and the difference in slope of  $M_{\text{bound}}(t)$  at  $t = 4$  Gyr and  $t = 8$  Gyr. The second major merger event leads to a temporary reduction in mass-loss for the cluster (at around  $t = 10$  Gyr). After this second halo merger the orbital period is evidently visible in the mass evolution of the cluster.

## 5.4 Discussion and conclusions

We presented a method to simulate star clusters within a pre-calculated tidal field, using the AMUSE environment. As a proof of concept, we apply this method to calculate the mass loss rates for star clusters in two live  $\Lambda$ CDM haloes from the CosmoGrid simulation. Our method compares well to self-consistent simulations.

We find that the mass loss rate strongly depends on the cluster's orbital parameters around the halo centre, as well as the central mass of the halo. Also, tidal disruption due to the  $\Lambda$ CDM environment is weaker in haloes that experienced many mergers. Finally, we find that in a Milky Way-like halo, the contribution of the  $\Lambda$ CDM environment to  $\Delta M / M_{\text{init}}$  can be up to 0.6 for clusters with an initial mass of  $32\,000 M_{\odot}$ .

In this article, several effects have not been taken into account, most notably we used a dark matter-only simulation. In this section, we discuss the relevance of these effects and how we intend to address these shortcomings.

Since the CosmoGrid simulation is a dark matter-only simulation, we do not account for the effect of baryons. Because the formation of the large-scale environment is dominated by dark matter, the lack of baryons has little influence on the formation of the haloes. Star clusters however likely contain little or no dark matter (Baumgardt et al. 2010; Conroy et al. 2011).

Because our simulation lacks baryons, there is no indication where star clusters would have formed or ended up had they been formed in our cosmological environment. We therefore have to resort to our method of identifying tracer particles for the star clusters in the final snapshot. We selected particles based on their distance to the halo centre. However, it is very likely that globular clusters would have formed in more specific locations, and possibly followed paths quite different from the ones in our simulation. In a simulation that includes baryonic matter and star formation, it would be possible to detect locations and masses of star clusters as they form.

The difference between old and young clusters herein is large: old clusters (like

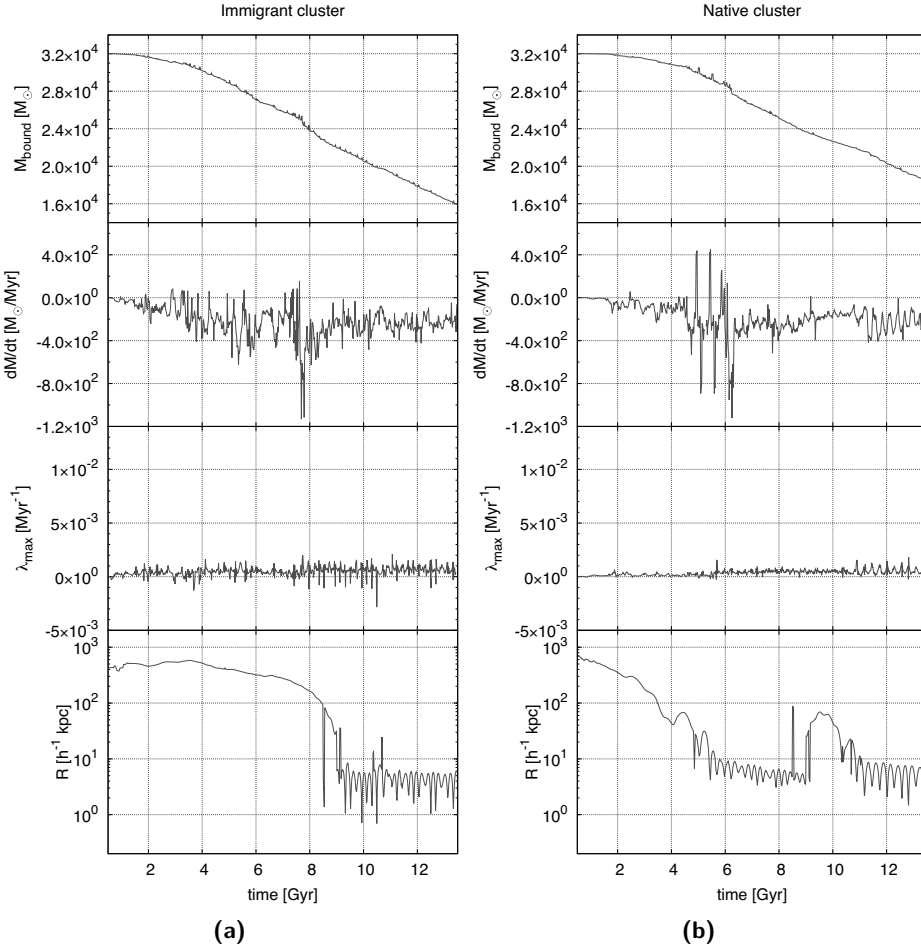


**Figure 5.14:** Evolution of two star clusters in orbit around halo B. To the left is a typical immigrant cluster identified with dark-matter particle nr B6-3 and to the right we present a native cluster, particle nr B6-2 (see also Table 5.2). From top to bottom the panels show the bound mass, the mass-loss rate, the strength of the tidal field ( $\lambda_{\max}$ ) and the co-moving distance of the cluster to the centre of the dark matter halo. Negative values of  $\lambda_{\max}$  correspond to times where the cluster is located inside a local (sub)concentration of matter. The spikes in the bottom panels for the immigrant and the native clusters is associated with a confusion in identifying the main parent in the halo finder.

the globular clusters in the Milky Way) formed before there was a Galactic disk, and remain relatively free of its influence. Young clusters however form in the galactic disk, and the tides experienced by these clusters are dominated by encounters with giant molecular clouds and spiral arms (Lamers and Gieles 2006; Gieles et al. 2007), the effect of which is about four times larger than the tidal field (e.g. Lamers and Gieles 2006, Figure 1). For this reason, we focus on old stellar clusters and initialize our simulated star clusters at an early epoch, before the galactic environment would have formed. In order to simulate young clusters, a galaxy simulation including baryons would be required. However, when the old clusters formed, the GMC density in the star-forming environment was likely very high, causing early disruption of low-mass globular clusters (Elmegreen 2010). This effect is not included in our simulations.

In order to investigate a large number of clusters with a reasonable amount of stars, we used the Barnes and Hut (1986) tree code *Bonsai* for most of our star cluster simulations. We compared the results for two distinct star clusters to similar simulations with the direct  $N$ -body code *ph4*. The results for both runs are similar for both codes, the direct code showing enhanced mass loss around the time of core collapse. However, the tree code fails to accurately describe the inner structure of the star cluster, and requires the distance between stars to be softened.

Another limit of our environment is its resolution. The spatial resolution of *CosmoGrid* is given by the softening length employed (175 parsec). Forces that occur on a scale similar to or smaller than this softening length are not accurately taken into account. Likewise, the mass resolution of dark matter particles in *CosmoGrid* is  $1.28 \times 10^5 M_{\odot}$ , about 4 times larger than the initial mass of our simulated clusters. The effects of tidal forces caused by a small dark matter object passing at close range to our clusters (such as a subhalo) are therefore limited, creating a possible bias against the effect of such structures. However, this resolution effect would be more important for baryons than it is for dark matter.

The benefit of using a large-scale cosmological simulation however, is that the formation of a dark-matter halo is followed. A simulation that only models a collision between galaxies would not take the earlier history and distribution of star clusters into account. In order to have the benefits of both a cosmological environment and high resolution, one could use re-simulation, where galaxies are simulated at high resolution within a lower-resolution environment.

Another limit imposed by our use of a pre-calculated simulation is its limited number of snapshots. We lack continuous information about the tidal tensor. In order to prevent sudden changes in the tidal field, we interpolate the tidal tensor between snapshots. However, it remains impossible to accurately track sudden changes in the tidal field on timescales shorter than our time resolution, such

as those occurring during halo mergers. Since the orbital periods of our clusters around the halo centre are larger than this time resolution, we do not expect this to have a large influence on the evolution of the tidal field. However, short-lasting passages of nearby objects may not be taken into account accurately, and a method in which the tidal field is sampled at more intervals remains preferable.

In a follow-up article (Rieder et al., in prep.), we will apply the method described in this article to the evolution of star clusters in the disk of a simulated Milky Way-type galaxy. In this follow-up, we will address several of the limitations discussed above, especially the lack of baryons and as a result the orbits and origins of the clusters.

## Acknowledgements

*It is our pleasure to thank the anonymous referee for very helpful suggestions and comments that greatly helped to improve the article. Also, we are grateful to Arjen van Elteren, Derek Groen, Inti Pelupessy, Jeroen Bédorf, Mark Gieles and Nathan de Vries for support, interesting discussions and useful suggestions.*

*This work was supported by NWO (grants IsFast [#643.000.803], VICI [#639.073.803], LGM [#612.071.503] and AMUSE [#614.061.608]), NCF (grants [#SH-095-08] and [#SH-187-10]), NOVA and the LKBF in the Netherlands, and by NSF grant AST-0708299 in the U.S. T.I. is financially supported by MEXT/HPCI STRATEGIC PROGRAM and MEXT/JSPS KAKENHI Grant Number 24740115. We thank the DEISA Consortium (EU FP6 project RI-031513 and FP7 project RI-222919) for support within the DEISA Extreme Computing Initiative (GBBP project).*

*The Cosmogrid simulations were partially carried out on Cray XT4 at Center for Computational Astrophysics, CfCA, of National Astronomical Observatory of Japan; Huygens at the Dutch National High Performance Computing and e-Science Support Center, SurfSARA (The Netherlands); HECToR at the Edinburgh Parallel Computing Center (United Kingdom) and Louhi at IT Center for Science in Espoo (Finland).*





## 6 | Evolution of star clusters in an evolving spiral galaxy

*Based on:*

*Steven Rieder, Robert Crain, Tom Theuns, Joop Schaye and Simon Portegies Zwart  
Evolution of star clusters in an evolving spiral galaxy  
In preparation*

In this chapter, we simulate open star clusters in a live galaxy. We utilize the tidal tensor approach described in chapter 5 to study the evolution and survivability of open clusters for various tidal fields representative for galactic open clusters. In the calculations, we include the effects of an initial cluster mass and radius distribution, a stellar initial mass function and stellar evolution, while the simulated galaxy has a potential representative for the Milky Way.

We simulate a set of 100 clusters in each of 30 different tidal fields, and compare the surviving distribution of clusters to the observed distribution of open clusters in the Milky Way.

## 6.1 Introduction

The stellar population of the galactic disk in the Milky Way is mostly comprised of field stars, while some stars reside in open clusters. However, most of these field stars were at one point not isolated: they used to be part of a cluster or a more extended association of stars (Portegies Zwart et al. 2010b; Lada and Lada 2003). Only a few stars remain bound to their birth cluster for more than a Gyr, most open clusters are disrupted within a few 100 Myr (e.g. Oort 1958; Kharchenko et al. 2005)

The mechanisms responsible for dispersing clusters and associations include stellar evolution, spiral arms, giant molecular clouds and a general galactic tidal field. Lamers and Gieles (2006) modelled the dissolution of open clusters, combining the effects of stellar evolution, tidal stripping, spiral arm shocks and GMC encounters using disruption rates found for these different disruption mechanisms in earlier studies, assuming a circular orbit around the galaxy at solar radius. They found a good agreement for cluster lifetimes between their cluster sample and observed clusters, with disruption of the clusters largely due to encounters with Giant Molecular Clouds (GMCs).

In this chapter, we use self-consistent simulations of star clusters in an evolving Milky Way-like galaxy to determine the lifetime and evolution of open clusters. We make use of a Milky Way-like galaxy re-simulation (originally selected from the large-scale Millennium run Springel et al. (2005)), which includes dark matter, gas and stars. The star particles in this simulation represent down to  $10^5 M_{\odot}$  in stellar matter, and contain information about their formation time, metallicity and location in each snapshot. We use these particles to trace the orbits of star clusters that would be born at such locations, giving us a realistic representation of the orbits star clusters would have in a Milky Way-type galaxy.

We calculate the tidal field in each snapshot at the location of these star particles, giving us a time-dependent tidal field for individual star clusters. With the Astrophysical Multipurpose Software Environment (AMUSE, Portegies Zwart et al. 2013), we combine these tidal fields to simulations of individual star clusters (including a stellar initial mass function and stellar evolution), giving us a self-consistent model for star clusters in the Milky Way.

We investigate the mass and radius distribution of clusters as they evolve, and compare the mass and radius distribution of surviving clusters to observations of open clusters in the solar neighbourhood. We distinguish clusters based on tidal field strength and orbital eccentricity, and investigate a possible signature of the tidal field strength in observable properties of the clusters.

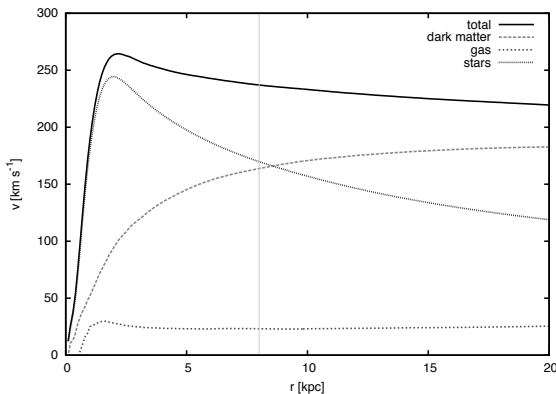


**Figure 6.1:** The rotation curve of the simulated galaxy employed in this chapter. The vertical line indicates the velocities at 8 kpc, the radius at which we select the star particles.

## 6.2 The experimental setup

### 6.2.1 The galaxy simulation

As a large-scale environment, we take a galaxy selected from re-simulated galaxies from the Millennium run (Springel et al. 2005). We selected this galaxy as a good example for a Milky Way-like galaxy, in that it has no major encounters after  $z = 1$  and has a stellar disk similar to that of the Milky Way. In Figure 6.1 we plot the galaxy's rotation curve, and in Figure 6.2 shows the distribution of gas in our simulated galaxy at  $z = 0$ .

The code used for the re-simulation is an evolution of the GIMIC and OWLS code, which reproduces many observable aspects of Milky Way-like galaxies at low redshift (eg Crain et al. 2009; Haas et al. 2012, and references therein). The simulation starts with only dark matter and gas particles. When a gas particle reaches a temperature and density required for star formation, it is converted to a star particle, with metallicity fixed at this point. Stellar winds, supernovae and other types of feedback incorporated in terms of subgrid physics gradually cause these star particles to lose mass to their surrounding gas particles, which are then enriched with metals formed in the stars.

We take a total of 900 snapshots during the galaxy simulation, with 23 Myr between snapshots near  $z = 0$ . This is sufficient time to account for orbits at the Solar orbital radius, with approximately 10 snapshots for each circular orbit between which we can interpolate. In each snapshot, the masses, positions and velocities of all the star, gas and dark matter particles are saved, as well as the metallicity, time of formation (when a gas particle is converted to a star particle), and mass at time of formation for the star particles.

From the final snapshot, we select all star particles and use these to calculate

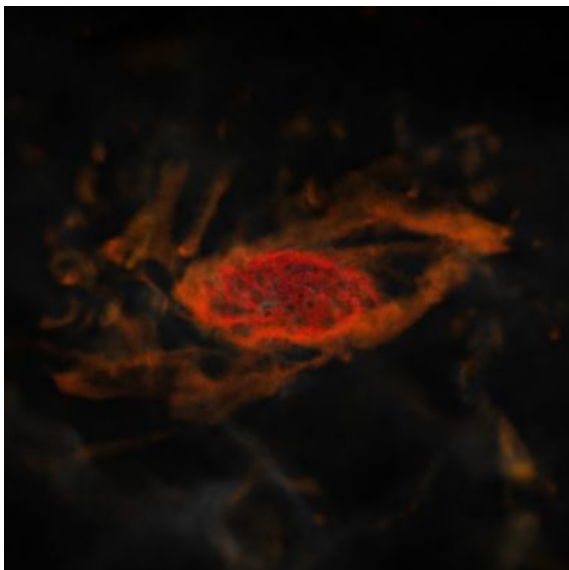


**Figure 6.2:** Image of gas in the galaxy used in our simulation at  $z = 0$ . Brightness and colour correspond to gas density and temperature, respectively.

the centre of the galaxy by taking the median of the positions. We calculate the orientation of the galactic stellar disk using the moment of inertia tensor. We then transform the positions of the star particles to galactic coordinates, and select all star particles with  $r = 8 \pm 0.5$  kpc and  $z = 0 \pm 0.5$  kpc. For each of these particles, we calculate the tidal tensor using the method described in Renaud et al. (2011) and chapter 5 with the gravity code `Fi` (Pelupessy 2005).

We now have fully time-dependent tidal fields for each of these star particles. These are representative for the tidal fields experienced by open clusters, but not for the stars expelled from these clusters. The initial mass of the star particles generally varies between  $2 \times 10^5 M_{\odot}$  and  $4 \times 10^5 M_{\odot}$ . This is higher than the mass of most open clusters, indicating that we cannot use their mass as a cluster mass function.

## 6.2.2 Star cluster models

We generate a set of initial conditions for cluster simulations. For these clusters, we use a Plummer (1911) model to spatially distribute stars. For the initial mass function of the stars, we select a Kroupa (2001) IMF, with a lower-mass cut-off at  $0.1 M_{\odot}$ . The average stellar mass varies between  $0.33$  and  $0.38 M_{\odot}$ , this scatter is due to run-to-run variations.

For the star clusters, we draw their initial masses from a Schechter (1976) distribution:

$$NdM \propto M^{-2} \exp(-M/M_{\star})dM, \quad (6.1)$$

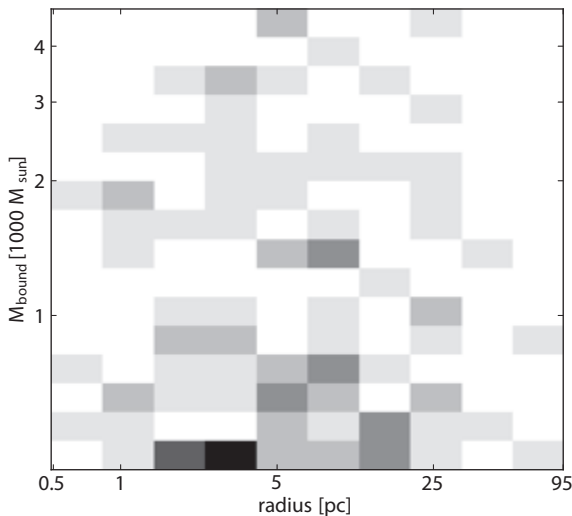


**Figure 6.3:** Density distribution of 100 randomly sampled clusters from a Schechter mass distribution and a lognormal radius distribution.

where  $M_* = 2 \times 10^5 M_\odot$ , which Larsen (2009) determined to be a good fit for young star clusters in spiral galaxies. For this initial investigation, we constrain our sample to those masses between  $5 \times 10^2 M_\odot$  and  $5 \times 10^3 M_\odot$ : lower mass clusters will quickly disperse, while higher mass clusters would take a much longer time to calculate. The minimum total mass for star clusters in our sample is  $500 M_\odot$ , the maximum is set to  $5000 M_\odot$ .

For the radius, we use a LogNormal distribution, with a mean of 5 pc and  $\sigma = 3$  pc. This is shown to be a good fit for young open clusters (van den Heuvel and Portegies Zwart 2013). We sample a total of 100 clusters from this distribution. This sample is limited to radii between 0.4 pc and 100 pc, again due to computational constraints. In Figure 6.3 we show the density distribution of clusters sampled this way.

### 6.2.3 Embedding star clusters in the galaxy

We use the AMUSE (Portegies Zwart et al. 2013) framework to simulate these clusters with the selected tidal fields. In AMUSE, many different codes for simulating gravity and stellar evolution are available. In order to investigate a large number of different clusters, we use the fast GPU-enabled tree code Bonsai (Bédorf et al. 2012) for gravity, in combination with the SeBa code (Portegies Zwart and Verbunt 1996; Toonen et al. 2012) for stellar evolution. We previously (see Figure 5.7) determined that the Bonsai code is indeed suitable for star cluster calculations, despite being a tree code. We use the mechanism described in chapter 5 to simulate the clusters within a time-dependent tidal field.

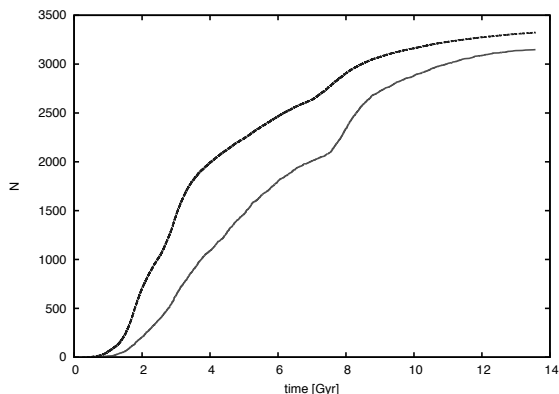


**Figure 6.4:** Star formation times for each of the star particles selected in our sample (solid) and for all the stars in our galaxy, lowered by 2 dex (dashed).

From our region of interest in the galaxy, we obtained 3150 star particles. In Figure 6.4, we plot the formation time for these particles. Since observed clusters only live for up to one Gyr, we select those particles that formed within a slightly longer period than that, up to 1.2 Gyr, to investigate in this chapter. For each of these star particles, we calculate the time-dependent tidal tensor, and simulate the previously generated set of 100 star clusters with this tensor.

At each step in the simulation, we check if the cluster still survives, i.e. more than 10% of the initial number of stars is still bound to the cluster. We stop the simulation at  $z = 0$ , or if the cluster is disrupted. If the cluster survives until  $z = 0$ , we save the positions, velocities and other properties of the stars in order to investigate these further.

## 6.3 Results

### 6.3.1 Tidal fields

We investigate all tidal fields formed in the last 1.5 Gyr of the simulation. In these fields, we distinguish three components: the dark matter, stars and gas. In Figure 6.5, we display two representatives of these tidal fields.

The tidal field is dominated by the stellar component, while the role of dark matter is almost equally important. The gas component is significantly less pronounced. This behaviour is as expected from the relative contributions of each fraction to the total enclosed mass, as can be inferred from Figure 6.1.

We find that the strength of the tidal field - measured as the largest component of its eigenvalues  $\lambda_{\max}$  - varies between  $0.0006 \text{ Myr}^{-2}$  and  $0.0084 \text{ Myr}^{-2}$ . Variations over time in the individual tidal fields are clearly visible, and are due to various causes, such as the eccentricity of the orbit, passages through the stellar

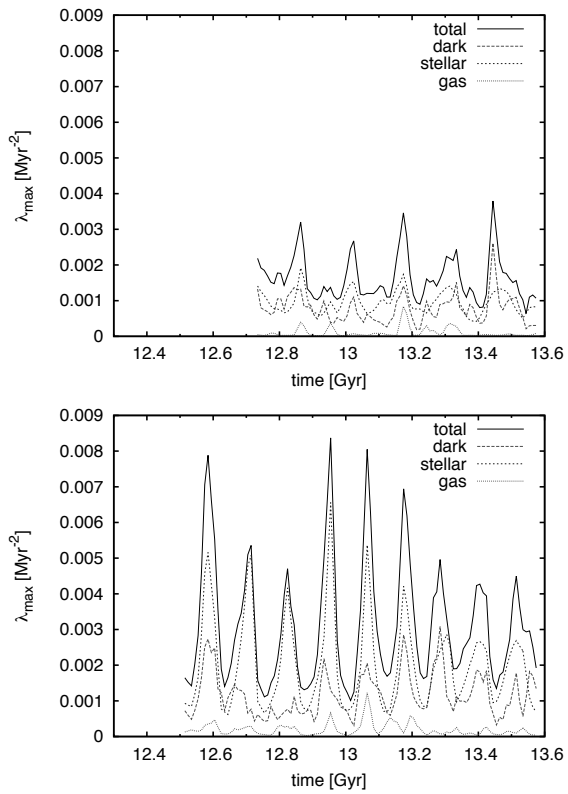


**Figure 6.5:** Strength ( $\lambda_{\max}$ ) of two tidal fields, 24 (top) as a representative weak tidal field and 33 (bottom) as a representative strong tidal field. The contributions of the three components (dark matter, stars and gas) are indicated.

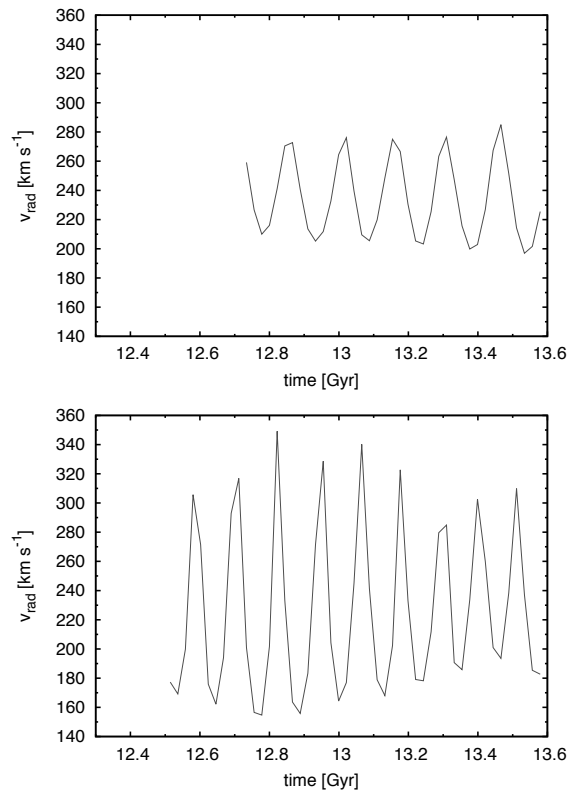


**Figure 6.6:** Orbital (circular) velocities of two clusters, 24 (top) and 33 (bottom).



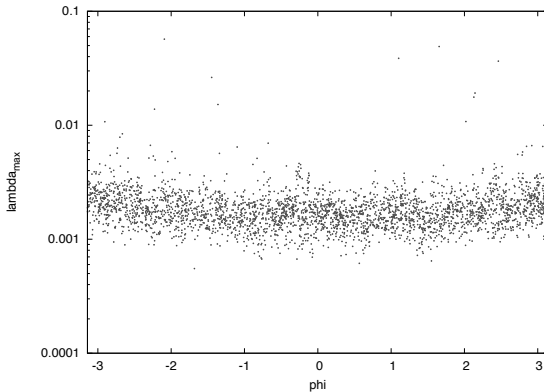


**Figure 6.7:** Distribution of tidal field strengths for clusters with different orbital phases at  $z = 0$ .

disk and encounters with locally enhanced densities. While in most tidal fields the difference between peaks and valleys is about a factor 2-3, in some extreme cases the difference can be a factor 9. In such cases (such as tidal field 30, see Table 6.1), a strong correlation is visible between the tidal field strength and the radial velocity of the cluster (see Figure 6.6), e.g. the eccentricity of the orbit.

The orbital periods of the clusters is most clearly visible in the stellar component, which shows one peak per orbit around the galactic centre. In the gas and dark matter components, this periodicity is far less pronounced.

For each of the clusters, we calculate the instantaneous Kepler orbital parameters: the eccentricity and the semi-major axis of the orbit. We find that the clusters with the strongest variations in the tidal field are those on the most eccentric orbits. In Table 6.1 we show the orbital parameters and tidal field strengths for each of the tidal fields studied in this chapter.

In Figure 6.7, we plot the field strength  $\lambda_{\max}$  against the orbital phase  $\phi$  in the final snapshot. We find that the tidal fields have a mean value of  $0.00196 \text{ Myr}^{-2}$  with a standard deviation  $\sigma = 0.00187 \text{ Myr}^{-2}$ .

### 6.3.2 Cluster evolution

We simulate clusters with each of the tidal fields investigated in the previous section. For each of the clusters simulated this way, we track the half-mass radii and the bound masses over their lifetimes.

We find that all clusters with a lifetime  $> 1.1 \text{ Gyr}$  are destroyed at  $z = 0$ . The rate at which clusters lose mass varies, dependent on the strength of the individual tidal fields and their initial compactness. Clusters that are initially more extended than  $10 \text{ pc}$  are destroyed within  $100 \text{ Myr}$ . The influence of peaks in the tidal field is visible, although these variations are largely smoothed out over a cluster's lifetime.

**Table 6.1:** Properties for the individual tidal fields investigated in this chapter.

ID	$Z$	$t_{\text{start}}$ Myr	$r(z=0)$ kpc	$e$	$a$ kpc	$p$ Myr	$\lambda_{\text{max}}(\text{min})$ $\text{Myr}^{-2}$	$\lambda_{\text{max}}(\text{max})$ $\text{Myr}^{-2}$	$\langle \lambda_{\text{max}} \rangle$ $\text{Myr}^{-2}$
02	0.022	13526.3	7.707	0.116	6.971	171.3	0.00230	0.00270	0.00244
03	0.014	13489.7	7.642	0.770	5.800	130.4	0.00148	0.00785	0.00436
04	0.020	13344.6	8.139	0.065	8.704	233.5	0.00066	0.00284	0.00136
05	0.035	13276.2	7.868	0.035	7.976	207.8	0.00107	0.00292	0.00201
06	0.026	13267.8	7.783	0.114	8.724	238.8	0.00098	0.00335	0.00183
07	0.045	13244.2	8.379	0.071	8.482	221.9	0.00124	0.00278	0.00189
08	0.048	13205.5	8.376	0.288	6.506	149.1	0.00100	0.00431	0.00237
09	0.024	13182.9	7.526	0.156	8.419	229.6	0.00183	0.00358	0.00269
10	0.017	13101.6	8.384	0.128	7.507	184.7	0.00103	0.00372	0.00202
11	0.029	12994.0	7.601	0.167	6.767	164.8	0.00137	0.00352	0.00242
12	0.008	12952.9	7.997	0.037	8.096	211.1	0.00074	0.00485	0.00218
13	0.015	12929.0	7.939	0.299	7.257	179.7	0.00144	0.00463	0.00298
14	0.045	12922.2	7.841	0.062	7.910	205.6	0.00141	0.00375	0.00243
15	0.022	12915.9	8.437	0.281	7.317	177.3	0.00059	0.00372	0.00155
16	0.006	12884.6	8.007	0.108	8.889	242.7	0.00075	0.00311	0.00164
17	0.022	12847.4	8.307	0.064	7.945	201.9	0.00113	0.00307	0.00206
18	0.046	12837.7	8.384	0.238	8.879	237.6	0.00071	0.00276	0.00157
19	0.023	12768.0	8.180	0.150	7.207	175.6	0.00106	0.00347	0.00192
20	0.018	12762.7	7.982	0.129	7.692	195.6	0.00142	0.00357	0.00221
21	0.023	12746.7	7.643	0.131	8.296	223.1	0.00108	0.00471	0.00204
22	0.026	12736.1	8.003	0.162	9.515	268.8	0.00079	0.00315	0.00142
23	0.037	12720.1	8.463	0.113	8.481	221.0	0.00079	0.00394	0.00186
24	0.004	12719.6	8.282	0.125	8.139	209.7	0.00064	0.00379	0.00163
25	0.049	12719.6	7.670	0.034	7.896	206.9	0.00174	0.00414	0.00281
26	0.028	12707.1	7.672	0.309	5.876	132.8	0.00165	0.00520	0.00330
27	0.050	12695.5	8.018	0.144	7.639	193.2	0.00120	0.00349	0.00202
28	0.027	12610.2	8.362	0.178	10.167	291.5	0.00120	0.00303	0.00182
29	0.036	12578.9	7.591	0.220	9.730	284.2	0.00130	0.00451	0.00241
30	0.022	12563.1	8.357	0.223	6.937	164.3	0.00076	0.00271	0.00164
31	0.030	12563.1	7.688	0.025	7.501	191.4	0.00137	0.00454	0.00273
32	0.035	12523.2	8.320	0.088	8.437	220.8	0.00103	0.00345	0.00203
33	0.026	12509.3	8.311	0.393	5.995	132.3	0.00101	0.00837	0.00314
34	0.024	12506.0	7.600	0.062	7.696	199.8	0.00093	0.00330	0.00199
35	0.010	12434.1	8.086	0.585	5.453	116.1	0.00081	0.00721	0.00331
36	0.010	12334.3	7.816	0.049	8.102	213.4	0.00100	0.00438	0.00236
37	0.028	12324.1	8.247	0.584	5.866	128.5	0.00065	0.00840	0.00296
38	0.053	12323.8	7.640	0.122	8.552	233.6	0.00087	0.00318	0.00178
39	0.029	12313.8	7.722	0.139	8.900	246.9	0.00081	0.00443	0.00189
40	0.006	12303.4	7.580	0.126	6.754	164.5	0.00108	0.00340	0.00220

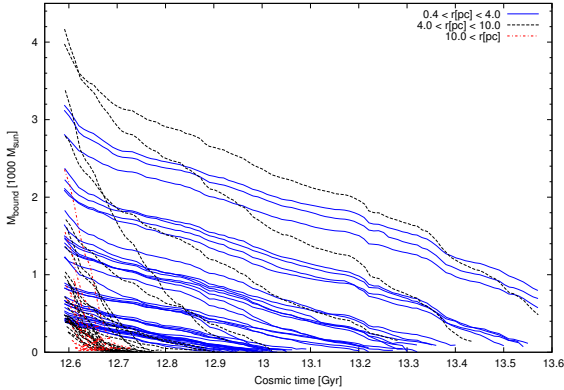


**Figure 6.8:** Mass evolution of clusters in tidal field 30.

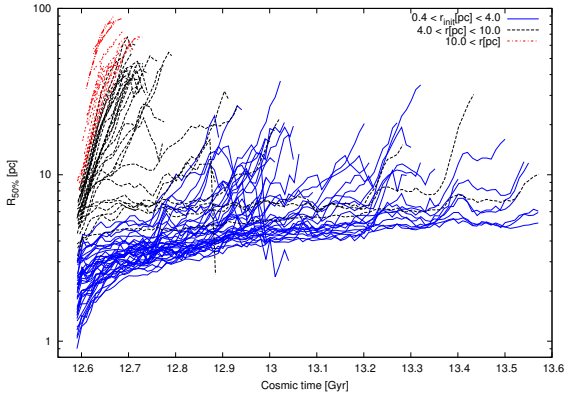


**Figure 6.9:** Half-mass radius evolution of clusters in tidal field 30.

Since the more extended clusters are quickly destroyed, the radius distribution of the clusters soon converges to smaller radii. In fact, as early as 200 Myr after the clusters are born, we see a half-mass radius distribution that has a peak between 4–5 pc, regardless of the tidal field. Clusters with an initially more compact radius gradually move towards this radius, while clusters with a half-mass radius larger than 7 pc are destroyed within 100 Myr (as seen in Figures 6.8 and 6.9 for tidal field 30, as an example).

### 6.3.3 Comparison to observed open clusters

In Figure 6.10, we plot the mass vs age distribution of surviving clusters, normalized to the number of clusters in the initial distribution. Each age bin represents an individual tidal field, each of which contains 100 clusters initially. In the same figure, we overplot the masses and ages of observed clusters, using the open cluster catalog data from Lamers et al. (2005); Kharchenko et al. (2005). The masses of

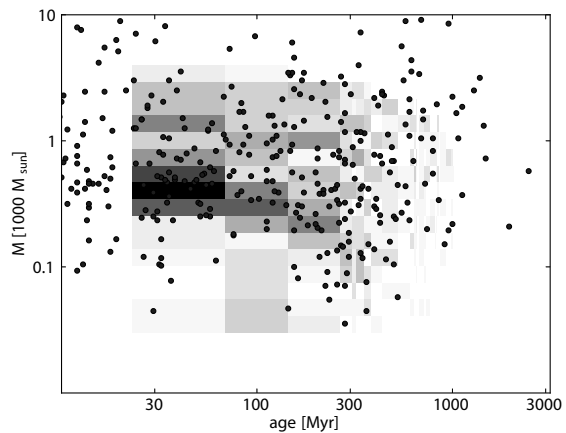


**Figure 6.10:** Distribution of simulated clusters surviving until  $z = 0$  (background, greyscale) with observed clusters from Lamers et al. (2005); Kharchenko et al. (2005) overlotted.

these observed clusters were obtained by fitting a Salpeter mass function with a lower limit of  $0.15 M_{\odot}$  to all observed stars.

Both the simulated and the observed distribution show a lack of clusters older than  $\approx 1$  Gyr, which was earlier identified as the "Oort problem". Also, both distributions show a peak in mass around  $500 M_{\odot}$  at young age, which declines with age.

The initial population of simulated clusters has a cutoff on the high end of the mass distribution at  $> 5000 M_{\odot}$ , as a result the simulated cluster distribution shows a dearth of higher-mass clusters especially at later ages.

#### 6.3.4 Influence of eccentricity on cluster properties

In Table 6.2 we show the masses, ages and radii for surviving clusters, divided into four categories based on their final mass and the eccentricity of their orbit in the galaxy. We find that clusters on orbits with high eccentricity show a larger half-mass radius than those clusters on more circular orbits. This may be a result of the more strongly varying tidal field experienced by these clusters. The low-mass clusters also show a larger half-mass radius than the high-mass sample. This is likely a result of nearly-disrupted clusters being included in this sample.

For clusters with equal mass, we find a higher age in the low-eccentricity cases than in high-eccentricity cases. This is a result of the stronger tidal field, and therefore mass loss, experienced by the latter group.

#### 6.3.5 White dwarfs as a signature for tidal field strength

In the initial phase of our star clusters, masses selected from a Kroupa (2001) mass function are assigned randomly to stars. In evolved clusters however, mass segrega-

**Table 6.2:** Properties of surviving simulated clusters, for clusters with high ( $> 0.129$ ) and low eccentricity, and high ( $> 458 M_{\odot}$ ) and low mass.

	N	$\langle M \rangle$ $M_{\odot}$	$\sigma M$ $M_{\odot}$	$\langle \text{age} \rangle$ Myr	$\sigma \text{ age}$ Myr	$r$ pc	$\sigma r$ pc
Low e, low mass	139	190	130	380	170	7.7	5.2
Low e, high mass	126	1190	590	430	210	4.9	1.9
High e, low mass	133	200	130	270	270	15.5	17.2
High e, high mass	147	1150	670	360	330	5.9	8.9

**Table 6.3:** Properties of two clusters of similar mass and radius at  $z = 0$ .

Cluster	Tidal field	$M_{\text{bound}}$ $M_{\odot}$	$R_{50\%}$ pc	$N_{\text{WD}}$
C004	T14	1253	4.8	54
C027	T15	1227	4.3	29

tion has been observed (e.g. Brandl et al. 1996; de Grijs et al. 2002), where massive stars have preferentially migrated towards the core. Since a tidal field preferentially removes stars from the outer parts of the cluster, over time tidal disruption in combination with mass segregation will increase the average stellar mass in the cluster.

In the case where the tidal field is initially weak, mass segregation can take place before a significant number of stars is stripped from the cluster, allowing these stars to be preferentially low-mass. In a strong tidal field however, mass stripping will occur before mass segregation. In such a cluster, higher-mass stars would be stripped as well, leading to a different fraction of high-mass stars in the cluster.

At a later age, this difference may translate into a different fraction of stellar remnants such as white dwarfs in the cluster. In order to test this scenario, we select two clusters from two tidal fields that differ in strength, but little in age (tidal fields 14 and 15, see Table 6.1), to investigate in more detail. These clusters originate from different masses, yet show similar characteristics ( $M_{\text{bound}}$ ,  $R_{50\%}$ , see Table 6.3) at  $z = 0$ . However, the number of white dwarfs within  $R_{50\%}$  is much higher in cluster 004. In order to test our hypothesis that this difference is a signature of the different strength of the tidal field, we re-simulate both these clusters for 130 different realizations of the initial random seed, and compare the characteristics.

In Table 6.4, we show the results of these new realizations. We count the number of white dwarf stars within  $R_{50\%}$  for each of these realisations, and show the average and standard deviation of this number. We find that the cluster that experienced the weaker tidal field, C027, now contains a slightly larger number of

**Figure 6.11:** Mass evolution of the 130 times re-simulated clusters T14 C004 and T15 C027. Solid lines represent the averaged value, dashed lines represent the  $1\sigma$  variation.

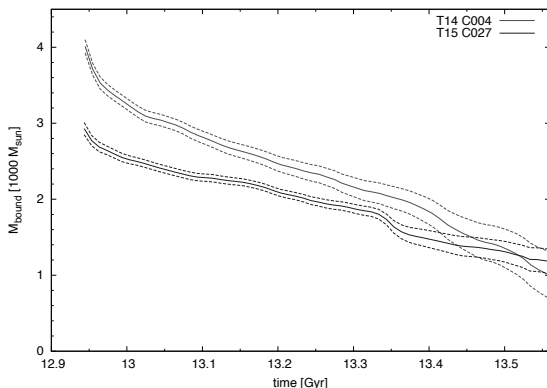


**Table 6.4:** Properties of 130 re-simulated clusters.

Cluster	Tidal field	$N_{\text{surv}}$	$M_{\text{bound}}$ $M_{\odot}$	$R_{50\%}$ pc	$N_{\text{WD}}$	$N_{\text{WD}}/M_{\text{bound}}$ $1/M_{\odot}$
C004	T14	128	$930 \pm 310$	$4.7 \pm 0.5$	$34.2 \pm 14.4$	0.037
C027	T15	130	$1130 \pm 170$	$4.4 \pm 0.5$	$42.6 \pm 9.6$	0.038

white dwarf stars at  $z = 0$ . However, when we count the number of white dwarfs per mass unit, this difference disappears. Based on these simulations, we find no evidence of the tidal field strength based on the number of white dwarfs.

## 6.4 Discussion and conclusions

We used a self-consistent model to simulate star clusters in a Milky Way-type galaxy. The clusters simulated in this way are disrupted in the first 1.1 Gyr, a result that is in agreement with observations and earlier studies.

## Acknowledgements

*We are grateful to Arjen van Elteren, Inti Pelupessy and Nathan de Vries, for their assistance with and work on AMUSE. Likewise, we are grateful to Jeroen Bédorf for his work on Bonsai. Furthermore, we would like to express our gratitude to Henny Lamers for useful discussions and assistance with observed cluster data, and to Nate Bastian and Mark Gieles for useful and interesting discussions*

# 7 | Samenvatting

## 7.1 Afstanden in het heelal

De meeste mensen, zeker in Nederland, wonen in steden. Ons dagelijks leven speelt zich dan ook af binnen enkele kilometers. Wanneer we een andere stad bezoeken bevindt zich deze meestal nog wel binnen enkele honderden kilometers. Als we op een verre reis gaan, wordt dat enkele duizenden kilometers. Een reis van Nederland naar Australië is zo'n 15.000 kilometer, voor menselijke begrippen een enorme afstand. De ruimtevaarders die de maan bezocht hebben, hebben daarvoor een nog veel grotere afstand afgelegd, ongeveer 380.000 kilometer heen en terug. Deze afstand is zo groot, dat licht er meer dan twee seconden over doet om heen en weer te gaan.

Dit proefschrift gaat voornamelijk over melkwegstelsels en sterrenhopen. De onderlinge afstanden hiertussen zijn van een volstrekt andere orde. Afstanden tussen sterren onderling worden gemeten in lichtjaren (de afstand die het licht in één jaar aflegt, zo'n 9.5 biljoen kilometer<sup>1</sup>, of in parsecs<sup>2</sup>. Om enigszins een idee te geven van deze afstanden heb ik ze geprobeerd te vertalen naar menselijke afstanden, waarbij ik onze melkweg de grootte van een stad als Leiden heb gegeven (zie tabel 7.1).

**Tabel 7.1:** Kosmische afstanden

grootte van:	in lichtjaar	in kkm <sup>3</sup>	vergelijkbaar met:
diameter melkweg	100.000	6	Leiden
afstand tot Andromeda	2.500.000	150	Leiden - Zwolle
afstand tot de Virgo cluster	50.000.000	3000	Leiden - Ankara
grootte van CosmoGrid	100.000.000	6000	Leiden - Novosibirsk
afstand verst bekende melkweg	12.500.000.000	750.000	Aarde - Maan en terug

<sup>1</sup>9.500.000.000.000 km

<sup>2</sup>1 parsec is ongeveer 3 lichtjaar

Onze melkweg ziet er ongeveer uit als een pannekoek met spiraalarmen en een bult in het midden (plaatje 7.1). Hij heeft een diameter van ongeveer 100.000 lichtjaar. Onze naaste buur van vergelijkbare grootte, het Andromedastelsel, staat op ongeveer 2,5 miljoen lichtjaar afstand.

Het heelal is onmetelijk groot. Het licht van het melkwegstelsel dat momenteel de recordhouder is van "verste melkweg" doet er zelfs 12,5 miljard jaar over om bij ons te komen, dat is bijna net zo lang als het heelal oud is.

Omdat het heelal zo groot is vergeleken met onze dagelijkse afstanden, zijn ook de tijdschalen van een andere orde. Tijdens een mensenleven kun je slechts af en toe kleine veranderingen zien in melkwegstelsels, zoals variaties in helderheden van sterren, en heel af en toe een ster die als supernova explodeert. Voor het overige lijkt het heelal stil te staan.

Toch weten we dat het heelal volop in ontwikkeling is. Melkwegstelsels ondergaan continu interacties met hun burens, dit leidt tot botsingen en het smelten tot grotere melkwegen. De sponsstructuur die we in het heelal zien (zie plaatje 7.2) is ontstaan uit een oorspronkelijk veel gelijkere verdeling van materie, die op den duur is gaan samenklonteren.

Omdat de tijdschaal waarop dit gebeurt in de orde van miljarden jaren ligt, kunnen we de verschillende ontwikkelingen die melkwegen ondergaan niet achtereenvolgens zien. We zien wel melkwegen in verschillende stadia van ontwikkeling, omdat licht van ver ook van lang terug komt. Maar om de ontwikkeling van een enkel melkwegstelsel te volgen moeten we deze proberen na te bootsen door middel van computersimulaties.

In dit proefschrift beschrijf ik een methode om een zo nauwkeurig mogelijke simulatie van een stukje heelal uit te voeren, en vervolgens enkele van de resultaten die deze simulatie heeft opgeleverd.

## 7.2 Samenstelling van het heelal

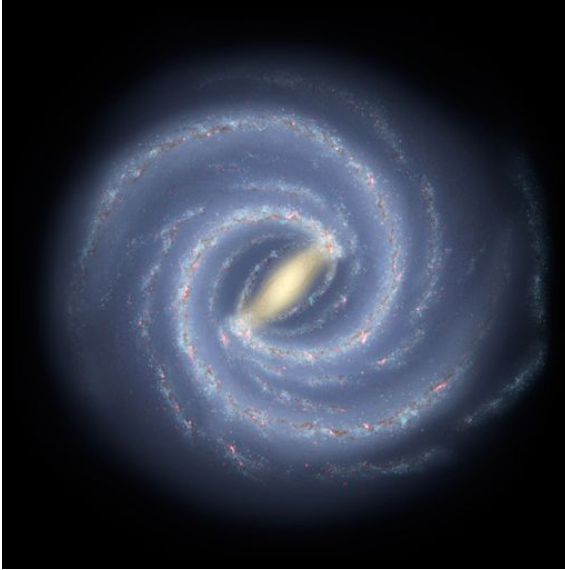
Volgens de meest recente metingen aan de samenstelling van het heelal, door de Planck satelliet, bestaat de energiedichtheid van het heelal voor 5 procent uit "normale" materie (zoals gas, sterren en planeten; maar ook zwarte gaten), 27 procent donkere materie en 68 procent donkere energie. Donkere energie is er verantwoordelijk voor dat het heelal steeds sneller uitdijt, donkere materie en gewone materie klonteren door hun zwaartekracht samen in respectievelijk halo's en melkwegen.

De grootschalige structuur in het heelal ontstaat dus voornamelijk door materie en energie die we niet direct kunnen zien. Indirect kunnen we donkere materie

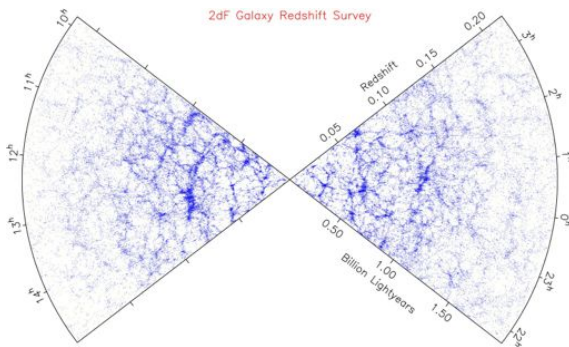
---

<sup>3</sup>kosmische kilometers





**Figuur 7.1:** Conceptbeeld van ons melkwegstelsel (NASA/JPL-Caltech/ESO/R. Hurt).



**Figuur 7.2:** De sponsstructuur in het heelal, zichtbaar in de verdeling van melkwegstelsels. Beeld van de 2dF Galaxy Redshift Survey.

wel meten, door de zwaartekracht die deze uitoefent. Als we bijvoorbeeld de snelheden van sterren in een melkwegstelsel meten kunnen we er achter komen hoeveel massa voor deze snelheden nodig is. Door deze hoeveelheid massa te vergelijken met de zichtbare hoeveelheid weten we ongeveer hoeveel donkere materie er in melkwegstelsels zit.

### 7.3 Simulaties

Doordat donkere materie grotendeels verantwoordelijk is voor de structuur van het heelal moet een simulatie van het heelal dus voornamelijk donkere materie bevatten. Gelukkig is donkere materie goed na te bootsen: het reageert (vrijwel) alleen via de zwaartekracht, en die is alleen afhankelijk van de afstanden tussen deeltjes en hun massa.

De eenvoudigste manier om het heelal na te bootsen is door een grote kubus te nemen, in deze kubus een grote hoeveelheid deeltjes te verspreiden (op een manier vergelijkbaar met het begin van het heelal) en hier zwaartekracht op te laten werken. Donkere energie speelt hierbij ook een rol: deze zorgt ervoor dat naarmate de simulatie vordert alle afstanden steeds groter worden. Om te zorgen dat niet alle deeltjes naar het midden worden getrokken zijn zulke kubussen periodiek: een deeltje wat aan de linkerkant de kubus uitgaat komt aan de rechterkant weer binnen.

Om zo gedetailleerd mogelijk te kunnen volgen hoe structuur in het heelal ontstaat, zijn veel deeltjes nodig: hoe meer hoe beter. Ook de grootte van de kubus is van belang: een grote kubus geeft meer informatie over grote structuren, maar dit gaat ten koste van de hoeveelheid detail. Er worden dan ook veel verschillende simulaties gedaan, om zo veel mogelijk schalen te kunnen onderzoeken. Een van de meest gebruikte simulaties van de afgelopen jaren is de Millennium simulatie, deze besloeg een kubus met zijden van 1.500 miljoen lichtjaar. Elk deeltje in deze simulatie had een massa vergelijkbaar met die van 1 miljard zonnen. Ter vergelijking: onze melkweg zou in die simulatie uit ongeveer 1.000 deeltjes bestaan, nauwelijks genoeg om enige details te kunnen onderzoeken.

Om toch ook naar details van stelsels vergelijkbaar met de melkweg te kunnen kijken wordt vaak gebruik gemaakt van *re-simulaties*. Hierbij wordt in eerste instantie gebruik gemaakt van een simulatie zoals Millennium, waarin de interessante gebieden gemarkeerd worden. Deze gebieden worden daarna nogmaals gesimuleerd, maar nu met veel meer deeltjes van kleinere massa. Zo hoef je niet de hele simulatie met hoge resolutie uit te voeren, wat veel meer computerkracht zou kosten. Een nadeel van deze methode is wel dat je eerst al op zoek moet gaan naar de interessante gebieden in de simulatie met lagere resolutie.

De CosmoGrid simulatie die ik in dit proefschrift gebruik is er juist een die een klein volume beschrijft, met "slechts" 100 miljoen lichtjaar per zijde. Elk deeltje stelt hierin 10.000 zonsmassa's voor, klein genoeg om details van halo's ter grootte van kleine dwergstelsels te kunnen vinden. Omdat een klein volume relatief meer computerkracht dan een groot volume kost, was het uitvoeren van CosmoGrid een zware taak.

## 7.4 De hoofdstukken in dit proefschrift

### 7.4.1 Simulaties op gecombineerde supercomputers

Om simulaties met zo veel mogelijk deeltjes (zoals CosmoGrid) uit te kunnen voeren, is dus veel computerkracht nodig. Hoewel de supercomputers die er zijn steeds groter en sneller worden, kan het ook nuttig zijn om gebruik te maken van zo veel mogelijk supercomputers tegelijk, om zo meer computerkracht te krijgen. Voor CosmoGrid hebben we deze methode toegepast. In hoofdstuk 2 testen we deze methode, om te kijken of deze ook nog efficiënt blijft ten opzichte van een simulatie op één supercomputer. We gebruiken hiervoor een combinatie van drie supercomputers (in Nederland, Schotland en Finland).

De zwaartekrachtcode die we hiervoor gebruiken testen we op verschillende (combinaties van) systemen, waarbij we de snelheid op één locatie als basis nemen. Wanneer we alle drie de supercomputers gekoppeld gebruiken met een gecombineerde rekenkracht gelijk aan die op één locatie halen we 90% van de oorspronkelijke tijd, 10% van de tijd gaat dus verloren door communicatie tussen de verschillende computers. Wanneer we een simulatie zouden uitvoeren met een grotere hoeveelheid deeltjes gaat dit percentage nog verder omlaag, zodat op dat moment nog meer computers tegelijk gebruikt zouden kunnen worden. De methode is dus geschikt om dit soort simulaties uit te voeren, wanneer inderdaad meerdere supercomputers tegelijkertijd beschikbaar zijn.

### 7.4.2 De CosmoGrid simulatie

In hoofdstuk 3 beschrijven we de CosmoGrid simulatie. Deze simulatie is specifiek geschikt om structuur ter grootte van dwergstelsels tot de lokale groep te onderzoeken. We onderzoeken in hoeverre de CosmoGrid simulatie overeenkomt met eerder gepubliceerde modellen en simulaties voeren we een serie tests uit om te controleren tot welk detailniveau de simulatie betrouwbaar is.

Ook onderzoeken we de hoeveelheid satellithalo's die de halo's van verschillende massa hebben. We vinden een verband tussen de hoeveelheid massa van een halo en de hoeveelheid subhalo's (groter dan een bepaalde massafractie) die deze

halo bij zich heeft. Echter, vanwege de beperkte grootte van het CosmoGrid volume is deze hoeveelheid voor grotere halo's enigszins onzeker. Om dit beter te kunnen bestuderen zou een groter volume met vergelijkbare massaresolutie nodig zijn.

### 7.4.3 Ontstaan van sliertige melkwegen in leegtes

Het heelal ziet er op grote schaal uit als een soort spons. Er komen gebieden voor waar veel melkwegstelsels op een kluitje zitten, maar er zijn ook grote leegtes, zogenaamde `voids': lege holten tussen dichte clusters, afgeplatte wanden en uitgerekte filamenten. Hier zijn bijna geen sterrenstelsels te vinden. Toch hebben astronomen door middel van de ``Void galaxy survey" (zoektocht naar melkwegen in leegtes) ongeveer zestig zogenaamde kluizenaarsstelsels in deze leegtes gevonden. De meesten hiervan zijn in hun eentje, zonder nabije burens, maar het systeem ``VGS\_31" bestaat uit maar liefst drie melkwegstelsels vlak bij elkaar. Uit waarnemingen blijkt dat deze stelsels in dezelfde sliert waterstofgas zitten, en dat ze wellicht pas recent bij elkaar zijn gekomen. Een merkwaardig melkwegensysteem dus, waarvan het ontstaan een raadsel is.

In hoofdstuk 4 onderzoeken we door middel van de CosmoGrid simulatie hoe dit soort kluizenaarsystemen kunnen zijn ontstaan. De CosmoGrid simulatie geeft in zeer hoog detail het ontstaan van donkere materie halo's waarin melkwegen ontstaan weer. In deze simulatie bevinden zich acht systemen die in allerlei aspecten sterk op VGS\_31 lijken. Van deze systemen onderzoeken we de ontstaansgeschiedenis. Hierbij kijken we naar verschillende aspecten: de hoeveel interacties/botsingen die de halo's ondergaan, hoe de afstanden tussen de verschillende halo's veranderen en hoe de omgeving van de stelsels er uit ziet.

De gesimuleerde systemen zien er aan het eind wel hetzelfde uit, maar de ontstaansgeschiedenis is desondanks erg gevarieerd. Ongeveer de helft van de systemen ontstond pas heel recent door botsingen tussen kleine halo's, de andere helft vormde heel vroeg en onderging daarna nauwelijks nog enige interactie. VGS\_31 is in dit opzicht dus niet een typisch voorbeeld van melkwegen in leegtes.

Er zijn ook overeenkomsten tussen de verschillende systemen: de stelsels blijken zonder uitzondering deel uit te maken van een zeer dunne structuur van donkere materie in de leegte. Dit verklaart het feit dat de VGS\_31 stelsels in een vrijwel rechte lijn staan, en dit lijkt een typische eigenschap te zijn van melkwegen in leegtes. De stelsels zijn in feite achtergebleven, terwijl grotere melkwegen aan de rand van de leegte alle materie wegtrokken. Een andere typische eigenschap van dit soort systemen is dat de stelsels al heel lang bij elkaar in de buurt te vinden zijn, waarschijnlijk zijn de stelsels in VGS\_31 dus al hun hele leven lang burens.

#### 7.4.4 Evolutie van bolhopen in halo's van donkere materie

In melkwegstelsels zitten behalve losse sterren ook veel sterren in groepen of clusters, zogenaamde sterrenhopen. Sterren in zulke clusters ontstaan nagenoeg tegelijkertijd uit een grote wolk gas, en worden door hun onderlinge zwaartekracht bij elkaar gehouden. Ruwweg is er een onderscheid te maken tussen twee groepen sterrenhopen: de jonge, kleinere open sterrenhopen (die zich voornamelijk in de melkwegschijf bevinden) en de oude, grote bolvormige sterrenhopen (die zich in de halo bevinden). In hoofdstuk 5 onderzoeken we hoe die laatste groep beïnvloed wordt door getijdenkrachten veroorzaakt door de donkere materie halo waarin ze zich bevinden. Hiervoor koppelen we de CosmoGrid simulatie met nieuwe simulaties van de sterrenhopen.

De sterrenhopen die zich aan het eind van de simulatie het dichtst bij het centrum van de halo bevinden blijken ook gedurende hun hele leven de sterkste getijdenkrachten te hebben ondervonden. Hierdoor hebben deze ook de grootste hoeveelheid sterren verloren. Ook is er een onderscheid te maken tussen lokaal geboren sterrenhopen en immigrant-sterrenhopen, waarbij de laatste groep pas bij de halo kwam na diens laatste grote botsing met een andere halo. Deze immigrant-sterrenhopen blijken gemiddeld een minder sterk getijdenveld te hebben ervaren, waardoor ze aan het eind van de simulatie meer sterren hebben weten te behouden.

#### 7.4.5 Evolutie van sterrenhopen in een melkweg

In hoofdstuk 6 gebruiken we dezelfde methode als in hoofdstuk 5, maar nu passen we deze toe op open sterrenhopen in een gesimuleerd melkwegstelsel wat behalve donkere materie ook gas en sterren bevat. De gesimuleerde open sterrenhopen bevinden zich in de melkwegschijf, op ongeveer dezelfde afstand van het centrum als de Zon. Hierdoor kunnen we de gesimuleerde sterrenhopen vergelijken met waarnemingen van sterrenhopen in onze buurt. We simuleren sterrenhopen met verschillende waarden voor hun massa en straal aan het begin van de simulatie.

We zien dat de sterrenhopen die aan het begin een vrij grote straal (groter dan 7 parsec) hadden, relatief snel (binnen 100 miljoen jaar) uit elkaar vallen. De compactere sterrenhopen convergeren binnen 200 miljoen jaar naar een gemeenschappelijke straal van ongeveer 4 – 5 parsec. De groep van sterrenhopen die tot het eind overleeft, komt qua straal en massa vrij goed overeen met de waargenomen sterrenhopen. Geen van de gesimuleerde sterrenhopen blijft langer dan 1,1 miljard jaar bij elkaar, ook dit komt overeen met de waargenomen sterrenhopen.



## Bibliography

- MAPPER: Multiscale Applications on European e-Infrastructures, 2012. URL <http://www.mapper-project.eu>.
- S. J. Aarseth, E. L. Turner, and J. R. Gott, III. N-body simulations of galaxy clustering. I - Initial conditions and galaxy collapse times. *ApJ*, 228:664--683, March 1979. doi: 10.1086/156892.
- D. Adams. *The Hitch Hiker's Guide to the Galaxy: A Trilogy in Four Parts*. Hitchhiker's Guide to the Galaxy Series. Heinemann, 1986. ISBN 9780434009206. URL <http://books.google.nl/books?id=7hi-QgAACAAJ>.
- V. Antonuccio-Delogu, A. Dobrotka, U. Becciani, S. Cielo, C. Giocoli, A. V. Macciò, and A. Romeo-Veloná. Dissecting the spin distribution of dark matter haloes. *MNRAS*, 407:1338--1346, September 2010. doi: 10.1111/j.1365-2966.2010.16989.x.
- M. A. Aragon-Calvo and A. S. Szalay. The hierarchical structure and dynamics of voids. *MNRAS*, 428:3409--3424, February 2013. doi: 10.1093/mnras/sts281.
- M. A. Aragón-Calvo, B. J. T. Jones, R. van de Weygaert, and J. M. van der Hulst. The multiscale morphology filter: identifying and extracting spatial patterns in the galaxy distribution. *A&A*, 474:315--338, October 2007. doi: 10.1051/0004-6361:20077880.
- P. A. Araya-Melo, A. Reisenegger, A. Meza, R. van de Weygaert, R. Dünner, and H. Quintana. Future evolution of bound superclusters in an accelerating Universe. *MNRAS*, 399:97--120, October 2009. doi: 10.1111/j.1365-2966.2009.15292.x.
- J. S. Bagla and J. Prasad. Effects of the size of cosmological N-body simulations on physical quantities - I. Mass function. *MNRAS*, 370:993--1002, August 2006. doi: 10.1111/j.1365-2966.2006.10528.x.
- J. Bailin and M. Steinmetz. Internal and External Alignment of the Shapes and Angular Momenta of  $\Lambda$ CDM Halos. *ApJ*, 627:647--665, July 2005. doi: 10.1086/430397.
- H. Bal and K. Verstoep. Large-scale parallel computing on grids. *Electronic Notes in Theoretical Computer Science*, 220(2):3 -- 17, 2008. ISSN 1571-0661. doi: DOI:10.1016/j.entcs.2008.11.010. Proceedings of the 7th International Workshop on Parallel and Distributed Methods in verification (PDMC 2008).
- P. Bar, C. Coti, D. Groen, T. Herault, V. Kravtsov, M. Swain, and A. Schuster. Running parallel applications with topology-aware grid middleware. In *Fifth IEEE international conference on e-Science and Grid computing: Oxford, United Kingdom*, pages 292--299, Piscataway, NJ, December 2009. IEEE Computer Society.

- J. Barnes and P. Hut. A hierarchical  $O(N \log N)$  force-calculation algorithm. *Nature*, 324: 446--449, December 1986. doi: 10.1038/324446a0.
- H. Baumgardt and J. Makino. Dynamical evolution of star clusters in tidal fields. *MNRAS*, 340:227--246, March 2003. doi: 10.1046/j.1365-8711.2003.06286.x.
- H. Baumgardt, P. Côté, M. Hilker, M. Rejkuba, S. Mieske, S. G. Djorgovski, and P. Stetson. Limits on the dark matter content of globular clusters. In R. de Grijs & J. R. D. Lépine, editor, *IAU Symposium*, volume 266 of *IAU Symposium*, pages 365--365, January 2010. doi: 10.1017/S174392130999130X.
- J. Bédorf, E. Gaburov, and S. Portegies Zwart. A sparse octree gravitational N-body code that runs entirely on the GPU processor. *Journal of Computational Physics*, 231:2825--2839, April 2012. doi: 10.1016/j.jcp.2011.12.024.
- P. S. Behroozi, R. H. Wechsler, and H.-Y. Wu. The ROCKSTAR Phase-space Temporal Halo Finder and the Velocity Offsets of Cluster Cores. *ApJ*, 762:109, January 2013a. doi: 10.1088/0004-637X/762/2/109.
- P. S. Behroozi, R. H. Wechsler, H.-Y. Wu, M. T. Busha, A. A. Klypin, and J. R. Primack. Gravitationally Consistent Halo Catalogs and Merger Trees for Precision Cosmology. *ApJ*, 763:18, January 2013b. doi: 10.1088/0004-637X/763/1/18.
- I. Berentzen and E. Athanassoula. Star cluster evolution in barred disc galaxies - I. Planar periodic orbits. *MNRAS*, 419:3244--3257, February 2012. doi: 10.1111/j.1365-2966.2011.19964.x.
- E. Bertschinger. The self-similar evolution of holes in an Einstein-de Sitter universe. *ApJS*, 58:1--37, May 1985.
- E. Bertschinger. Multiscale Gaussian Random Fields and Their Application to Cosmological Simulations. *ApJS*, 137:1--20, November 2001. doi: 10.1086/322526.
- P. Bett, V. Eke, C. S. Frenk, A. Jenkins, J. Helly, and J. Navarro. The spin and shape of dark matter haloes in the Millennium simulation of a  $\Lambda$  cold dark matter universe. *MNRAS*, 376:215--232, March 2007. doi: 10.1111/j.1365-2966.2007.11432.x.
- B. Beygu, K. Kreckel, R. van de Weygaert, J. M. van der Hulst, and J. H. van Gorkom. An Interacting Galaxy System along a Filament in a Void. *AJ*, 145:120, May 2013. doi: 10.1088/0004-6256/145/5/120.
- G. R. Blumenthal, L. N. da Costa, D. S. Goldwirth, M. Lecar, and T. Piran. The largest possible voids. *ApJ*, 388:234--241, April 1992.
- J.R. Bond, L. Kofman, and D. Pogosyan. How filaments of galaxies are woven into the cosmic web. *Nature*, 380(6575):603--606, April 1996.
- M. Boylan-Kolchin, V. Springel, S. D. M. White, A. Jenkins, and G. Lemson. Resolving cosmic structure formation with the Millennium-II Simulation. *MNRAS*, 398:1150--1164, September 2009. doi: 10.1111/j.1365-2966.2009.15191.x.
- M. Boylan-Kolchin, V. Springel, S. D. M. White, and A. Jenkins. There's no place like home? Statistics of Milky Way-mass dark matter haloes. *MNRAS*, 406:896--912, August 2010. doi: 10.1111/j.1365-2966.2010.16774.x.
- B. Brandl, B. J. Sams, F. Bertoldi, A. Eckart, R. Genzel, S. Drapatz, R. Hofmann, M. Loewe, and A. Quirrenbach. Adaptive Optics Near-Infrared Imaging of R136 in 30 Doradus: The Stellar Population of a Nearby Starburst. *ApJ*, 466:254, July 1996.



doi: 10.1086/177507.

- J. P. Brodie and J. Strader. Extragalactic Globular Clusters and Galaxy Formation. *ARA&A*, 44:193--267, September 2006. doi: 10.1146/annurev.astro.44.051905.092441.
- G. L. Bryan and M. L. Norman. Statistical Properties of X-Ray Clusters: Analytic and Numerical Comparisons. *ApJ*, 495:80--+, March 1998. doi: 10.1086/305262.
- J. S. Bullock, A. Dekel, T. S. Kolatt, A. V. Kravtsov, A. A. Klypin, C. Porciani, and J. R. Primack. A Universal Angular Momentum Profile for Galactic Halos. *ApJ*, 555:240--257, July 2001a. doi: 10.1086/321477.
- J. S. Bullock, T. S. Kolatt, Y. Sigad, R. S. Somerville, A. V. Kravtsov, A. A. Klypin, J. R. Primack, and A. Dekel. Profiles of dark haloes: evolution, scatter and environment. *MNRAS*, 321:559--575, March 2001b. doi: 10.1046/j.1365-8711.2001.04068.x.
- M. T. Busha, R. H. Wechsler, P. S. Behroozi, B. F. Gerke, A. A. Klypin, and J. R. Primack. Statistics of Satellite Galaxies around Milky-Way-like Hosts. *ApJ*, 743:117, December 2011. doi: 10.1088/0004-637X/743/2/117.
- M. Cautun, R. van de Weygaert, and B. J. T. Jones. NEXUS: tracing the cosmic web connection. *MNRAS*, 429:1286--1308, February 2013. doi: 10.1093/mnras/sts416.
- M. C. Cautun and R. van de Weygaert. The DTFE public software - The Delaunay Tessellation Field Estimator code. *arXiv:1105.0370*, May 2011.
- L. Ceccarelli, N. D. Padilla, C. Valotto, and D. G. Lambas. Voids in the 2dFGRS and  $\Lambda$ CDM simulations: spatial and dynamical properties. *MNRAS*, 373:1440--1450, December 2006.
- D. F. Chernoff and M. D. Weinberg. Evolution of globular clusters in the Galaxy. *ApJ*, 351:121--156, March 1990. doi: 10.1086/168451.
- G. Chincarini and H. J. Rood. Size of the Coma cluster. *Nature*, 257:294, 295, September 1975.
- C. Conroy, A. Loeb, and D. N. Spergel. Evidence against Dark Matter Halos Surrounding the Globular Clusters MGC1 and NGC 2419. *ApJ*, 741:72, November 2011. doi: 10.1088/0004-637X/741/2/72.
- E. Contini, G. De Lucia, and S. Borgani. Statistics of substructures in dark matter haloes. *MNRAS*, 420:2978--2989, March 2012. doi: 10.1111/j.1365-2966.2011.20149.x.
- R A Crain, T Theuns, C Dalla Vecchia, V R Eke, C S Frenk, A Jenkins, S T Kay, J A Peacock, F R Pearce, J Schaye, V Springel, P A Thomas, S D M White, and R P C Wiersma. Galaxies-intergalactic medium interaction calculation - I. Galaxy formation as a function of large-scale environment. *MNRAS*, 399:1773--1794, 2009.
- M. Crocce, P. Fosalba, F. J. Castander, and E. Gaztañaga. Simulating the Universe with MICE: the abundance of massive clusters. *MNRAS*, 403:1353--1367, April 2010. doi: 10.1111/j.1365-2966.2009.16194.x.
- R. de Grijs, G. F. Gilmore, A. D. Mackey, M. I. Wilkinson, S. F. Beaulieu, R. A. Johnson, and B. X. Santiago. Mass segregation in young compact clusters in the Large Magellanic Cloud - III. Implications for the initial mass function. *MNRAS*, 337:597--608, December 2002. doi: 10.1046/j.1365-8711.2002.05954.x.
- V. de Lapparent, M. J. Geller, and J. P. Huchra. A slice of the universe. *ApJL*, 302:L1--L5,

- March 1986. doi: 10.1086/184625.
- Tom DeFanti, Cees de Laat, Joe Mambretti, Kees Neggers, and Bill St. Arnaud. Translight: a global-scale lambda-grid for e-science. *Commun. ACM*, 46(11):34--41, November 2003. ISSN 0001-0782. doi: 10.1145/948383.948407. URL <http://doi.acm.org/10.1145/948383.948407>.
- J. Diemand, B. Moore, and J. Stadel. Convergence and scatter of cluster density profiles. *MNRAS*, 353:624--632, September 2004. doi: 10.1111/j.1365-2966.2004.08094.x.
- J. Diemand, M. Zemp, B. Moore, J. Stadel, and C. M. Carollo. Cusps in cold dark matter haloes. *MNRAS*, 364:665--673, December 2005. doi: 10.1111/j.1365-2966.2005.09601.x.
- J. Diemand, M. Kuhlen, and P. Madau. Dark Matter Substructure and Gamma-Ray Annihilation in the Milky Way Halo. *ApJ*, 657:262--270, March 2007. doi: 10.1086/510736.
- J. Diemand, M. Kuhlen, P. Madau, M. Zemp, B. Moore, D. Potter, and J. Stadel. Clumps and streams in the local dark matter distribution. *Nature*, 454:735--738, August 2008. doi: 10.1038/nature07153.
- J. Dubinski, L. N. da Costa, D. S. Goldwirth, M. Lecar, and T. Piran. Void evolution and the large-scale structure. *ApJ*, 410(2):458--468, June 1993.
- G. Efstathiou. The clustering of galaxies and its dependence upon Omega. *MNRAS*, 187: 117--127, April 1979.
- J. Einasto, I. Suhhonenko, G. Hütsi, E. Saar, M. Einasto, L. J. Liivamägi, V. Müller, A. A. Starobinsky, E. Tago, and E. Tempel. Towards understanding the structure of voids in the cosmic web. *A&A*, 534:A128, October 2011.
- B. G. Elmegreen. The Globular Cluster Mass Function as a Remnant of Violent Birth. *ApJ*, 712:L184--L188, April 2010. doi: 10.1088/2041-8205/712/2/L184.
- A. E. Evrard, T. J. MacFarland, H. M. P. Couchman, J. M. Colberg, N. Yoshida, S. D. M. White, A. Jenkins, C. S. Frenk, F. R. Pearce, J. A. Peacock, and P. A. Thomas. Galaxy Clusters in Hubble Volume Simulations: Cosmological Constraints from Sky Survey Populations. *ApJ*, 573:7--36, July 2002. doi: 10.1086/340551.
- S. M. Fall. On the evolution of galaxy clustering and cosmological N-body simulations. *MNRAS*, 185:165--178, October 1978.
- A. Franquin. *Die Reuze Flater*. Dupuis, 1972. ISBN 9031401005.
- M. Frigo and S. Johnson. The design and implementation of fftw3. In *Proceedings of the IEEE*, volume 93, pages 216--231, Feb 2005.
- T. Fukushige and J. Makino. On the Origin of Cusps in Dark Matter Halos. *ApJ*, 477: L9, March 1997. doi: 10.1086/310516.
- T. Fukushige and J. Makino. Structure of Dark Matter Halos from Hierarchical Clustering. *ApJ*, 557:533--545, August 2001. doi: 10.1086/321666.
- T. Fukushige and J. Makino. Structure of Dark Matter Halos from Hierarchical Clustering. II. Dependence of Cosmological Models in Cluster-sized Halos. *ApJ*, 588:674--679, May 2003. doi: 10.1086/374206.
- T. Fukushige, A. Kawai, and J. Makino. Structure of Dark Matter Halos from Hierarchical Clustering. III. Shallowing of the Inner Cusp. *ApJ*, 606:625--634, May 2004. doi:

10.1086/383192.

- M. Fujii, M. Iwasawa, Y. Funato, and J. Makino. BRIDGE: A Direct-Tree Hybrid N-Body Algorithm for Fully Self-Consistent Simulations of Star Clusters and Their Parent Galaxies. *PASJ*, 59:1095--, December 2007.
- S.R. Furlanetto and T. Piran. The evidence of absence: galaxy voids in the excursion set formalism. *MNRAS*, 366(2):467--479, February 2006.
- E. Gabriel, M. Resch, T. Beisel, and R. Keller. Distributed computing in a heterogeneous computing environment. In *Recent Advances in Parallel Virtual Machine and Message Passing Interface*, volume 1497 of *Lecture Notes in Computer Science*, pages 180--187. Springer, 1998.
- E. Gabriel, G. E. Fagg, G. Bosilca, T. Angskun, J. J. Dongarra, J. M. Squyres, V. Sahay, P. Kambadur, B. Barrett, A. Lumsdaine, R. H. Castain, D. J. Daniel, R. L. Graham, and T. S. Woodall. Open MPI: Goals, concept, and design of a next generation MPI implementation. In *Proceedings, 11th European PVM/MPI Users' Group Meeting*, pages 97--104, Budapest, Hungary, September 2004.
- L. Gao, S. D. M. White, A. Jenkins, F. Stoehr, and V. Springel. The subhalo populations of  $\Lambda$ CDM dark haloes. *MNRAS*, 355:819--834, December 2004. doi: 10.1111/j.1365-2966.2004.08360.x.
- L. Gao, J. F. Navarro, S. Cole, C. S. Frenk, S. D. M. White, V. Springel, A. Jenkins, and A. F. Neto. The redshift dependence of the structure of massive  $\Lambda$  cold dark matter haloes. *MNRAS*, 387:536--544, June 2008. doi: 10.1111/j.1365-2966.2008.13277.x.
- L. Gao, C. S. Frenk, M. Boylan-Kolchin, A. Jenkins, V. Springel, and S. D. M. White. The statistics of the subhalo abundance of dark matter haloes. *MNRAS*, 410:2309--2314, February 2011. doi: 10.1111/j.1365-2966.2010.17601.x.
- S. Ghigna, B. Moore, F. Governato, G. Lake, T. Quinn, and J. Stadel. Density Profiles and Substructure of Dark Matter Halos: Converging Results at Ultra-High Numerical Resolution. *ApJ*, 544:616--628, December 2000. doi: 10.1086/317221.
- M. Gieles, E. Athanassoula, and S. F. Portegies Zwart. The effect of spiral arm passages on the evolution of stellar clusters. *MNRAS*, 376:809--819, April 2007. doi: 10.1111/j.1365-2966.2007.11477.x.
- M. Giersz. Monte Carlo simulations of star clusters - II. Tidally limited, multimass systems with stellar evolution. *MNRAS*, 324:218--230, June 2001. doi: 10.1046/j.1365-8711.2001.04337.x.
- M. Giersz and D. C. Heggie. Monte Carlo simulations of star clusters - VI. The globular cluster NGC 6397. *MNRAS*, 395:1173--1183, May 2009. doi: 10.1111/j.1365-2966.2009.14638.x.
- M. Giersz and D. C. Heggie. Monte Carlo simulations of star clusters - VII. The globular cluster 47 Tuc. *MNRAS*, 410:2698--2713, February 2011. doi: 10.1111/j.1365-2966.2010.17648.x.
- O. Y. Gnedin and J. P. Ostriker. Destruction of the Galactic Globular Cluster System. *ApJ*, 474:223, January 1997. doi: 10.1086/303441.
- D. M. Goldberg and M. S. Vogeley. Simulating Voids. *ApJ*, 605:1--6, April 2004.
- S. Gottlöber, E. L. Łokas, A. Klypin, and Y. Hoffman. The structure of voids. *MNRAS*,

- 344:715--724, September 2003.
- A. W. Graham, D. Merritt, B. Moore, J. Diemand, and B. Terzić. Empirical Models for Dark Matter Halos. II. Inner Profile Slopes, Dynamical Profiles, and  $\rho/\sigma^3$ . *AJ*, 132: 2701--2710, December 2006. doi: 10.1086/508990.
- S. A. Gregory and L. A. Thompson. The Coma/A1367 supercluster and its environs. *ApJ*, 222(1):784--799, June 1978.
- D. Groen, S. Rieder, P. Grosso, C. de Laat, and S. Portegies Zwart. A lightweight communication library for distributed computing. *Computational Science and Discovery*, 3(1):015002--+, January 2010. doi: 10.1088/1749-4699/3/1/015002.
- D. Groen, S. Portegies Zwart, T. Ishiyama, and J. Makino. High-performance gravitational N-body simulations on a planet-wide-distributed supercomputer. *Computational Science and Discovery*, 4(1):015001--+, January 2011. doi: 10.1088/1749-4699/4/1/015001.
- N. A. Groggin and M. J. Geller. An Imaging and Spectroscopic Survey of Galaxies within Prominent Nearby Voids. I. The Sample and Luminosity Distribution. *AJ*, 118:2561--2580, December 1999.
- N. A. Groggin and M. J. Geller. An Imaging and Spectroscopic Survey of Galaxies within Prominent Nearby Voids. II. Morphologies, Star Formation, and Faint Companions. *AJ*, 119:32--43, January 2000.
- A. Gualandris, S. Portegies Zwart, and A. Tirado-Ramos. Performance analysis of direct n-body algorithms for astrophysical simulations on distributed systems. *Parallel Computing*, 33(3):159--173, 2007.
- M R Haas, J Schaye, C M Booth, C Dalla Vecchia, V Springel, T Theuns, and R P C Wiersma. Physical properties of simulated galaxy populations at  $z=2$  -- I. Effect of metal-line cooling and feedback from star formation and AGN. *MNRAS*, astro-ph.CO, 2012.
- E. Hayashi, J. F. Navarro, C. Power, A. Jenkins, C. S. Frenk, S. D. M. White, V. Springel, J. Stadel, and T. R. Quinn. The inner structure of  $\Lambda$ CDM haloes - II. Halo mass profiles and low surface brightness galaxy rotation curves. *MNRAS*, 355:794--812, December 2004. doi: 10.1111/j.1365-2966.2004.08359.x.
- D. C. Heggie and R. D. Mathieu. Standardised Units and Time Scales. In P. Hut & S. L. W. McMillan, editor, *The Use of Supercomputers in Stellar Dynamics*, volume 267 of *Lecture Notes in Physics*, Berlin Springer Verlag, page 233, 1986. doi: 10.1007/BFb0116419.
- R. W. Hockney and J. W. Eastwood. *Computer Simulation Using Particles*. 1981.
- Y. Hoffman and J. Shaham. On the origin of the voids in the galaxy distribution. *ApJL*, 262:L23--L26, November 1982.
- F. Hoyle and M. S. Vogeley. Voids in the Point Source Catalogue Survey and the Updated Zwicky Catalog. *ApJ*, 566:641--651, February 2002.
- F. Hoyle and M. S. Vogeley. Voids in the Two-Degree Field Galaxy Redshift Survey. *ApJ*, 607:751--764, June 2004.
- F. Hoyle, M. S. Vogeley, and D. Pan. Photometric properties of void galaxies in the Sloan Digital Sky Survey Data Release 7. *MNRAS*, 426:3041--3050, November 2012. doi:

- 10.1111/j.1365-2966.2012.21943.x.
- V. Icke. Voids and filaments. *MNRAS*, 206:1P--3P, January 1984.
- T. Ishiyama, T. Fukushige, and J. Makino. Environmental Effect on the Subhalo Abundance --- a Solution to the Missing Dwarf Problem. *PASJ*, 60:L13, August 2008.
- T. Ishiyama, T. Fukushige, and J. Makino. Variation of the Subhalo Abundance in Dark Matter Halos. *ApJ*, 696:2115--2125, May 2009a. doi: 10.1088/0004-637X/696/2/2115.
- T. Ishiyama, T. Fukushige, and J. Makino. GreeM: Massively Parallel TreePM Code for Large Cosmological N-body Simulations. *PASJ*, 61:1319--, December 2009b.
- T. Ishiyama, K. Nitadori, and J. Makino. 4.45 Pflops Astrophysical N-Body Simulation on K computer -- The Gravitational Trillion-Body Problem. *arXiv: 1211.4406*, November 2012.
- T. Ishiyama, S. Rieder, J. Makino, S. Portegies Zwart, D. Groen, K. Nitadori, C. de Laet, S. McMillan, K. Hiraki, and S. Harfst. The Cosmogrid Simulation: Statistical Properties of Small Dark Matter Halos. *ApJ*, 767:146, April 2013. doi: 10.1088/0004-637X/767/2/146.
- A. Jenkins, C. S. Frenk, S. D. M. White, J. M. Colberg, S. Cole, A. E. Evrard, H. M. P. Couchman, and N. Yoshida. The mass function of dark matter haloes. *MNRAS*, 321: 372--384, February 2001. doi: 10.1046/j.1365-8711.2001.04029.x.
- Y. P. Jing. The Density Profile of Equilibrium and Nonequilibrium Dark Matter Halos. *ApJ*, 535:30--36, May 2000. doi: 10.1086/308809.
- Y. P. Jing and Y. Suto. The Density Profiles of the Dark Matter Halo Are Not Universal. *ApJ*, 529:L69--L72, February 2000. doi: 10.1086/312463.
- Y. P. Jing and Y. Suto. Triaxial Modeling of Halo Density Profiles with High-Resolution N-Body Simulations. *ApJ*, 574:538--553, August 2002. doi: 10.1086/341065.
- V. E. Karachentseva, I. D. Karachentsev, and G. M. Richter. A list of nearby dwarf galaxies towards the Local Void in Hercules-Aquila. *A&AS*, 135:221--226, March 1999.
- N. Karonis, B. Toonen, and I. Foster. Mpich-g2: A grid-enabled implementation of the message passing interface. *Journal of Parallel and Distributed Computing*, 63(5):551 -- 563, 2003. ISSN 0743-7315. Special Issue on Computational Grids.
- A. Kawai, J. Makino, and T. Ebisuzaki. Performance Analysis of High-Accuracy Tree Code Based on the Pseudoparticle Multipole Method. *ApJS*, 151:13--33, March 2004. doi: 10.1086/381391.
- S. Kazantzidis, A. R. Zentner, and A. V. Kravtsov. The Robustness of Dark Matter Density Profiles in Dissipationless Mergers. *ApJ*, 641:647--664, April 2006. doi: 10.1086/500579.
- N. V. Kharchenko, A. E. Piskunov, S. Röser, E. Schilbach, and R.-D. Scholz. Astrophysical parameters of Galactic open clusters. *A&A*, 438:1163--1173, August 2005. doi: 10.1051/0004-6361:20042523.
- J. Kim, C. Park, J. R. Gott, III, and J. Dubinski. The Horizon Run N-Body Simulation: Baryon Acoustic Oscillations and Topology of Large-scale Structure of the Universe. *ApJ*, 701:1547, August 2009. doi: 10.1088/0004-637X/701/2/1547.
- R. P. Kirshner, Jr. Oemler, A., P. L. Schechter, and S. A. Shectman. A million cubic

- megaparsec void in Bootes. *ApJ*, 248:L57--L60, September 1981.
- R. P. Kirshner, A. Oemler, Jr., P. L. Schechter, and S. A. Shectman. A survey of the Bootes void. *ApJ*, 314:493--506, March 1987.
- A. Klypin, A. V. Kravtsov, O. Valenzuela, and F. Prada. Where Are the Missing Galactic Satellites? *ApJ*, 522:82--92, September 1999. doi: 10.1086/307643.
- A. Klypin, A. V. Kravtsov, J. S. Bullock, and J. R. Primack. Resolving the Structure of Cold Dark Matter Halos. *ApJ*, 554:903--915, June 2001. doi: 10.1086/321400.
- A. A. Klypin, S. Trujillo-Gomez, and J. Primack. Dark Matter Halos in the Standard Cosmological Model: Results from the Bolshoi Simulation. *ApJ*, 740:102, October 2011. doi: 10.1088/0004-637X/740/2/102.
- A. Knebe and C. Power. On the Correlation between Spin Parameter and Halo Mass. *ApJ*, 678:621--626, May 2008. doi: 10.1086/586702.
- A. Knebe, S. R. Knollmann, S. I. Muldrew, F. R. Pearce, M. A. Aragon-Calvo, Y. Ascasibar, P. S. Behroozi, D. Ceverino, S. Colombi, J. Diemand, K. Dolag, B. L. Falck, P. Fasel, J. Gardner, S. Gottlöber, C.-H. Hsu, F. Iannuzzi, A. Klypin, Z. Lukić, M. Maciejewski, C. McBride, M. C. Neyrinck, S. Planelles, D. Potter, V. Quilis, Y. Rasera, J. I. Read, P. M. Ricker, F. Roy, V. Springel, J. Stadel, G. Stinson, P. M. Sutter, V. Turchaninov, D. Tweed, G. Yepes, and M. Zemp. Haloes gone MAD: The Halo-Finder Comparison Project. *MNRAS*, 415:2293--2318, August 2011. doi: 10.1111/j.1365-2966.2011.18858.x.
- L. M. Krauss and B. Chaboyer. Age Estimates of Globular Clusters in the Milky Way: Constraints on Cosmology. *Science*, 299:65--70, January 2003. doi: 10.1126/science.1075631.
- A. V. Kravtsov and O. Y. Gnedin. Formation of Globular Clusters in Hierarchical Cosmology. *ApJ*, 623:650--665, April 2005. doi: 10.1086/428636.
- K. Kreckel, E. Platen, M. A. Aragon-Calvo, J. H. van Gorkom, R. van de Weygaert, J. M. van der Hulst, K. Kováč, C.-W. Yip, and P. J. E. Peebles. Only the Lonely: HI Imaging of Void Galaxies. *AJ*, 141:4, January 2011.
- K. Kreckel, E. Platen, M. A. Aragon-Calvo, J. H. van Gorkom, R. van de Weygaert, J. M. van der Hulst, and B. Beygu. The Void Galaxy Survey: Optical Properties and HI Morphology and Kinematics. *AJ*, 144:16, July 2012.
- P. Kroupa, B. Famaey, K. S. de Boer, J. Dabringhausen, M. S. Pawłowski, C. M. Boily, H. Jerjen, D. Forbes, G. Hensler, and M. Metz. Local-Group tests of dark-matter concordance cosmology. Towards a new paradigm for structure formation. *A&A*, 523: A32+, November 2010. doi: 10.1051/0004-6361/201014892.
- Pavel Kroupa. On the variation of the initial mass function. *Monthly Notices of the Royal Astronomical Society*, 322(2):231--246, April 2001.
- J. M. D. Kruijssen, F. I. Pelupessy, H. J. G. L. M. Lamers, S. F. Portegies Zwart, and V. Icke. Modelling the formation and evolution of star cluster populations in galaxy simulations. *MNRAS*, 414:1339--1364, June 2011. doi: 10.1111/j.1365-2966.2011.18467.x.
- J. M. D. Kruijssen, F. I. Pelupessy, H. J. G. L. M. Lamers, S. F. Portegies Zwart, N. Bastian, and V. Icke. Formation versus destruction: the evolution of the star

- cluster population in galaxy mergers. *MNRAS*, 421:1927--1941, April 2012. doi: 10.1111/j.1365-2966.2012.20322.x.
- B. Kuhn, U. Hopp, and H. Elsaesser. Results of a search for faint galaxies in voids. *A&A*, 318:405--415, February 1997.
- C. Lacey and S. Cole. Merger rates in hierarchical models of galaxy formation. *MNRAS*, 262:627--649, June 1993.
- C. Lacey and S. Cole. Merger Rates in Hierarchical Models of Galaxy Formation - Part Two - Comparison with N-Body Simulations. *MNRAS*, 271:676--+, December 1994.
- C. J. Lada and E. A. Lada. Embedded Clusters in Molecular Clouds. *ARA&A*, 41: 57--115, 2003. doi: 10.1146/annurev.astro.41.011802.094844.
- H. J. G. L. M. Lamers and M. Gieles. Clusters in the solar neighbourhood: how are they destroyed? *A&A*, 455:L17--L20, August 2006. doi: 10.1051/0004-6361:20065567.
- H. J. G. L. M. Lamers, M. Gieles, N. Bastian, H. Baumgardt, N. V. Kharchenko, and S. Portegies Zwart. An analytical description of the disruption of star clusters in tidal fields with an application to Galactic open clusters. *A&A*, 441:117--129, October 2005. doi: 10.1051/0004-6361:20042241.
- H. J. G. L. M. Lamers, H. Baumgardt, and M. Gieles. Mass-loss rates and the mass evolution of star clusters. *MNRAS*, 409:305--328, November 2010. doi: 10.1111/j.1365-2966.2010.17309.x.
- S. S. Larsen. The mass function of young star clusters in spiral galaxies. *A&A*, 494:539--551, February 2009. doi: 10.1051/0004-6361:200811212.
- Y.-S. Li, A. Helmi, G. De Lucia, and F. Stoehr. On the common mass scale of the Milky Way satellites. *MNRAS*, 397:L87--L91, July 2009. doi: 10.1111/j.1745-3933.2009.00690.x.
- Z. Lukić, K. Heitmann, S. Habib, S. Bashinsky, and P. M. Ricker. The Halo Mass Function: High-Redshift Evolution and Universality. *ApJ*, 671:1160--1181, December 2007. doi: 10.1086/523083.
- A. V. Macciò, A. A. Dutton, F. C. van den Bosch, B. Moore, D. Potter, and J. Stadel. Concentration, spin and shape of dark matter haloes: scatter and the dependence on mass and environment. *MNRAS*, 378:55--71, June 2007. doi: 10.1111/j.1365-2966.2007.11720.x.
- A. V. Macciò, A. A. Dutton, and F. C. van den Bosch. Concentration, spin and shape of dark matter haloes as a function of the cosmological model: WMAP1, WMAP3 and WMAP5 results. *MNRAS*, 391:1940--1954, December 2008. doi: 10.1111/j.1365-2966.2008.14029.x.
- A. V. Macciò, X. Kang, and B. Moore. Central Mass and Luminosity of Milky Way Satellites in the  $\Lambda$  Cold Dark Matter Model. *ApJ*, 692:L109--L112, February 2009. doi: 10.1088/0004-637X/692/2/L109.
- J. Makino. A Fast Parallel Treecode with GRAPE. *PASJ*, 56:521--531, June 2004.
- S. Manos, M. Mazzeo, O. Kenway, P. V. Coveney, N. T. Karonis, and B. R. Toonen. Distributed mpi cross-site run performance using mpig. In *HPDC*, pages 229--230, 2008.
- H. Matsui, T. R. Saitoh, J. Makino, K. Wada, K. Tomisaka, E. Kokubo, H. Daisaka,

- T. Okamoto, and N. Yoshida. Origin of Multiple Nuclei in Ultraluminous Infrared Galaxies. *ApJ*, 746:26, February 2012. doi: 10.1088/0004-637X/746/1/26.
- S. McMillan, S. Portegies Zwart, A. van Elteren, and A. Whitehead. Simulations of Dense Stellar Systems with the AMUSE Software Toolkit. 453:129, July 2012.
- D. Merritt, A. W. Graham, B. Moore, J. Diemand, and B. Terzić. Empirical Models for Dark Matter Halos. I. Nonparametric Construction of Density Profiles and Comparison with Parametric Models. *AJ*, 132:2685--2700, December 2006. doi: 10.1086/508988.
- K. Miyoshi and T. Kihara. Development of the correlation of galaxies in an expanding universe. *PASJ*, 27:333--346, 1975.
- B. Moore, S. Ghigna, F. Governato, G. Lake, T. Quinn, J. Stadel, and P. Tozzi. Dark Matter Substructure within Galactic Halos. *ApJ*, 524:L19--L22, October 1999a. doi: 10.1086/312287.
- B. Moore, T. Quinn, F. Governato, J. Stadel, and G. Lake. Cold collapse and the core catastrophe. *MNRAS*, 310:1147--1152, December 1999b. doi: 10.1046/j.1365-8711.1999.03039.x.
- J. C. Muñoz-Cuartas, A. V. Macciò, S. Gottlöber, and A. A. Dutton. The redshift evolution of  $\Lambda$  cold dark matter halo parameters: concentration, spin and shape. *MNRAS*, 411:584--594, February 2011. doi: 10.1111/j.1365-2966.2010.17704.x.
- J. F. Navarro, C. S. Frenk, and S. D. M. White. A Universal Density Profile from Hierarchical Clustering. *ApJ*, 490:493--+, December 1997. doi: 10.1086/304888.
- J. F. Navarro, E. Hayashi, C. Power, A. R. Jenkins, C. S. Frenk, S. D. M. White, V. Springel, J. Stadel, and T. R. Quinn. The inner structure of  $\Lambda$ CDM haloes - III. Universality and asymptotic slopes. *MNRAS*, 349:1039--1051, April 2004. doi: 10.1111/j.1365-2966.2004.07586.x.
- J. F. Navarro, A. Ludlow, V. Springel, J. Wang, M. Vogelsberger, S. D. M. White, A. Jenkins, C. S. Frenk, and A. Helmi. The diversity and similarity of simulated cold dark matter haloes. *MNRAS*, 402:21--34, February 2010. doi: 10.1111/j.1365-2966.2009.15878.x.
- A. F. Neto, L. Gao, P. Bett, S. Cole, J. F. Navarro, C. S. Frenk, S. D. M. White, V. Springel, and A. Jenkins. The statistics of  $\Lambda$  CDM halo concentrations. *MNRAS*, 381:1450--1462, November 2007. doi: 10.1111/j.1365-2966.2007.12381.x.
- M. Norman, P. Beckman, G. Bryan, J. Dubinski, D. Gannon, L. Hernquist, K. Keahay, J. Ostriker, J. Shalf, J. Welling, and S. Yang. Galaxies collide on the i-way: an example of heterogeneous wide-area collaborative supercomputing. *International Journal of High Performance Computing Applications*, 10(2-3):132--144, 1996. doi: 10.1177/109434209601000202.
- T. Okamoto and C. S. Frenk. The origin of failed subhaloes and the common mass scale of the Milky Way satellite galaxies. *MNRAS*, 399:L174--L178, October 2009. doi: 10.1111/j.1745-3933.2009.00748.x.
- J. Onions, A. Knebe, F. R. Pearce, S. I. Muldrew, H. Lux, S. R. Knollmann, Y. Ascasibar, P. Behroozi, P. Elahi, J. Han, M. Maciejewski, M. E. Merchán, M. Neyrinck, A. N. Ruiz, M. A. Sgró, V. Springel, and D. Tweed. Subhaloes going Notts:



- the subhalo-finder comparison project. *MNRAS*, 423:1200--1214, June 2012. doi: 10.1111/j.1365-2966.2012.20947.x.
- J. H. Oort. Summary - From the Astronomical Point of View. *Ricerche Astronomiche*, 5: 507, 1958.
- B. Paczynski. A test of the galactic origin of gamma-ray bursts. *ApJ*, 348:485--494, January 1990. doi: 10.1086/168257.
- C. Park, Y.-Y. Choi, M. S. Vogeley, J. R. Gott, III, M. R. Blanton, and SDSS Collaboration. Environmental Dependence of Properties of Galaxies in the Sloan Digital Sky Survey. *ApJ*, 658:898--916, April 2007.
- D. Park and J. Lee. The size distribution of void filaments in a  $\Lambda$ CDM cosmology. *MNRAS*, 397:2163--2169, August 2009. doi: 10.1111/j.1365-2966.2009.15117.x.
- S. G. Patiri, J. E. Betancort-Rijo, F. Prada, A. Klypin, and S. Gottlöber. Statistics of voids in the two-degree Field Galaxy Redshift Survey. *MNRAS*, 369:335--348, June 2006a.
- S. G. Patiri, F. Prada, J. Holtzman, A. Klypin, and J. Betancort-Rijo. The properties of galaxies in voids. *MNRAS*, 372:1710--1720, November 2006b.
- J. A. Peacock. *Cosmological Physics*. January 1999.
- F. I. Pelupessy. *Numerical studies of the interstellar medium on galactic scales*. PhD thesis, Leiden Observatory, Leiden University, P.O. Box 9513, 2300 RA Leiden, The Netherlands, March 2005.
- F. I. Pelupessy and S. Portegies Zwart. The evolution of embedded star clusters. *MNRAS*, page 2133, December 2011. doi: 10.1111/j.1365-2966.2011.20137.x.
- F. I. Pelupessy, A. van Elteren, N. de Vries, S. L. W. McMillan, N. Drost, and S. F. Portegies Zwart. The Astrophysical Multipurpose Software Environment. *arXiv:1307.3016*, July 2013.
- Planck Collaboration, P. A. R. Ade, N. Aghanim, C. Armitage-Caplan, M. Arnaud, M. Ashdown, F. Atrio-Barandela, J. Aumont, C. Baccigalupi, A. J. Banday, and et al. Planck 2013 results. I. Overview of products and scientific results. *arXiv: 1303.5062*, March 2013.
- E. Platen. *A Void Perspective of the Cosmic Web*. PhD thesis, University of Groningen, November 2009.
- E. Platen, R. van de Weygaert, and B. J. T. Jones. Alignment of voids in the cosmic web. *MNRAS*, 387:128--136, June 2008. doi: 10.1111/j.1365-2966.2008.13019.x.
- Erwin Platen, Rien van de Weygaert, and Bernard J. T. Jones. A cosmic watershed: the WVF void detection technique. *MNRAS*, 380(2):551--570, September 2007.
- H. C. Plummer. On the problem of distribution in globular star clusters. *MNRAS*, 71: 460--470, March 1911.
- D. Pogosyan, J. R. Bond, L. Kofman, and J. Wadsley. Cosmic Web: Origin and Observables. In S. Colombi, Y. Mellier, and B. Raban, editors, *Wide Field Surveys in Cosmology*, page 61, 1998.
- C. C. Popescu, U. Hopp, and H. Elsaesser. Erratum: Results of a search for emission-line galaxies towards nearby voids. The spatial distribution. *A&A*, 328:756, December 1997.
- S. Portegies Zwart, S. McMillan, S. Harfst, D. Groen, M. Fujii, B. Ó. Nualláin, E. Glebbeek, D. Heggie, J. Lombardi, P. Hut, V. Angelou, S. Banerjee, H. Belkus,

- T. Fragos, J. Fregeau, E. Gaburov, R. Izzard, M. Jurić, S. Justham, A. Sottoriva, P. Teuben, J. van Bever, O. Yaron, and M. Zemp. A multiphysics and multiscale software environment for modeling astrophysical systems. *New A*, 14:369--378, May 2009. doi: 10.1016/j.newast.2008.10.006.
- S. Portegies Zwart, T. Ishiyama, D. Groen, K. Nitadori, J. Makino, C. de Laat, S. McMillan, K. Hiraki, S. Harfst, and P. Grosso. Simulating the universe on an intercontinental grid of supercomputers. *IEEE Computer*, v.43, No.8, p.63-70, 43:63--70, October 2010a. doi: 10.1109/MC.2009.419.
- S. Portegies Zwart, S. McMillan, I. Pelupessy, and A. van Elteren. Multi-physics simulations using a hierarchical interchangeable software interface. *arXiv:1110.2785*, October 2011.
- S. Portegies Zwart, S. L. W. McMillan, E. van Elteren, I. Pelupessy, and N. de Vries. Multi-physics simulations using a hierarchical interchangeable software interface. *Computer Physics Communications*, 183:456--468, March 2013. doi: 10.1016/j.cpc.2012.09.024.
- S. F. Portegies Zwart and F. Verbunt. Population synthesis of high-mass binaries. *A&A*, 309:179--196, May 1996.
- S. F. Portegies Zwart, P. Hut, J. Makino, and S. L. W. McMillan. On the dissolution of evolving star clusters. *A&A*, 337:363--371, September 1998.
- S. F. Portegies Zwart, S. L. W. McMillan, and M. Gieles. Young Massive Star Clusters. *ARA&A*, 48:431--493, September 2010b. doi: 10.1146/annurev-astro-081309-130834.
- C. Power and A. Knebe. The impact of box size on the properties of dark matter haloes in cosmological simulations. *MNRAS*, 370:691--701, August 2006. doi: 10.1111/j.1365-2966.2006.10562.x.
- C. Power, J. F. Navarro, A. Jenkins, C. S. Frenk, S. D. M. White, V. Springel, J. Stadel, and T. Quinn. The inner structure of  $\Lambda$ CDM haloes - I. A numerical convergence study. *MNRAS*, 338:14--34, January 2003. doi: 10.1046/j.1365-8711.2003.05925.x.
- C. Power, A. Knebe, and S. R. Knollmann. The dynamical state of dark matter haloes in cosmological simulations - I. Correlations with mass assembly history. *MNRAS*, 419:1576--1587, January 2012. doi: 10.1111/j.1365-2966.2011.19820.x.
- A. Praagman, J. Hurley, and C. Power. Star cluster evolution in dark matter dominated galaxies. *New A*, 15:46--51, January 2010. doi: 10.1016/j.newast.2009.05.003.
- T. J. Pratt, L. G. Martinez, M. O. Vahle, and T. V. Archuleta. Sandia's network for supercomputer '96: Linking supercomputers in a wide area asynchronous transfer mode (atm) network. Technical report, Sandia National Labs., Albuquerque, NM (United States), 1997.
- W. H. Press and P. Schechter. Formation of Galaxies and Clusters of Galaxies by Self-Similar Gravitational Condensation. *ApJ*, 187:425--438, February 1974. doi: 10.1086/152650.
- S. Prunet, C. Pichon, D. Aubert, D. Pogosyan, R. Teyssier, and S. Gottloeber. Initial Conditions For Large Cosmological Simulations. *ApJS*, 178:179--188, October 2008. doi: 10.1086/590370.

- S. A. Pustilnik and A. L. Tepliakova. Study of galaxies in the Lynx-Cancer void - I. Sample description. *MNRAS*, 415:1188--1201, August 2011.
- D. Reed, J. Gardner, T. Quinn, J. Stadel, M. Fardal, G. Lake, and F. Governato. Evolution of the mass function of dark matter haloes. *MNRAS*, 346:565--572, December 2003. doi: 10.1046/j.1365-2966.2003.07113.x.
- D. Reed, F. Governato, L. Verde, J. Gardner, T. Quinn, J. Stadel, D. Merritt, and G. Lake. Evolution of the density profiles of dark matter haloes. *MNRAS*, 357:82--96, February 2005. doi: 10.1111/j.1365-2966.2005.08612.x.
- D. S. Reed, R. Bower, C. S. Frenk, A. Jenkins, and T. Theuns. The halo mass function from the dark ages through the present day. *MNRAS*, 374:2--15, January 2007. doi: 10.1111/j.1365-2966.2006.11204.x.
- D. S. Reed, S. M. Koushiappas, and L. Gao. Non-universality of halo profiles and implications for dark matter experiments. *MNRAS*, 415:3177--3188, August 2011. doi: 10.1111/j.1365-2966.2011.18930.x.
- E. Regos and M. J. Geller. The evolution of void-filled cosmological structures. *ApJ*, 377: 14--28, August 1991.
- F. Renaud and M. Gieles. The role of galaxy mergers on the evolution of star clusters. *MNRAS*, 431:L83--L87, April 2013. doi: 10.1093/mnras/slt013.
- F. Renaud, M. Gieles, and C. M. Boily. Evolution of star clusters in arbitrary tidal fields. *MNRAS*, 418:759--769, December 2011. doi: 10.1111/j.1365-2966.2011.19531.x.
- R. R. Rojas, M. S. Vogeley, F. Hoyle, and J. Brinkmann. Photometric Properties of Void Galaxies in the Sloan Digital Sky Survey. *ApJ*, 617:50--63, December 2004.
- R. R. Rojas, M. S. Vogeley, F. Hoyle, and J. Brinkmann. Spectroscopic Properties of Void Galaxies in the Sloan Digital Sky Survey. *ApJ*, 624:571--585, May 2005.
- Brent Rood, Nathan Gnanasambandam, Michael J. Lewis, and Naveen Sharma. Toward high performance computing in unconventional computing environments. In *Proceedings of the 19th ACM International Symposium on High Performance Distributed Computing*, HPDC '10, pages 627--635, New York, NY, USA, 2010. ACM. ISBN 978-1-60558-942-8. doi: <http://doi.acm.org/10.1145/1851476.1851569>. URL <http://doi.acm.org/10.1145/1851476.1851569>.
- V. Sahni, B. S. Sathyaprakah, and S. F. Shandarin. The evolution of voids in the adhesion approximation. *ApJ*, 431:20--40, August 1994.
- T. R. Saitoh, H. Daisaka, E. Kokubo, J. Makino, T. Okamoto, K. Tomisaka, K. Wada, and N. Yoshida. Toward First-Principle Simulations of Galaxy Formation: II. Shock-Induced Starburst at a Collision Interface during the First Encounter of Interacting Galaxies. *PASJ*, 61:481--, June 2009.
- W. E. Schaap and R. van de Weygaert. Continuous fields and discrete samples: reconstruction through Delaunay tessellations. *A&A*, 363:L29--L32, November 2000.
- P. Schechter. An analytic expression for the luminosity function for galaxies. *Astrophysical Journal*, 203:297--306, January 1976.
- R. K. Sheth and G. Tormen. Large-scale bias and the peak background split. *MNRAS*, 308:119--126, September 1999. doi: 10.1046/j.1365-8711.1999.02692.x.
- R.K. Sheth and R. van de Weygaert. A hierarchy of voids: much ado about nothing.

- MNRAS*, 350(2):517--538, May 2004.
- V. Springel, S. D. M. White, A. Jenkins, C. S. Frenk, N. Yoshida, L. Gao, J. Navarro, R. Thacker, D. Croton, J. Helly, J. A. Peacock, S. Cole, P. Thomas, H. Couchman, A. Evrard, J. Colberg, and F. Pearce. Simulations of the formation, evolution and clustering of galaxies and quasars. *Nature*, 435:629--636, June 2005. doi: 10.1038/nature03597.
- V Springel, J Wang, M Vogelsberger, A Ludlow, A Jenkins, A Helmi, J F Navarro, C S Frenk, and S D M White. The Aquarius Project: the subhaloes of galactic haloes. *Monthly Notices of the Royal Astronomical Society*, 391(4):1685--1711, December 2008.
- J. Stadel, D. Potter, B. Moore, J. Diemand, P. Madau, M. Zemp, M. Kuhlen, and V. Quilis. Quantifying the heart of darkness with GALLO - a multibillion particle simulation of a galactic halo. *MNRAS*, 398:L21--L25, September 2009. doi: 10.1111/j.1745-3933.2009.00699.x.
- K. Stanonik, E. Platen, M. A. Aragón-Calvo, J. H. van Gorkom, R. van de Weygaert, J. M. van der Hulst, and P. J. E. Peebles. Polar Disk Galaxy Found in Wall Between Voids. *ApJL*, 696(1):L6--L9, May 2009.
- C. Stewart, R. Keller, R. Repasky, M. Hess, D. Hart, M. Muller, R. Sheppard, U. Wossner, M. Aumuller, H. Li, D. Berry, and J. Colbourne. A global grid for analysis of arthropod evolution. In *GRID '04: Proceedings of the 5th IEEE/ACM International Workshop on Grid Computing*, pages 328--337, Washington, DC, USA, 2004. IEEE Computer Society.
- L. E. Strigari, J. S. Bullock, M. Kaplinghat, J. D. Simon, M. Geha, B. Willman, and M. G. Walker. A common mass scale for satellite galaxies of the Milky Way. *Nature*, 454:1096--1097, August 2008. doi: 10.1038/nature07222.
- S. Sundari M., S. S. Vadhiyar, and R. S. Nanjundiah. Morco: middleware framework for long-running multi-component applications on batch grids. In *Proceedings of the 19th ACM International Symposium on High Performance Distributed Computing*, HPDC '10, pages 328--331, New York, NY, USA, 2010. ACM. ISBN 978-1-60558-942-8. doi: <http://doi.acm.org/10.1145/1851476.1851522>. URL <http://doi.acm.org/10.1145/1851476.1851522>.
- A. Szomoru, J. H. van Gorkom, M. D. Gregg, and M. A. Strauss. An HI Survey of the Bootes Void. II. The Analysis. *AJ*, 111:2150, June 1996.
- K. Takahashi and S. F. Portegies Zwart. The Evolution of Globular Clusters in the Galaxy. *ApJ*, 535:759--775, June 2000. doi: 10.1086/308857.
- A. Tanikawa and T. Fukushige. Mass-Loss Timescale of Star Clusters in an External Tidal Field. I. Clusters on Circular Orbits. *PASJ*, 57:155--164, February 2005.
- A. Tanikawa and T. Fukushige. Mass-Loss Timescale of Star Clusters in an External Tidal Field. II. Effect of Mass Profile of Parent Galaxy. *PASJ*, 62:1215--1230, October 2010.
- J. E. Taylor and J. F. Navarro. The Phase-Space Density Profiles of Cold Dark Matter Halos. *ApJ*, 563:483--488, December 2001. doi: 10.1086/324031.
- R. Teyssier, S. Pires, S. Prunet, D. Aubert, C. Pichon, A. Amara, K. Benabed, S. Colombi, A. Refregier, and J.-L. Starck. Full-sky weak-lensing simulation with 70 billion particles. *A&A*, 497:335--341, April 2009. doi: 10.1051/0004-6361/200810657.

- A. V. Tikhonov and I. D. Karachentsev. Minivoids in the Local Volume. *ApJ*, 653:969--976, December 2006.
- J. Tinker, A. V. Kravtsov, A. Klypin, K. Abazajian, M. Warren, G. Yepes, S. Gottlöber, and D. E. Holz. Toward a Halo Mass Function for Precision Cosmology: The Limits of Universality. *ApJ*, 688:709--728, December 2008. doi: 10.1086/591439.
- S Toonen, G Nelemans, and Simon F Portegies Zwart. Supernova Type Ia progenitors from merging double white dwarfs. Using a new population synthesis model. *Astronomy & Astrophysics*, 546:70, October 2012.
- R. van de Weygaert and J. R. Bond. Clusters and the Theory of the Cosmic Web. In M. Plionis, O. López-Cruz, and D. Hughes, editors, *A Pan-Chromatic View of Clusters of Galaxies and the Large-Scale Structure*, volume 740 of *Lecture Notes in Physics*, Berlin Springer Verlag, page 335, 2008.
- R. van de Weygaert and E. Platen. Cosmic Voids: Structure, Dynamics and Galaxies. *International Journal of Modern Physics Conference Series*, 1:41, 2011. doi: 10.1142/S2010194511000092.
- R. van de Weygaert and W. Schaap. The Cosmic Web: Geometric Analysis. In V. J. Martínez, E. Saar, E. Martínez-González, and M.-J. Pons-Bordería, editors, *Data Analysis in Cosmology*, volume 665 of *Lecture Notes in Physics*, Berlin Springer Verlag, pages 291--413, 2009. doi: 10.1007/978-3-540-44767-2\_11.
- R. van de Weygaert and E. van Kampen. Voids in Gravitational Instability Scenarios - Part One - Global Density and Velocity Fields in an Einstein - De-Sitter Universe. *MNRAS*, 263(2):481, July 1993.
- F. C. van den Bosch, G. Tormen, and C. Giocoli. The mass function and average mass-loss rate of dark matter subhaloes. *MNRAS*, 359:1029--1040, May 2005. doi: 10.1111/j.1365-2966.2005.08964.x.
- E. P. J. van den Heuvel and S. Portegies Zwart. Are Super-Luminous supernovae and Long GRBs produced exclusively in young dense star clusters? *arXiv:1303.6961*, March 2013.
- E. Vesperini and D. C. Heggie. On the effects of dynamical evolution on the initial mass function of globular clusters. *MNRAS*, 289:898--920, August 1997.
- A. M. von Benda-Beckmann and V. Müller. Void statistics and void galaxies in the 2dF Galaxy Redshift Survey. *MNRAS*, 384:1189--1199, March 2008.
- J. Wambsganss, P. Bode, and J. P. Ostriker. Giant Arc Statistics in Concord with a Concordance Lambda Cold Dark Matter Universe. *ApJ*, 606:L93--L96, May 2004. doi: 10.1086/421459.
- H. Wang, H. J. Mo, Y. P. Jing, X. Yang, and Y. Wang. Internal properties and environments of dark matter haloes. *MNRAS*, 413:1973--1990, May 2011. doi: 10.1111/j.1365-2966.2011.18301.x.
- M. S. Warren, K. Abazajian, D. E. Holz, and L. Teodoro. Precision Determination of the Mass Function of Dark Matter Halos. *ApJ*, 646:881--885, August 2006. doi: 10.1086/504962.
- R. H. Wechsler, J. S. Bullock, J. R. Primack, A. V. Kravtsov, and A. Dekel. Concentrations of Dark Halos from Their Assembly Histories. *ApJ*, 568:52--70, March 2002. doi:

- 10.1086/338765.
- G. Wegner and N. A. Groggin. Ages and Metallicities of Early-Type Void Galaxies from Line Strength Measurements. *AJ*, 136:1, July 2008.
- M. White, J. D. Cohn, and R. Smit. Cluster galaxy dynamics and the effects of large-scale environment. *MNRAS*, 408:1818--1834, November 2010. doi: 10.1111/j.1365-2966.2010.17248.x.
- S. D. M. White and M. J. Rees. Core condensation in heavy halos - A two-stage theory for galaxy formation and clustering. *MNRAS*, 183:341--358, May 1978.
- H. Yahagi, M. Nagashima, and Y. Yoshii. Mass Function of Low-Mass Dark Halos. *ApJ*, 605:709--713, April 2004. doi: 10.1086/382649.
- K. Yoshikawa and T. Fukushige. PPPM and TreePM Methods on GRAPE Systems for Cosmological N-Body Simulations. *PASJ*, 57:849--860, December 2005.
- I. B. Zeldovich, J. Einasto, and S. F. Shandarin. Giant voids in the universe. *Nature*, 300:407--413, December 1982.
- Y. B. Zel'dovich. Gravitational instability: An approximate theory for large density perturbations. *A&A*, 5:84--89, March 1970.
- A. R. Zentner, A. A. Berlind, J. S. Bullock, A. V. Kravtsov, and R. H. Wechsler. The Physics of Galaxy Clustering. I. A Model for Subhalo Populations. *ApJ*, 624:505--525, May 2005. doi: 10.1086/428898.
- D. H. Zhao, Y. P. Jing, H. J. Mo, and G. Börner. Mass and Redshift Dependence of Dark Halo Structure. *ApJ*, 597:L9--L12, November 2003. doi: 10.1086/379734.
- D. H. Zhao, Y. P. Jing, H. J. Mo, and G. Börner. Accurate Universal Models for the Mass Accretion Histories and Concentrations of Dark Matter Halos. *ApJ*, 707:354--369, December 2009. doi: 10.1088/0004-637X/707/1/354.

## Curriculum Vitae

Ik ben op 3 april 1983 geboren in Zwolle. Al vroeg raakte ik geïnteresseerd in sterrenkunde, en op mijn achtste verjaardag kreeg ik mijn eerste telescoop. Tevens werd ik dat jaar lid van de Jongerenwerkgroep voor Sterrenkunde (JWG). Met de JWG heb ik vele cursussen, praatjes en kampen meegemaakt, die mijn interesse in de sterrenkunde alleen maar vergrootten.

Van 1995 tot 2001 zat ik in Zwolle op het Gymnasium Coleanum. Daarna begon ik aan de opleiding "Natuur- en Sterrenkunde" aan de Universiteit Utrecht. Mijn bacheloronderzoek heb ik daar voltooid bij Henny Lamers, gevolgd door een masteronderzoek bij Søren Larsen. In 2008 behaalde ik in Utrecht mijn MSc-diploma.

In 2009 begon ik in Amsterdam aan mijn promotie in de computationele sterrenkunde bij Simon Portegies Zwart en Cees de Laat, om na slechts een paar maanden met Simon zijn groep mee te verhuizen naar de Sterrewacht Leiden. Na de afronding van mijn promotie ben ik in september 2013 als postdoc begonnen bij het Kapteyn instituut in Groningen.





## Nawoord

Nou moe?!? De tijd is voorbij gevlogen, nu zit ik hier al met een voltooid proefschrift. Daar heeft behoorlijk wat werk in gezeten, en niet alleen van mijzelf. Ik wil graag van deze pagina's gebruik maken om de vele anderen die hier op enige wijze aan hebben bijgedragen te bedanken.

Allereerst mijn familie. Zonder hen zou ik hier letterlijk, maar ook figuurlijk niet zijn. Ik heb nooit gebrek aan steun gehad. Dank jullie allemaal, betere familieleden kan ik me niet voorstellen.

Ook de (voormalige) leden van de "Computational Astrophysics" onderzoeksgroep ben ik allen veel dank schuldig. Een aantal wil ik in het bijzonder bedanken voor hun bijdragen. Derek, Jeroen, Arjen, Inti, Nathan en Niels: zonder jullie waren CosmoGrid, Bonsai en AMUSE er nooit gekomen, en had dit proefschrift dus heel anders uitgekapt! Michiko, Bernadetta and Carmen, you were the best officemates one could hope for in these last two years. Dan, Alex: thank you for all the fun times we had!

I was also fortunate enough to be a guest at Kapteyn institute in Groningen on occasion. Rien, all Kapteyners: thank you for making me feel part of the group there as well (in advance to really being a member of the group, as it turned out)!

As institutes go, I can't think of a better place to do one's PhD than the Sterrewacht Leiden. During these four years, it's become like a home. There are so many people there that have become my friends... I could probably fill a few pages just mentioning names of the people I owe thanks to, for all those conversations at tea time, borrels, and where not. All of you: thank you so very much for making the Sterrewacht such a wonderful place to be!

A few people (formerly) at the sterrewacht I would like to thank in particular. Allereerst Marcel: dank je voor alle gesprekken (op het werk, in de trein, in het café, bij de JWG, op vakantie, waar dan ook), over van alles en nog wat! Dankzij internet is de VS ook lang niet zo ver meer als het vroeger leek... Henriette: I am very grateful you agreed to be one of my paranymphs! Jeanette: Always a pleasure to talk with you, from political differences between our countries to PhD troubles and

what not! Matt: thanks for all the moral support and conversations. Mattia: thank you for organizing lots of parties, great memories of the Hutspot party and the Sinterklaasparties. Remco en alle andere klaverjasmaatjes: jammer dat jullie steeds de voorkeur gaven aan Rotterdams, maar dat blijft natuurlijk fijner dan überhaupt niet klaverjassen. Rob: I love working on our little project, can't wait to see what else may come out of it! Jeanne, Evelijn, Jan, Erik, David, Niels, Aart, Tycho, Liesbeth en Anita: zonder jullie zou het allemaal lang niet zo goed lopen bij de sterrewacht. Dank voor al jullie ondersteuning!

Mijn vrienden bij de JWG (ook al te veel om allemaal op te noemen) verdienen hier ook een bijzondere vermelding, aangezien ik zonder de JWG waarschijnlijk niet in de sterrenkunde terecht zou zijn gekomen. De afgelopen jaren was ik actief in het hoofdbestuur van de JWG en de redactie van *Universum*. Voor die fijne tijd wil ik graag al mijn mede-HB'ers en redacteurs bedanken, in het bijzonder Anna en Ruben, zonder wie *Universum* lang niet zo'n goed blad zou zijn geweest.

Naast sterrenkunde ben ik de afgelopen jaren ook actief geweest binnen D66. Het was ontzettend prettig om ook af en toe nog met totaal andere dingen bezig te zijn dan het heelal en simulaties, daarvoor ben ik al mijn vrienden binnen D66 erg dankbaar!

Ik wil ook graag nog twee goede school- en studievrienden bedanken. Jacob: je bent er altijd, en dat is ontzettend fijn! Tim: heel hartelijk bedankt dat ook jij toegezegd hebt mijn paranimf te willen zijn!

Tenslotte wil ik graag mijn promotoren bedanken. Cees: we hebben lang niet zo veel samengewerkt als de bedoeling was, maar die samenwerking vond ik wel heel prettig. Simon: zonder jou was het natuurlijk überhaupt allemaal niet zover gekomen. Ik geloof niet dat ik een betere promotor had kunnen wensen, ik heb ontzettend genoten van de afgelopen jaren!